MAX-PLANCK-INSTITUT FÜR KOLLOID- UND GRENZFLÄCHENFORSCHUNG

FUNCTIONALIZATION OF NANOPOROUS CARBON MATERIALS FOR CHIRAL SEPARATION AND HETEROGENEOUS OXIDATION CATALYSIS

Dissertation

zur Erlangung des akademischen Grades
Doktor der Naturwissenschaften („Doctor rerum naturalium", Dr. rer. nat.)
in der Wissenschaftsdisziplin „Kolloidchemie"

eingereicht an der Mathematisch-Naturwissenschaftlichen Fakultät
der Universität Potsdam

von

Milena Perovic

Ort und Tag der Disputation: Potsdam, 08.12.2020

Hauptbetreuer: Prof. Dr. Dr. h.c. Markus Antonietti

Betreuerinnen: Prof. Dr. Yan Lu
Dr. Martin Oschatz

Gutachterinnen: Prof. Dr. Dr. h.c. Markus Antonietti
Dr. Martin Oschatz
Prof. Dr. Joanna Gościańska

Published online on the
Publication Server of the University of Potsdam:
https://doi.org/10.25932/publishup-43571
https://nbn-resolving.org/urn:nbn:de:kobv:517-opus4-435713

Acknowledgment

I would like to thank my supervisor, Prof. Markus Antonietti, for the opportunity to conduct my research at the Department of Colloid Chemistry at the Max Planck Institute of Colloids and Interfaces.

My sincerest acknowledgment goes to my mentor who was supporting my work and me throughout the years, (soon Prof.) Dr. Martin Oschatz. Scientific discussions with him were always fruitful, enjoyable, and I always left his office more optimistic and smiling. He believed in me from the beginning and was willing to support my career and academic growth. I learned a lot from him, not only in the field of porous carbons, materials science, and catalysis, but maybe even more importantly: life and human relations. Thank you, Martin!

I would like to acknowledge Prof. Yan Lu from the University of Potsdam and Helmholtz-Zentrum Berlin für Materialien und Energie, for supervising the thesis.

I am very grateful for the numerous collaborators of this work. M.Sc. Sapir Shekef and Prof. Yitzhak Mastai from Bar-Ilan University in Israel were supportive in providing me the chiral materials and being great warm hosts during our project visit. I thank Dr. Lukas Zeininger for bringing me into the world of fluorocarbons and for a nice collaboration. Dr. Nadezda V. Tarakina and Bolortuya Badamdorj performed HRTEM measurements, and XPS was measured by Prof. Dr. Jan Philipp Hofmann at the Eindhoven University of Technology, The Netherlands. I would like to thank the following colleagues and technicians for their assistance with the collection of my data: Rona Pitschke and Heike Runge for TEM, SEM, and EDX measurements, Dr. Ralf Walczak and M.Sc. Wuyong Zhang for Raman spectroscopy, Antje Völkel for TGA and EA, Ines Below-Lutz for ICP-OES and general lab organization.

My PhD projects have been financially supported by the German-Israeli Foundation for Scientific Research and Development, and the Deutsche Forschungsgemeinschaft (DFG, German Research Foundation) under Germany's Excellence Strategy.

My colleagues at MPI became my friends over the past years, and I would like to thank them for a wonderful time at (and outside of) MPI, all of the coffees, BBQs, after-work beers, evenings and nights at CB, dinners and clubbing nights in Berlin. Thanks Barış, Paolo, João, İpek, Max, Marius, Konstantin, Runyu, Ivan, Julya, Tânia, Nina, Daniel, Vale, Majd, Jose, Francesco, Ale, Stefano, Diana, Marko, Qing, and many others.

I am thankful for my long-time friends that were always there for me and made my entire academic journey easier: Acka (+ Letići), Jovana, Mina, Gala, Mario. A special thanks goes to my Ex-Yugo-Berliners, Nataša, Ismar, Ivan Č, and Ivan U. My everyday PhD life was persistently enlivened by my dearest Kafultet (Iva, Makica, Sanja, Nadja) and my almost-Balkan group, Brian, Ilgın, Antreas, Rayoon, Anna-Maria, and Alexandra.

Finally, I am the most thankful to my family for their unconditional support, love, and strength they gave me: my parents Bosiljka and Milenko, brothers Miloš and Petar, and sister in law Svetlana. My deepest gratitude goes to my boyfriend Ralf for his support, patience, and help during my PhD journey.

The completion of the present thesis could not have been accomplished without the support of all of you, thank you, хвала, Danke!

Table of Contents

1. Motivation

Catalysis is essential in the modern world economy, which is constant growth due to increasing consumption. For example, every molecule in modern transportation fuels went through at least one catalytic process, and it is estimated that around 85% of all chemical processes are supported by catalysts. Among those, 80% of the processes are heterogeneously catalyzed, 17% make use of homogeneous catalysts, and 3% are biocatalytic processes.[1] The range of applications of heterogeneous catalysts covers harvesting, conversion, and storage of energy, production of bulk, specialty, and fine chemicals, as well as the production of food and pharmaceuticals. The global catalyst market size in 2019 amounted to 33 billion US$, with an estimation of the annual growth rate of about 4.5%.[2] However, the global sales of catalysts are not the only relevant measure for the importance of catalytic processes, since the entire catalysis industry, including the products obtained in this way, amount to more than 100 times the catalysts sales. Even more importantly, the environmental impact of catalysis is substantial, because the manufacturing processes require less energy and raw materials as the production becomes more efficient.[3-6]

In addition, especially in the pharmaceutical and agrochemical industry, a significant part of these processes involves chiral compounds. More than half of the drugs that are currently in use and 30% of active ingredients in agrochemicals are chiral, although the vast majority of these are manufactured as racemates (containing an equimolar mixture of two enantiomers).[7-9] However, in the pharmaceutical industry, the regulatory guidelines recommend the assessment of the activity of each enantiomer in every phase of the manufacturing process and clinical trials.[10-11] Due to the high costs, the production of agrochemicals has scarce regulations in this regard, which results in chiral pollution in the environment, particularly in soil.[12-13] Thus, obtaining enantiomerically pure compounds is necessary and it is usually accomplished by asymmetric synthesis and catalysis, as well as chiral separation. Following the general principles of the transition from homogeneous to heterogeneous catalysis, the efficiency of these processes may be vastly improved if the chiral selectors are positioned on a porous solid support, thereby increasing the available surface area for chiral recognition.[14]

Similarly, the majority of commercial catalysts are also supported, usually comprising of metal nanoparticles (NPs) dispersed on highly porous oxide or carbon material. These catalysts alone are already complex multi-component systems and become even more complicated under catalytic operation, which makes the understanding of their structure–activity relationship rather challenging. The interpretation and rationalization of these relationships and underlying principles are crucial for the improvement of catalytic processes, from both an industrial and academic point of view. One approach to get fundamental insights into the underlying mechanisms within such systems is a design of structurally well-defined model catalysts and investigation of their activity on model catalytic reactions.[15-16]

Materials that have exceptional thermal and chemical stability, and are electrically conductive are porous carbons. Their stability in extreme pH regions and temperatures, the possibility to tailor their pore architecture and chemical structure, and the possibility to support a process by the application of an external electric potential have already established these materials in the fields of separation and catalysis. However, there are severe challenges in applications of porous carbons, usually related to their less defined local atomic construction, absence of long-range order, and abundant defects (described in Chapter 2.1). This heterogeneous chemical structure in combination with typically present broad pore size distributions make it challenging to develop reliable models for the investigation of structure-performance relationships. Therefore, there is a necessity for expanding the fundamental understanding of these robust materials under experimental conditions to allow for their further optimization for particular applications. This thesis gives a contribution to our knowledge about carbons, through different aspects, and in different applications. On the one hand, a rather exotic novel application will be investigated by attempts in synthesizing porous carbon materials with an enantioselective surface. This application is long dominated by porous oxide materials with chiral surface functional groups, but their thermal and/or chemical instability hinders some of their uses and their recyclability. The studies presented in this thesis are one of the first attempts to utilize the advantages of porous carbon materials in chiral separation processes. On the other hand, the structure–activity relationship of carbons as supports for gold

nanoparticles in a rather traditional catalytic model reaction will be studied. The possibility of regulating catalytic activity by confinement effects on the fluid phase surrounding the catalyst will be presented. The local environment of a catalyst will be further controlled by introducing perfluorinated compounds, resulting in promoted catalytic activity. In both applications, important structure-property relationships can be concluded as carbon structures have a crucial influence on the respective performance, either directly on adsorption of chiral compounds or indirectly by changing the local environment of a catalyst.

2. Theoretical Background

2.1. Fundamentals of Porous Carbon Materials

Carbon is best known among chemists for its versatility. This originates from its position in the periodic table of elements, which enables this element to form bonds with both elements with low electronegativity, as well as high electronegativity. But even more importantly, its ability to catenate (bond with atoms of the same element into a chain) makes carbon a basis of organic life on Earth, which is easily illustrated with approximately 12 million carbon compounds known so far, most of which are in focus of organic chemistry. Inorganic carbon is most often found in the form of carbonates, which are minerals that build up sedimentary rocks. As one of the essential components of all organisms, carbon from ancient plants and animals composes fossil fuels (coal, oil, and natural gas).[17-19] It was once thought that the carbon-based molecules could only be obtained from living things, as they were thought to contain a 'spark of life'. This belief changed in 1828, when Friedrich Wöhler synthesized urea from inorganic reagents. This is also marked as the moment when the synthetic organic chemistry was born.[20-21]

The electronic structure of the carbon atom allows it to form bonds in different modes of hybridization – sp, sp^2, and sp^3. Even the explanation of hybridization theory can be easily followed on the examples of carbon-hydrogen compounds, by looking at acetylene ($HC{\equiv}CH$) for sp, ethylene ($H_2C{=}CH_2$) for sp^2, and ethane ($H_3C{-}CH_3$) for sp^3. This adaptability makes it easy for carbon to build numerous (nano)structures, which have different chemical construction and different properties but consist entirely of carbon atoms. Some of the most important allotropes of carbon are graphite, diamond, fullerenes, carbon nanotubes, and porous carbon (**Figure 2.1**). Diamond is an sp^3-hybridized form of carbon with a diamond cubic crystal structure (**Figure 2.1b**), known for its exceptional mechanical properties, such as hardness and toughness. In addition, due to its wide band gap (5.5 eV), this insulating material is transmitting visible light, which causes its clear colorless appearance. Diamond is a metastable form of carbon, suspended from converting to the most stable form – graphite by a high energy barrier. Graphite is a material in which

stacked layers, called graphene, are bonded through weak van der Waals interactions (**Figure 2.1a**). Carbon atoms in graphene are sp^2-hybridized and arranged in a hexagonal, honeycomb-like structure. As a result of electron delocalization within π-orbitals, both graphite and graphene are electronically conductive, soft, black materials.

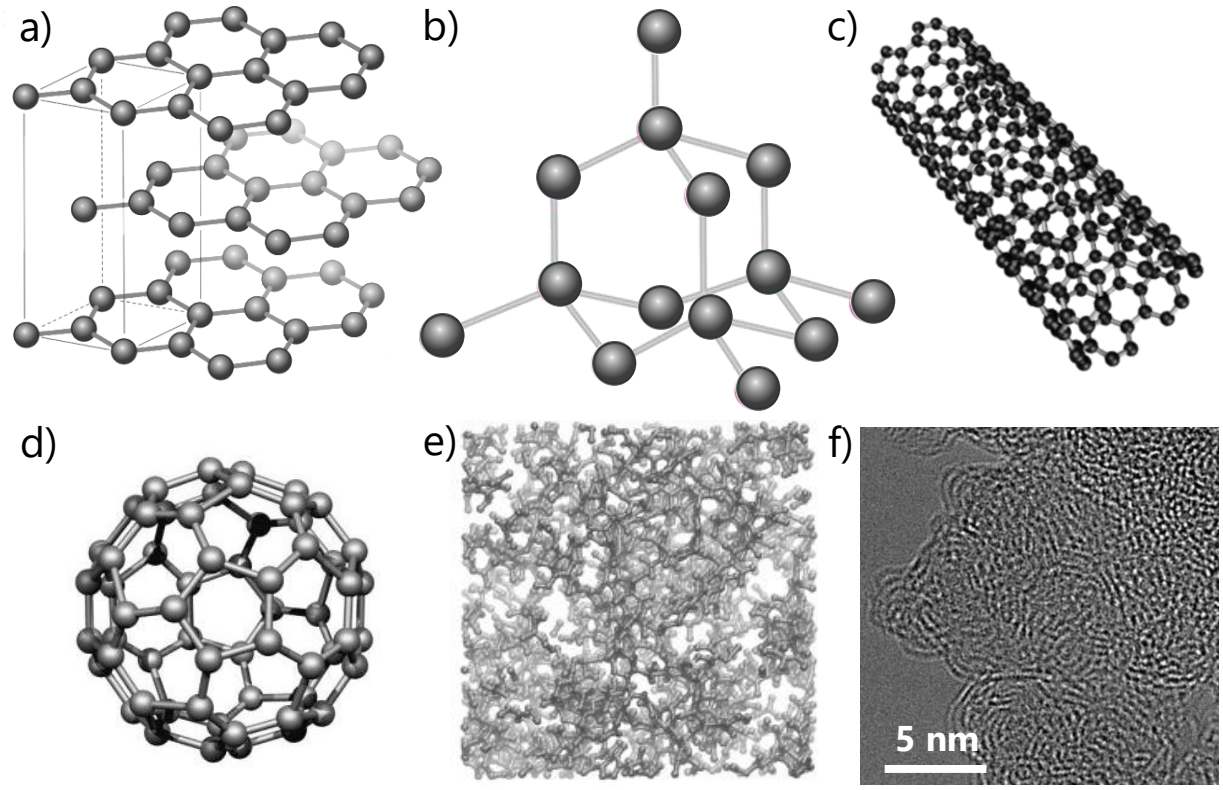

Figure 2.1. *Atomic structures of a) graphite, b) diamond, c) single-walled carbon nanotube, and d) fullerene, e) model atomic structure of a porous carbon material and f) high-resolution transmission electron microscopy image of a porous carbon.*

Artificial synthesis of urea from inorganic starting materials served as a bond between organic and inorganic chemistry. By a similar analogy, we could appoint nanostructured carbon materials as a bond between materials science and chemistry.

According to their dimensionality, nanostructured sp^2-hybridized carbon allotropes can be subdivided to 0-dimensional (0D) fullerenes (**Figure 2.1d**), 1-dimensional (1D) carbon nanotubes (CNTs) (**Figure 2.1c**), 2-dimensional (2D) graphene.[22] Graphene is a central building block of these structures, and by rolling a sheet of graphene single-walled carbon nanotubes are obtained, whereas curving graphene into a cage and replacing a certain amount of six-rings with five-rings, the result is a fullerene. Among the family of fullerenes,

the most famous member is C_{60}, also known as the buckminsterfullerene, although structures as small as C_{20}, as well as the ones containing several thousand carbon atoms are known so far.[23] Two main types of CNTs are single-, and multi-wall CTNs, referring to one layer, and multiple parallel layers of rolled graphene, respectively.[24] Other notable nanostructures of carbon materials are nanodiamonds (consist of only sp^3-hybridized carbon atoms),[25] onion-like carbons (multi-shell fullerenes),[26] carbon fibers, and porous carbon materials.

Similarly to sp^2-only carbon allotropes, porous carbons also originate from graphene, but what distinguishes them is their ill-defined local atomic arrangement. By substituting carbon six-rings in graphene or graphite by other structure motifs like five-rings, seven-rings, or defects, the structure of the carbon gets distorted (**Figure 2.1e** and **f**).[27] Such highly disordered graphene has an intrinsically high amount of pores. As defined by IUPAC (International Union of Pure and Applied Chemistry), a pore is a surface curvature whose cavity is deeper than wide. Porous carbon can have pores of different sizes, architectures, and connectivity, including micropores (< 2 nm in diameter), mesopores (2–50 nm), and macropores (> 50 nm).[28] Because of this property, porous carbons also stand out in the group of carbon allotropes. Namely, they possess a high ratio between internal and external surface area, and thus large intra-particle porosity. On the contrary, fullerenes, CNTs, and carbon onions experience a large external surface area that comes from inter-particle pores.

2.2. Different Synthesis Approaches towards Porous Carbon Materials

Intrinsic porosity of porous carbons, along with their electric and thermal conductivity, high chemical, thermal and mechanical stability has led to various commercial applications of these materials in the field of adsorption from the gas phase,[29-30] and from liquid, as electrode materials in batteries and supercapacitors,[31-32] and catalysis.[33-35] In all cases, porous carbons result from the carbonization of organic materials, which is a heat treatment in an inert atmosphere to a certain temperature resulting in decomposition of the organic materials and by that increased carbon content and decreased heteroatoms

content due to the release of volatile compounds such as water. This kind of synthesis method needs to fulfil certain criteria, such the control over the pore size and their distribution, high yield, sustainability, and others. The introduction of porosity in the porous carbons on an industrial scale is most widely accomplished by activation.

2.2.1. Activated Carbons

For the production of activated carbons, there is a broad range of possible carbon-containing organic materials used as precursors, for instance wood, nutshells, sawdust, pitch, fruit stones, coke, lignite, etc. Some of these parent-materials provide carbons that already have a certain amount of pores, however, their porosity is not sufficiently developed for most applications, and thus further modification of the pores is required. This is accomplished by widening existing porosity and creating further porosity, processes known as activation, which can be physical (thermal) or chemical. Activation can easily be imagined as etching of carbon atoms from the carbon network, creating additional pore volume and surface area due to pores enclosed by carbon atoms. Physical activation uses gasifying oxidation agents such as carbon dioxide and water vapor, either individually or together, to extract carbon atoms out of the material, according to the following equations:

$$2C + CO_2 \rightarrow C + 2CO \tag{2.1}$$

$$2C + H_2O \rightarrow C + H_2 + CO \tag{2.2}$$

Both reactions are endothermic and therefore controllable by temperature, which is not the case when oxygen is used, making it a less desirable gasifying agent. Although the stoichiometric equations above (Equation 2.1 and 2.2) seem simple, the mechanisms behind physical activation are much more complex. In both cases (CO_2 and H_2O) the development of porosity includes mechanisms of the opening of previously inaccessible pores, the creation of new pores, and the widening of existing pores. One would expect that the steam develops narrower pores than carbon dioxide, due to higher diffusivity and smaller kinetic diameter of the H_2O molecule. On the contrary, CO_2 activation develops narrow microporosity and a narrow pore size distribution, whereas steam produces wider

micropores with a broader micropore size distribution and slightly higher development of mesopores. This can be explained with the kinetics of these reactions, which involve multistage reaction sequences with adsorbed species that impact the rate of gasification. In the CO_2 activation process, the etching is inhibited by carbon monoxide through the removal of chemisorbed oxygen from the carbon surface, while in steam activation hydrogen inhibits the reaction both by removal of surface oxygen and by dissociative chemisorption of H_2 on the carbon surface. This makes hydrogen a much stronger inhibitor for the reaction of carbon with steam than is CO for the reaction of CO_2 with carbon, hence leading to a larger non-uniformity in steam activation.[36-37]

While physical activation is simple and broadly applicable, its energy consumption and low yield are clear drawbacks that can partly be overcome by applying chemical activation. This method is based on co-carbonization of precursor and an inorganic dehydration agent, most commonly zinc chloride ($ZnCl_2$), phosphoric acid (H_3PO_4), or potassium hydroxide (KOH). In a typical process, the carbon precursor is impregnated with a highly concentrated, aqueous solution of the activation agent. After the carbonization and removal of the activation agent by washing, the activated carbon material is obtained. The mechanisms by which the etching with diverse agents is accomplished are different, although in all cases the porosity can be slightly adjusted by altering the ratio of the precursor to the activation agent and by the activation temperature. Processes involving zinc chloride and phosphoric acid mostly rely on the extraction of water from the precursors, and chemical reaction with the precursor, respectively. On the other hand, the mechanism by which the activation with potassium hydroxide happens is more complex, involving the disintegration of structure, intercalation of metallic potassium, and gasification by the oxygen coming from the hydroxide. In conclusion, chemical activation has the advantages over physical activation in higher carbonization yields, easier control of surface functionalities, there is no selective removal of carbon atoms, and the porosity is often more precisely defined. At the same time, the activated carbons obtained from chemical activation procedures can contain inorganic impurities that originate from the activation agent, and additional synthesis steps are required.[38-41]

Nevertheless, none of these activation procedures can result in very narrowly distributed pores – especially when the resulting carbon materials have high specific surface area. Often the entire surface area of activated carbon is also not accessible for the guest species, because of their worm-like or bottleneck pore structure. These problems were partially addressed by the development of carbon gels.[42-44] They are obtained by the carbonization of organic gels synthesized by the sol-gel polycondensation of organic monomers such as resorcinol and formaldehyde. The cross-linked organic gels are subsequently dried, resulting in aerogels, cryogels, or xerogels, formed by supercritical, freeze, or vacuum drying, respectively. The structure of carbon gels typically consists of primary spherical particles connected with pores. Although they can be rich in intra-particle pores (inside of the spherical particles), their overall porosity is dominated by inter-particle voids.

2.2.2. Templating

The efforts to enhance the transport properties of carbon materials resulted in the development of a large variety of templating methods. In this way, well-defined bimodal, multimodal or hierarchical pore systems can be synthesized.[45-50]

In the old manufacturing process of casting that exists already for 6000 years, liquid material is poured into a copper mold, to obtain various tools, religious objects, and weapons. By scaling down this process from a macroworld to a nanoscale, “nanocasting” is achieved. First nanomaterials obtained in this way were porous carbons that appeared already at the beginning of the 1980s for the application as a stationary phase in chromatography.[51] However, the term “nanocasting” first appears in 1998, referring to a synthesis of a porous polymer network templated by silica.[52] Since then, there have been numerous studies applying this technique for the synthesis of porous carbon materials, which opened up new ones and enhanced the existing applications of carbons. Templates can be classified into exo-, and endotemplates, depending on whether the precursor occupies the internal, or external porosity of the template, respectively.[53] Endotemplated structures always result in a continuous phase of the porous material, whereas exotemplating can also lead to separated structures with a large contribution of inter-particle pores, like in particles or rods. According to the nature of the template, templating

processes can be categorized into hard, soft, and sacrificial templating. Moreover, in recent years there has been a rise in the usage of inorganic salts for building porosity in carbons. Although chemical activation with $ZnCl_2$ is known for a long time, there are several reasons why "salt templating" can be labeled as a separate templating method, and as such will be discussed in further text. Sacrificial templating represents an alternative synthetic approach towards porous carbons with sacrificial templates like metal-organic frameworks (MOF) or carbide-derived carbons (CDC). MOFs can be used both as sacrificial templates and without additional carbon sources – serving as a template and a carbon precursor simultaneously. The presence of metal ions or clusters in these frameworks allows incorporating metals or metal oxides into the resulting carbon material, or using the metals as a hard template that is removed by etching.[54-58] The latter principle is the basis for the synthesis of CDCs. Metal atoms from metal carbides are removed by high-temperature halogen treatments, typically resulting in the insertion of micropores and small mesopores, and good control over porosity parameters.[59-60] The disadvantages in carbon synthesis from MOFs are the low degree of control over the carbonization pathways, and synthesis of CDCs require multiple steps, is still rather expensive and results in low yields.

Hard templating

The hard-templating methods make use of various inorganic solid templates (e.g., silica, zeolites, alumina membranes, colloid crystals, etc.), that hold the nanostructure of the precursor during carbonization.[53, 61-62]

Extensive efforts towards the synthesis of uniform microporous carbons by using zeolites have been made in the past.[63-65] However, the resulting carbons are usually not as ordered as their parent zeolites, due to the very narrow pores of zeolites and a geometrical mismatch between the pores of zeolite and carbon material structure. In addition, they are intrinsically limited in the view of the porosity, which results in transport limitations in various applications. Materials with less restricted materials transport have been achieved with silica materials as hard templates. This is mainly due to the fact that the pores of silica can be adjusted over a broader range of sizes and geometries. In this way, their replica-

materials can be more precisely designed, which is the main advantage of this synthesis procedure over the typical activation, or sol-gel pathways. Some of the structured silica which are most often used as templates are members of the series MCM (Mobil Composition of Matter, developed by Mobil's researchers),[66] SBA (Santa Barbara Amorphous type material, according to the institution where they were originally synthesized, the University of California, Santa Barbara),[67-68] KIT (Korea Advanced Institute of Science and Technology, KAIST),[69] and others.[70-71] Interestingly, these templates are also obtained by templating procedure, but with soft templating instead. There are various available silica materials used as templates for carbon materials nowadays, with diverse geometries. Materials like SBA-15, MCM-41, SBA-3, and others, have a hexagonal ordered mesoporous structure (space group *p*6*mm*). Most prominent examples of 3-D cubic bicontinuous mesoporous silica (space group $Ia\bar{3}d$) are MCM-48 and KIT-6. 3-D cage-like cubic mesoporous structure is found in SBA-1 and SBA-6 with $Pm\bar{3}n$ symmetry, and in SBA-16 silica with $Im\bar{3}m$ symmetry.

Generally, the synthetic procedure for ordered mesoporous carbons templated by silica consists of the same elementary steps. Firstly, the silica template is impregnated with a carbon precursor, followed by subsequent polymerization of the precursor inside of the pores of silica. After carbonization, a composite of carbon and silica is obtained, which is transformed into a replica-carbon by removal of the silica template (**Figure 2.2**).[72] Because of the importance of this material in the present thesis, CMK-3 (carbon mesostructured by KAIST) will serve as an example of a typical nanocasting procedure in the following. Furthermore, this material is one of the first examples of ordered mesoporous carbon which retained the structural symmetry of the silica template.[72-73]

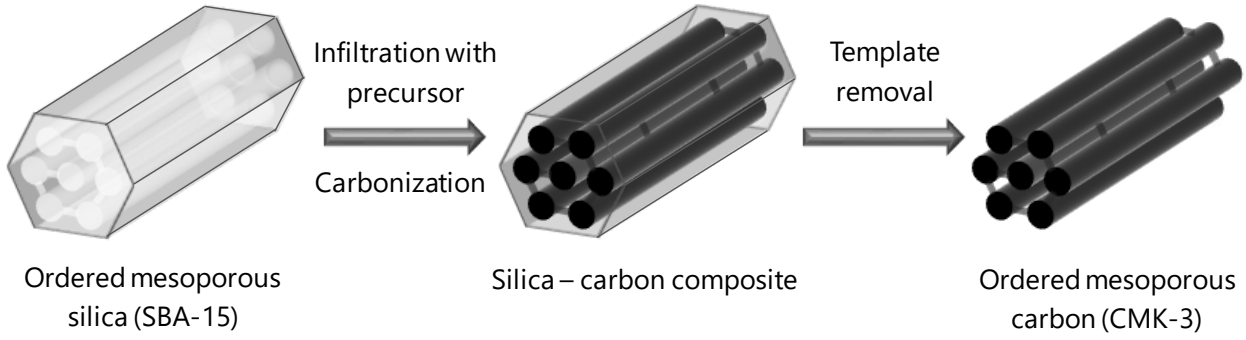

Figure 2.2. *The principle of hard templating on the example of CMK-3 synthesis.*

Hexagonally ordered mesoporous rods of SBA-15 are infiltrated with an aqueous solution of sucrose and sulfuric acid, which serve as a carbon precursor and a catalyst in a condensation reaction, respectively. An important criterion in the choice of carbon precursor is that it is capable of polymerizing and by that building a carbonaceous network, in other words, that it does not completely decompose to gases during carbonization. Moreover, it is desirable that the given precursor gives a high carbonization yield, and has low volume shrinkage during carbonization. After the polymerization of sucrose, the impregnation step is repeated to ensure the complete filling of the pores. Then, the composite is again heated and subsequently carbonized in an inert atmosphere. The removal of the silica template is accomplished by dissolution in NaOH, which results in a complete replica of SBA-15, ordered mesoporous carbon CMK-3. Mesopores of SBA-15 are interconnected with microporous channels, which enables complete infiltration of the void space of silica with carbon precursor. This is also the reason for the structural stability of carbon replica, that is, the ordered mesoporosity instead of a disordered network of carbon rods. The main disadvantages of hard templating are the need for a solid template material, the duration of the process with multiple steps, as well as harsh conditions for the template removal (either in a hot solution of NaOH or by leaching with HF).

Soft templating

In the soft templating process, organic molecules serve as a mold around which the inorganic framework is built. Typically, various kinds of surfactants are used as soft templates, and the processes involved are either sol-gel or solvent evaporation induced self-assembly (EISA) processes. Since the hydrolysis and condensation rates of silicates are

easily controlled by reaction conditions such as pH value and temperature, this route is especially suitable for the synthesis of mesoporous silica. The synthesis of ordered hexagonal mesoporous silica, SBA-15, is a prominent example of the self-assembly process occurring in soft templating.[67, 74] A structure-directing agent (SDA) employed here is a nonionic type of a surfactant, amphiphilic triblock copolymer Pluronic® P123 ($EO_{20}PO_{70}EO_{20}$) [1] in aqueous acidic conditions (pH ≈ 1), that forms micelles with poly(propylene oxide) inner core and the cylinder corona made up of poly(ethylene oxide) (**Figure 2.3**). A silicate precursor, tetraethyl orthosilicate (TEOS), undergoes hydrolysis catalyzed by acid and transforms into a sol of silicate oligomers. Cooperative assembly between silicate oligomers and surfactant micelles results in aggregation and precipitation of a gel. Afterward, hydrothermal treatment is carried out for the complete condensation and solidification, which results in improved long-range regularity and interconnecting pores between the individual mesopores that are important for nanocasting as in the case of CMK-3 discussed above. The final product is obtained after the calcination in order to remove the organic template.[75-77]

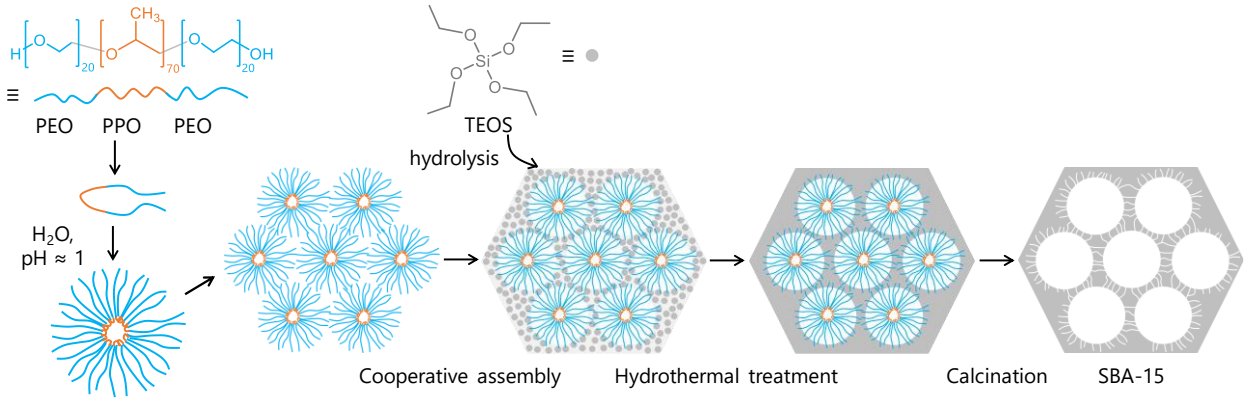

Figure 2.3. *The principle of soft templating on the example of SBA-15 synthesis.*

Synthesis of carbon materials *via* soft templating is, on the other hand, rather difficult due to several factors. The main challenge lies in the nature of the carbon precursor, which has to sustain the template removal step in the highly cross-linked polymeric state. On the other hand, an SDA has to be stable throughout the curing of the carbon, but at the same time that it readily decomposes after the synthesis. Finally, sufficient interactions (mostly

[1] PEO–PPO–PEO stands for poly(ethylene oxide)-*b*-poly(propylene oxide)-*b*-poly(ethylene oxide).

weak interactions such as Coulomb and van-der-Waals forces) between a carbon precursor and a template have to exist in order for a self-assembly process to take place. Nevertheless, there are several strategies towards soft-templated carbons, among which the most promising synthetic procedure uses organic-organic self-assembly which combines block copolymer templates and a polymerizable precursor.[78-81] Common copolymers are the family of Pluronic®, polystyrene-*b*-poly(ethylene oxide) (PS-*b*-PEO), and others, and typical carbon precursors include phenol–formaldehyde (resol), resorcinol–formaldehyde (RF resin), or phloroglucinol–formaldehyde (PF resin). A drawback of this templating procedure is that a thermal treatment induces shrinkage of the pore system, as a result of compaction of the material. As one result, the specific surface areas (SSA) of these materials usually do not exceed 1500 $m^2\ g^{-1}$.[82-83]

Salt templating

Already at the beginning of the 1990s, different synthetic parameters of chemical activation with $ZnCl_2$ were investigated, and it was seen that this inorganic salt prevents the contraction of carbon network, where the pore volume of final material could be linked to the volume of $ZnCl_2$ used. Remarkable SSA of more than 2000 $m^2\ g^{-1}$ was accomplished at a carbonization temperature of only 500 °C. Moreover, the usage of $ZnCl_2$ can positively influence the carbonization yield and catalyze the carbonization process. This and similar studies questioned the role of this salt being solely a chemical activation agent, and brought to the classification of this method of introducing porosity into carbons as "salt templating".[36, 38] The salt templating method uses non-carbonizable inorganic salt that is mixed with a carbon precursor, which builds a carbonaceous network in the presence of the molten salt at elevated temperatures (**Figure 2.4**). For these purposes, inorganic salts alone, or multi-component salt systems can be used (commonly used salts: $ZnCl_2$, LiCl, KCl, NaCl, LI, KI, etc.). The second broadens the operating temperature range due to the eutectic behavior of these salt (e.g., melting point of a eutectic composition of LiCl/KCl is 352 °C, in comparison to 610 °C for LiCl and 771 °C for KCl). By varying the salt melt system, as well as the proportion of template to the precursor, different modes of porosities and morphologies of resulting materials can be accomplished. For example, low content of salt in the mixture with the precursor can yield to purely microporous carbons (**Figure 2.4a**),

whereas higher salt content brings the development of larger micropores as well as mesopores (**Figure 2.4b**).[84-87] In addition, even the microstructure of carbons can be influenced by salt, by increasing the fraction of sheet-like structures belonging to thin graphite stacks. The formation of graphitic carbon nanostructures is a complex process involving the formation of metallic oxides and their reduction to elemental metal that finally catalyzes the conversion of amorphous carbon intro a graphitic one.[88-90] Removal of the salt is accomplished by washing with water or solution of acid, and this is at the same time the largest drawback of this templating method. Namely, the complete removal of inorganic species from carbon can be problematic, especially if the carbonaceous network also has heteroatoms in the backbone, since they can effectively stabilize electrophilic metal cations. This is often the case as the latter can vice versa stabilize Lewis-basic heteroatoms under high temperature carbonization conditions.

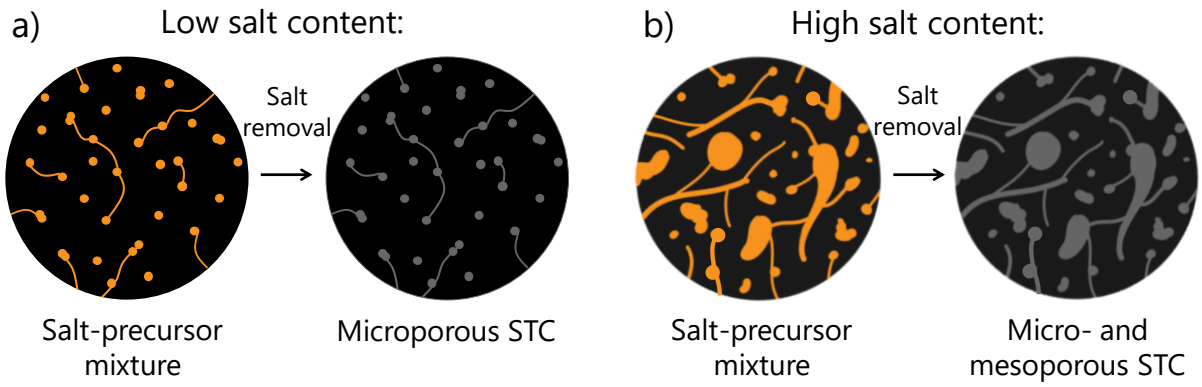

Figure 2.4. *The principle of salt templating using different salt mixtures and/or different ratios of carbon precursor to salt template.*

In chapter 2.2, an overview over different synthesis approaches towards porous carbons was given. All these different methods and pathways in principle have the same goal, and that is tailoring the porosity of the material for specific applications. These applications, although very diverse, share one basic principle, that is, the interaction of species from a fluid phase with a solid surface (that is, adsorption process). Properties of porous materials that can influence the interactions with guest species are pore architecture and the electron density (distribution) within the pore walls. Therefore, ways of affecting the latter are essential to efficiently utilize carbon materials and can be accomplished by chemical functionalization.

2.3. Functionalization of Porous Carbon Materials

Chemical functionalization is a powerful tool for altering the adsorption properties of porous materials as it can add specific chemical interactions such as formation of donor-acceptor couples or hydrogen bonds in addition to pure physisorption that is dominated by non-specific van-der-Waals interactions. In order to make the maximum possible use of chemical functionalization to tailor adsorption processes on carbon surfaces, it is important that the functional motifs are uniform throughout the material, and that the other properties are retained (i.e., crystallinity, pore architecture, etc.).In materials with high degrees of structural ordering, like MOFs or zeolites, or materials with known and regular surface functionalities, like silica or porous polymers, post-synthetic modifications are straightforward. In the case of porous carbon materials, on the other hand, the local arrangement of atoms in the network is abundant in defects, making these materials electronically heterogeneous. For that reason, the functionalization of carbons has to be accomplished through alternative strategies. In recent years, the scientific community has been focusing on several ways, including heteroatom doping, incorporation of metallic species, and formation of composites, which will be described in the following. [57, 91-96]

2.3.1. Heteroatom Functionalization

Heteroatom doping of carbons is defined as chemical attachment or incorporation of heteroatoms (e.g., nitrogen, boron, phosphorus, oxygen, sulfur, etc.) into the carbon network of the material (**Figure 2.5**). These functionalities can be introduced by post-synthetic treatments, which include heat treatment in the desired atmosphere (for example, NH_3 atmosphere for N-doping or diborane atmosphere for B-doping), or subjecting the carbon to certain chemical agents (for example boiling in nitric acid for O-doping).[97-98] However, due to the different reactivity of atoms in the porous carbon backbone, this approach offers lower control over the resulting material and usually generates only surface functionalities instead of incorporating heteroatoms into the network of porous carbon.

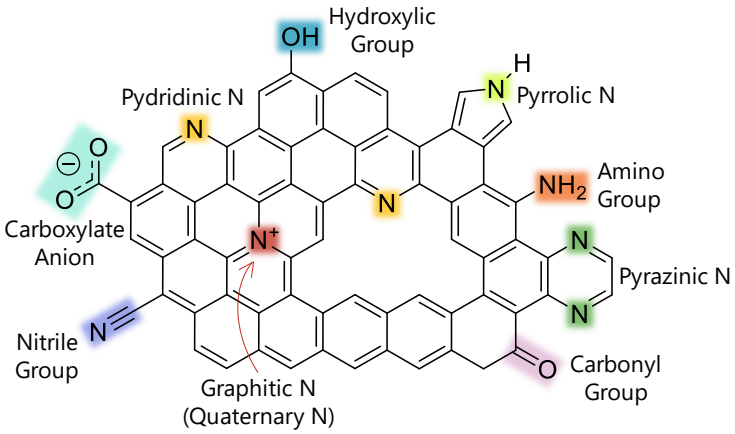

Figure 2.5. *Some of the possible heteroatom-containing functional groups within porous carbon materials.*

Thus, synthetic strategies offering a higher degree of control over heteroatom doping are needed. This can be achieved by adding a source of heteroatoms to the carbon precursor prior to carbonization,[99-100] or direct carbonization of a heteroatom-containing material. Viable approaches using heteroatom-containing precursors that have been investigated in recent years include carbonization of MOFs,[56, 101] porous polymers,[102-103] or (poly)ionic liquids,[104-105] and condensation and coordination reactions of molecular building blocks.[106-108]

Ionic Liquids as Carbon Precursors

Ionic liquids (ILs) are mostly organic salts that are liquid at temperatures below 100 °C and have a negligible vapor pressure.[109] The latter is an especially beneficial property for materials used as carbon precursors since they can be heated without evaporating, and easily processed and shaped without the need for a solvent. Another attractive feature of ILs is the ability to have control over multiple properties by tuning cation and anion pairs. It is, however, necessary that they meet certain requirements before the ILs can be utilized as carbon and heteroatom precursors.[110-111] To avoid complete thermal decomposition, ILs have to possess polymerizable groups in their structure, or (pre)polymerized ILs can be used.[112-114] The common approach is using cross-linkable functional groups with high heteroatom content (e.g., cyano groups that undergo trimerization reaction),[115-117] which follows the same mechanism as the formation of covalent triazine frameworks.[118-119]

Nonetheless, thermal decomposition can also be prevented by using spatial confinement, that is, by nanocasting with inorganic oxides such as silica, alumina, or titania.[115, 120-121] IL interacts strongly with the polar surface of oxides, leading to homogeneous coverage of the pores of the template, and by that in both higher yield of carbonaceous material, and a porous replica of a template.[122] In this process, nanoconfinement is an important factor affecting the course of carbonization, mostly by lowering the rate of dehydration of IL.[123] Other ways of introducing porosity into IL-derived carbons are salt templating, or by using sacrificial ions, specifically non-crosslinkable counterions that serve as templates.[113, 124-125] Finally, it is important to note that the usage of such costly carbon precursors cannot always be justified by the superior properties of the resulting carbons. This can be addressed by a formation of IL-derived carbon coating on an ordinary inexpensive carbon bulk material, gaining simultaneously heteroatom doping and control over porosity.[126-127]

2.3.2. Functionalization by Composite Engineering

What is often a limiting aspect of the utilization of novel materials is that certain traits have to be sacrificed for the benefit of the other desired properties. For instance, by increasing heteroatom content, and thus the polarity of porous carbon, the adsorption enthalpy of a given adsorbent will increase but other crucial properties such as conductivity or porosity can be lost. As it was mentioned in the example of IL-based carbon materials, the compromise can successfully be found in the formation of composite materials. Practically, it means functionalizing a porous carbon with a heteroatom-containing carbon material, resulting in a material that bears two different sets of characteristics in one material. Interestingly, the interface formed between two materials becomes an area where synergistic effects can occur, as a consequence of charge transfer.[128] Formation of junctions within composite materials consisting of nanostructured sp^2-hybridized carbon allotropes (graphene, CNT, fullerene, etc.) has been widely studied and applied.[129-131] The outcome of such composite engineering is controlled doping of materials without covalent functionalization and thus change in their work function and other surface-related parameters.[132] When the contact between the materials is made, electrons flow from material with more electrons (more shallow Fermi level compared to vacuum) to the material with fewer electrons (lower-lying Fermi level compared to vacuum), to equalize

the Fermi levels in materials.[133] For example, when a junction between graphene and a metallic single-walled carbon nanotube is made, graphene is being doped with electrons. This is due to the higher work function of graphene (lower Fermi level) than that of metallic CNT, resulting in electron transfer from CNT to graphene. This means that the graphene is being n-doped, while CNT is being p-doped.[134] Even the growth of CNTs, and therefore their chirality, is governed by charge transfer between the metal cluster (used as a catalyst for CNT growth) and a carbon cap.[135]

However, these synergistic effects are not only applicable to carbon nanomaterials with high degrees of order, as they were already recognized in composites of porous carbon materials as well.[126-127, 136] π–π interactions between two different carbon structures are responsible for colloidal stabilization of CNTs and enable their potential utilization as inks, films, or conductive membranes. Nitrogen-doped carbon hollow nanospheres ("nanobubbles") are rather electron-poor (lower Fermi level) and they exhibit superior dispersability in water due to their negatively charged surface. Upon their contact with CNTs in an aqueous phase, a cooperative stabilization occurs, leading to the creation of coacervates. Stabilization is a result of donor/acceptor-like interaction, where charge density is transferred from the electron-rich CNTs to the nanobubbles (**Figure 2.6**).[137] Another example where superior performance was accomplished by the formation of a composite material used nitrogen-doped carbon on carbon fibers. Nitrogen-doped carbons obtained by post-synthetic treatment, or by low-temperature condensation of nitrogen-rich precursors are usually rich in pyridinic nitrogen. This species is responsible for enhancing the performance of electrode materials in electrochemical energy storage devices, due to the strong interaction with metal ions or the electrolyte. On the other hand, this type of nitrogen functionality is decreasing the electric conductivity of carbonaceous materials, making them less attractive for such applications. An optimal solution can be accomplished by a formation of a composite between nitrogen-rich carbon material and a conductive pristine carbon, which enhances the rate capability and energy storage capacity in sodium-ion capacitor anodes. The performance was improved as compared to the individual compounds, indicating the cooperative effects in this composite, as well.[138]

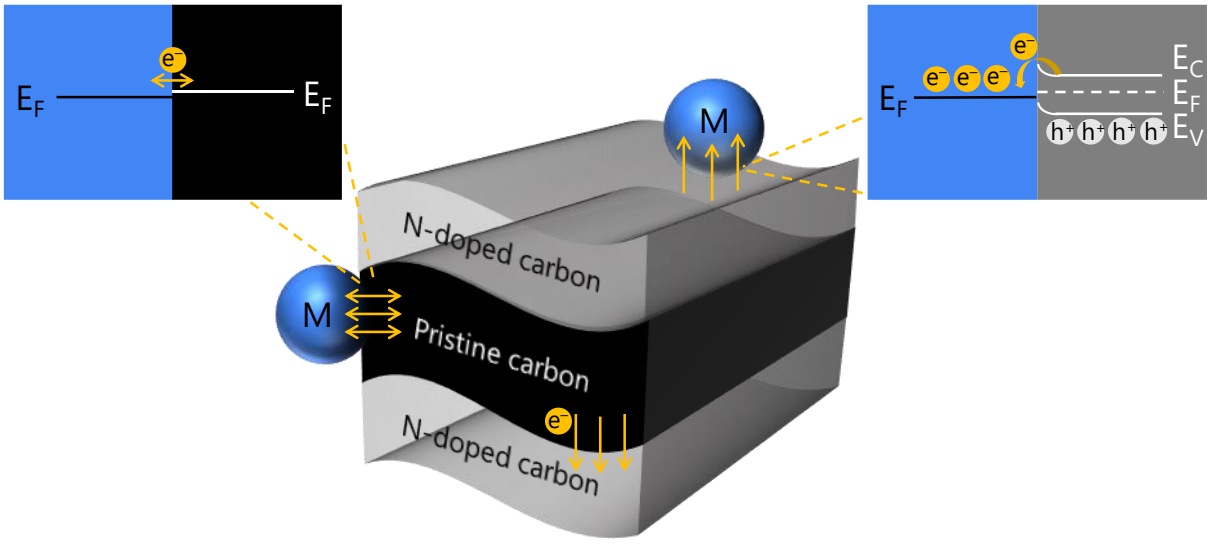

Figure 2.6. *Illustration of the electronic effects occurring upon functionalization of carbon with N-doped carbon, or with metallic species, and upon functionalization of N-doped carbon with metallic species.*

2.3.3. Metallic Species Functionalization

Already at the beginning of the last century, it was recognized that activated carbon, used as an adsorbent in gas masks, could also accommodate metals on its surface.[139] Immobilization of metallic species in the form of nanoparticles (NPs; size between 1 and 100 nm) or single atoms/ions on porous carbons is one of the most prominent applications of these materials.[140] For more than a century, carbons are used in the field of heterogeneous catalysis as support materials for the active phase of a catalyst in order to enhance its activity and stability. Among other notable characteristics that porous carbons offer as supports, which will be the focus of the following chapter, they are often preferred materials due to their catalytic inertness. Nonetheless, this is only partially true, as numerous effects can influence the catalytic reaction in which they are involved.

Adsorption mechanisms of guest species (thereby also metallic species) on porous materials are dictated by their porosity and surface properties. Since porous carbons are abundant in defects where many electron lone-pairs are localized, their surface offers plenty of reactive sites for anchoring metals.[141] Furthermore, incorporation of heteroatoms into their backbone induces electron relocalization, increases the number of electron donor functions, and thus the stability of metallic species on the support.[142-143]

There are various kinds of interactions that can occur between metal and support, among which the most important ones are geometric and electronic effects.[144] The geometric influence that carbon can have on a metallic NP is lattice strain, as a consequence of structural mismatch at the NP–support interface. Strained overlayers induce changes in reactivity because of a shift in the center of the metal *d* bands.[145-146] Electronic effects are essentially charge transfer, comparable events as in the formation of composites, described in the previous chapter. If there is a difference between Fermi levels of metal and carbon support, an electron transfer occurs when the interface between the materials is created (**Figure 2.6**).[147] The creation of a charged interface is similar to a formation of "dyadic structure" on the semiconductor interface, which is described as the Mott–Schottky effect.[128] The magnitude of this interaction is strongly dependent on the metal particle size and the nature of the support, but also on the nature of the metal itself.[148-150] The direction of the charge transfer depends on the work functions of carbon and the immobilized metal, and as such can vary significantly with the structure of carbon, presence of defects, and surface chemistry. "Typical" porous carbon rich in defects and without heteroatom doping has a comparable work function with the metal, leading to a free electron flow between these two materials, in both directions. Doping with nitrogen reduces the work function of carbonaceous material, and by opening the band gap induces the Mott-Schottky barrier at the junction between the metal and support. This directs the electron flux from nitrogen-doped carbon towards the metal. Charge transfer has increasing importance with decreasing metal particle size, being the most pronounced for isolated atoms.[33] Single-site catalysts have attracted more attention in recent years, because they exhibit more exposed active sites per unit mass of the catalyst, and have the highest atom utilization. Embedding single atoms into a carbonaceous network usually requires heteroatom doping, to form appropriate "ligand" that will stabilize metal atoms by complexation.[151]

2.4. Applications of Porous Carbon Materials

Previous chapters gave a general overview of the versatility that carbon materials offer, as well as the possibilities of tailoring their properties for specific requirements. Decades of research have led to the development and optimization of this class of porous materials for

the various applications where thermally and chemically stable materials are desired. In different applications, carbons have to fulfill very different demands, meaning that a broad set of parameters has to be precisely adjusted to construct an optimized material. Electric conductivity and high surface area make porous carbons suitable electrode materials for energy storage devices.[31] By doping carbons with heteroatoms and tuning their pore size, efficient selective gas adsorption and separation can be achieved.[106, 152] They are also commonly used as adsorbents in the liquid phase separations, especially for adsorption of dye molecules in the wastewater treatment,[153] filtration of drinking water,[154] or adsorption of heavy metal ions.[155] In catalytic applications, carbons are utilized either as support materials for catalytically active metallic species or even as catalysts themselves. Requirements that are important in catalysis and electrochemical energy storage are combined when carbon-based materials are used in electrocatalysis. The following chapters are introducing two different applications of carbons, Chapter 2.4.1 representing a future promising field of application that includes chiral separation, asymmetric catalysis, or chiral sensing, and Chapter 2.4.2 describing a classical use of carbons in the field of heterogeneous catalysis.

2.4.1. Chirality-Related Applications

In the middle of the nineteenth century, Pasteur discovered that certain crystals are optically active, and concluded that for each optically active substance inducing rotation in the plane-polarized light to the right there has to be an identical substance inducing rotating to the left.[156-157] This is marked as a discovery of enantiomers, defined as the non-superimposable objects related to each other by the mirror symmetry. Enantiomers are energetically degenerate with one another and share the same physical properties, such as melting and boiling point, color, density, etc. Since this discovery, chirality is considered as a fundamental criterion for life. Chirality (from Ancient Greek ‘cheir’ meaning ‘hand’) is a geometrical property describing the fact that the mirror image of an object is not superimposable with the original. Chirality matters when one chiral compound reacts with another chiral compound, which is of crucial importance because nature is comprised of chiral entities. Organic molecules essential for life, such as amino acids, nucleic acids, and sugars, are chiral and almost exclusively present in nature in only one enantiomeric form

(that is, enantiopure). Humans can sometimes distinguish between two enantiomers of certain compounds by smell (e.g., terpene (R)-limonene smells like orange, (S)-limonene smells like lemon) because our odor receptors are chiral. The infamous example of the importance of enantioselectivity is medication thalidomide, whose racemate (equal amounts of the enantiomers) was prescribed in the 1960s to pregnant women against morning sickness. However, the D enantiomer of thalidomide has the desirable tranquilizing properties, but the L enantiomer is teratogenic and causes malformations in embryos. This constitutes the principal concepts in pharmaceutical design, as the biological activity correlates with the chirality of a chemical compound. Therefore, the production of enantiopure compounds is necessary for the pharmaceutical and agricultural industry, and this is usually accomplished through the asymmetric synthesis or chiral separation.[158-162]

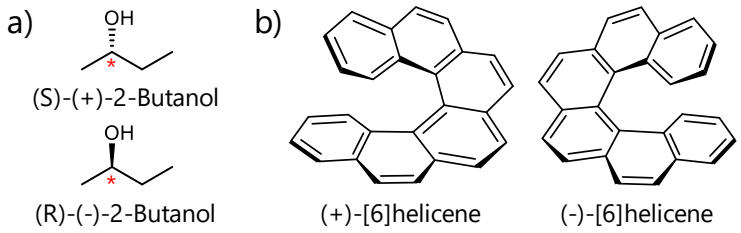

Figure 2.7. *Examples of chiral molecules that a) possess a chiral center, and b) without a chiral center.*

In organic chemistry, any atom (usually an sp^3-carbon atom) that forms bonds to four different atoms or groups of atoms is a chiral center (e.g., carbon atom marked with a star in **Figure 2.7a**). Nevertheless, molecules can express chirality without possessing any chiral center, known from helicene molecules that form a helical structure (**Figure 2.7b**). In nanoscience and materials chemistry, the chirality of nanostructures is present on atomic, but also on the nanoscale, and sometimes even larger scales.[163-165] In separation sciences, the processes are usually based on chromatographic techniques or capillary electromigration techniques. Asymmetric synthesis and catalysis, and chiral separation are foundations for obtaining necessary enantiopure chemicals. Logically, the development of asymmetric sensing will follow, in order to monitor the chiral composition of the product. Chiral sensors respond to an enantiomeric excess by a proportional change of conductivity, reflectivity, or magnetism. The enantiomers are separated through the interaction with a

chiral selector, which is either attached to a solid support or added to a mobile phase or background electrolyte.[14, 166-167] Solid supports are often designed to be porous, in order to increase the available surface area for functionalization with chiral moieties and make the separation processes more efficient. Silica is commonly used in these applications, because of their well-defined surface chemistry. Typically, terminal silanol groups are covalently modified by linker moieties like alkyltrialkoxysilane, phosphonate, carboxylate, amine, and others.[168-169] In recent years, metal-organic frameworks (MOFs) have emerged as another class of porous materials used for chiral separation. Homochiral MOFs are most commonly obtained from metal-containing nodes and enantiopure organic linkers, although other strategies are also possible.[170-171] Stereoregular chiral polymers are also utilized in enantioseparation, and they have been obtained by polymerization or by modification of natural polymers.[172-173] Silica, MOFs, and polymers have major drawbacks in terms of low stability in the extreme pH regions. Besides, a large limitation in the utilization of MOFs and polymers is their low thermal stability, and moisture sensitivity of MOFs.

One of the main challenges of asymmetric separations is the poisoning of the adsorbent, which can hardly be overcome by regeneration if the materials are thermally and chemically sensitive.[174] Materials that have superior thermal and chemical stability and express electric conductivity are porous carbons. They can potentially be used in chiral separations, either classically or controlled by an applied electric potential. Their conductivity opens up the possibility of utilization in asymmetric electrocatalysis or as chiral sensors.[175-177] Carbon nanomaterials with higher degrees of atomic order, such as carbon nanotubes (CNTs), fullerene, or graphene can be easily functionalized with chiral moieties, due to their well-defined surface chemistry. The reaction usually takes place on the more reactive sites of the material, such as the cap of the CNT, an edge of graphene, or defect sites.[178-180] However, these nanostructured carbons are not intrinsically porous, and they cannot be tailored for the different uses. Therefore, porous carbons are suitable versatile materials for chirality-related applications.[124-125] As mentioned in Chapter 2.3, the controlled functionalization of the surface of carbons is rather challenging because of the electronic heterogeneity of the individual atoms in the network. A promising approach

for uniform inclusion of chiral information into the carbon materials is a synthesis from an intrinsically chiral precursor. One class of carbon precursors discussed previously are ionic liquids (ILs). Their cations or anions can be designed to contain chiral information, and as such are already used as mobile-phase additives in chromatography, background electrolyte additives or selectors in capillary electrophoresis.[181-182] Their usage can be extended from a chiral additive to a chiral selector by applying them as chiral carbon precursors.[124-125] The porosity of resulting carbon materials can be created by various templating approaches described in Chapter 2.2. Development of novel chiral porous carbon materials and strategies for obtaining them can enable their application in chiral separation, asymmetric catalysis, as well as chiral sensing.

2.4.2. Nanoparticles in Heterogeneous Catalysis

Ground and commodity chemicals as well as other critical materials of modern societies are obtained by industrial processes involving catalysis. Catalysts have revolutionized both industry and academia, and they represent essential factors in our everyday life. A catalyst is defined as a substance that increases the rate of reaching chemical equilibrium, and at the end of a catalytic cycle, it regenerates to its original form. According to Sabatier, a good heterogeneous catalyst exhibits an intermediate strength of interaction with the reactants, products, and intermediates. The heterogeneous catalytic process can be described in a series of elementary steps, including 1) diffusion of the reactants through a boundary layer surrounding the catalyst, 2) diffusion into the pores of the catalyst, 3) adsorption of the reactants onto the active sites, 4) surface reactions, 5) desorption of the products from the active sites, 6) diffusion of the products from the pores of the catalyst, and 7) diffusion of the products across the boundary layer surrounding the catalyst.[3, 183-186] As it was illustrated in Chapter 2.3.3, carbon materials (or generally any kind of support material) and nanoparticles (NPs) deposited on it cannot be considered as independent systems. Figuratively speaking, in heterogeneous catalysis, the support acts as ligands in homogeneous catalysis. The main role of the support is to stabilize the active phase of the catalyst throughout the catalytic reaction, but it can also affect the active phase by charge transfer, or it can be directly involved in catalysis.[4, 187-189]

Properties of materials (especially metals) vary with size once their size is below 100 nm, and these variations arise from scalable and quantum effects. Scalable effects stand for surface-to-volume ratio, which increases with decreasing particle size. The simplest model for describing quantum effects is a particle in a box, where small clusters have discrete energy levels, and these effects are getting more pronounced as the size of the NP decreases. One of the most important parameters for understanding the catalytic activity of NPs is the coordination number, defined as the number of nearest neighbors. The simplified model of a crystal surface constructed from cubic atoms can be used to illustrate the coordination number (**Figure 2.8**). Each of the nearest neighbors bound through a face of the cube contributes with a certain binding energy to the stabilization of an atom. The numbers shown represent coordination numbers, and they are the first measure of the energy of an atom, the most stable being the one in the bulk (number 6, not depicted), and the least stable being the surface adatom (number 1). This is due to the degree of unsaturation of their bonds, and it directly relates to their ability to catalyze chemical reactions.[16, 140, 190-191] In a similar sense, carbon materials can serve as catalysts on their own, due to their defective surface, through the introduction of heteroatoms, or formation of heterojunctions.[35, 192]

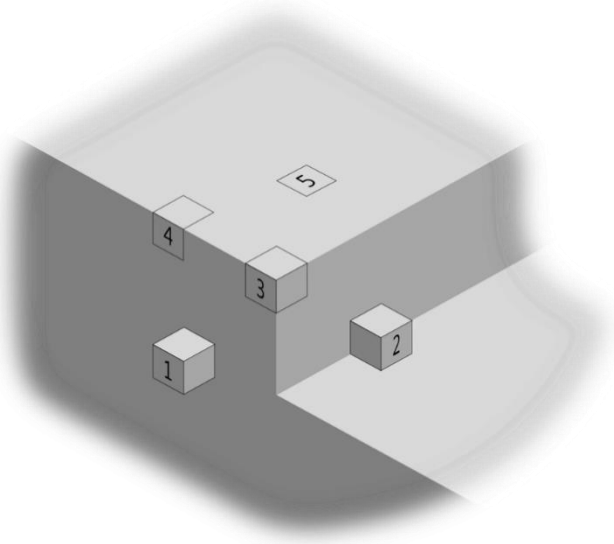

Figure 2.8. *A simplified model of a crystal surface presenting various sites, 1: surface adatom, 2: step adatom, 3: corner atom, 4: edge atom, 5: surface atom.*

To truly utilize the catalytic properties of NPs, it is crucial to control their size, shape, and dispersity. This is accomplished by immobilizing and stabilizing them on the surface of porous materials. Along with their properties that make them suitable for numerous applications, such as high surface area and tailorable pore architecture, some of the features of carbon materials make them especially attractive materials for catalysis. The most notable properties of carbon supports are: 1) resistance in extreme pH regions, 2) stability on high temperatures, 3) easy reduction of metallic phase, 4) possibility of preparing a catalyst in different macroscopic forms (pellets, fibers, monoliths, cloths, etc.), 5) simple recovery of the active phase, and 6) low cost.[33-34, 193]

The effects induced by metal–support interactions described in Chapter 2.3.3, such as charge transfer and strain, can have a direct influence on the catalysis of NPs. Usually, the effects important for catalytic activity and selectivity are studied on systems where reactants are only in the gas phase or only in the solution. However, a large number of catalytic processes are taking place on the surface of supported NPs that are in the reaction solution, where one of the reactants is a gas. Due to the complexity of this system, comprising of solid, liquid, and gaseous state, it is viable to study the effects on catalytic activity using a simple model reaction. One of such widely studied reactions is partial glucose oxidation with molecular oxygen, over AuNPs supported on porous carbons.

Oxidation of Glucose With Molecular Oxygen over AuNPs Supported on Porous Carbons

Partial oxidations of biomass compounds like alcohols and carbohydrates are important reactions for producing higher value-added chemicals, used in food, pharmaceutical, and detergent industry. They are often accomplished through enzymatic and microbial oxidation or homogeneous catalysis, but the advantages of heterogeneous catalysis have led to the considerable development of oxidation over supported NPs.[194-196] Efforts for making the heterogeneously catalyzed oxidations more environmentally benign yielded in replacing traditional stoichiometric oxidants by molecular oxygen. Notwithstanding the high productivity of gas-phase oxidations in continuous-flow reactors at elevated temperatures, these processes are limited to volatile and thermally stable reactants and products. Besides, the metal NPs of the catalyst must also be resistant against sintering and

oxidation, and the porous support must be stable in the oxidative atmosphere at high temperatures. Therefore, it is more viable to perform these oxidations in the liquid phase. These reactions are typically highly selective under mild conditions, making them good candidates for model systems.[197-198]

Being the main constituent of cellulose, starch, and crop stover, glucose is especially suitable model reactant because of its low cost, high abundance, and simple production from biomass. The main product of glucose oxidation is gluconic acid (or its salts), and they serve as important biodegradable chelating agents and intermediates in food, pharmaceutical, and concrete industry.[199-201] The rate of oxidation and selectivity towards the desired product depend on many factors, including the choice of metal and the size of the NP, choice of support, as well as conditions such as pH of the aqueous solution of glucose, temperature, and the stirring rate. A number of catalysts investigated for this reaction consist of NPs of metals from the Pt group, but these suffer from deactivation due to over-oxidation and poisoning.[202-203] A suitable alternative is gold, which is highly active below a NP size of 10 nm, and highly selective towards gluconate.[204-206] Porous carbons are proven to serve as good support materials for AuNPs, and they have been utilized in different morphologies, porosities, and surface chemistries.[207-212] Sugars are primarily in the cyclic form in neutral water, whereas acidic and basic conditions catalyze their ring-opening. The high rate of glucose oxidation in mildly basic conditions is a consequence of the rapid reaction of an aldehyde, which is the ring-open form of sugar. Supported AuNP-catalyzed glucose oxidation is highly selective towards gluconate in moderate temperature and mildly basic conditions since the isomerization of glucose is catalyzed by the solution medium. At pH 7, isomerization to fructose starts at 70 °C, and at pH 9 already at 50 °C. Small quantities of other byproducts such as sorbitol, mannose, glycolaldehyde, and maltose were observed above 70 °C at pH 9.5.[213]

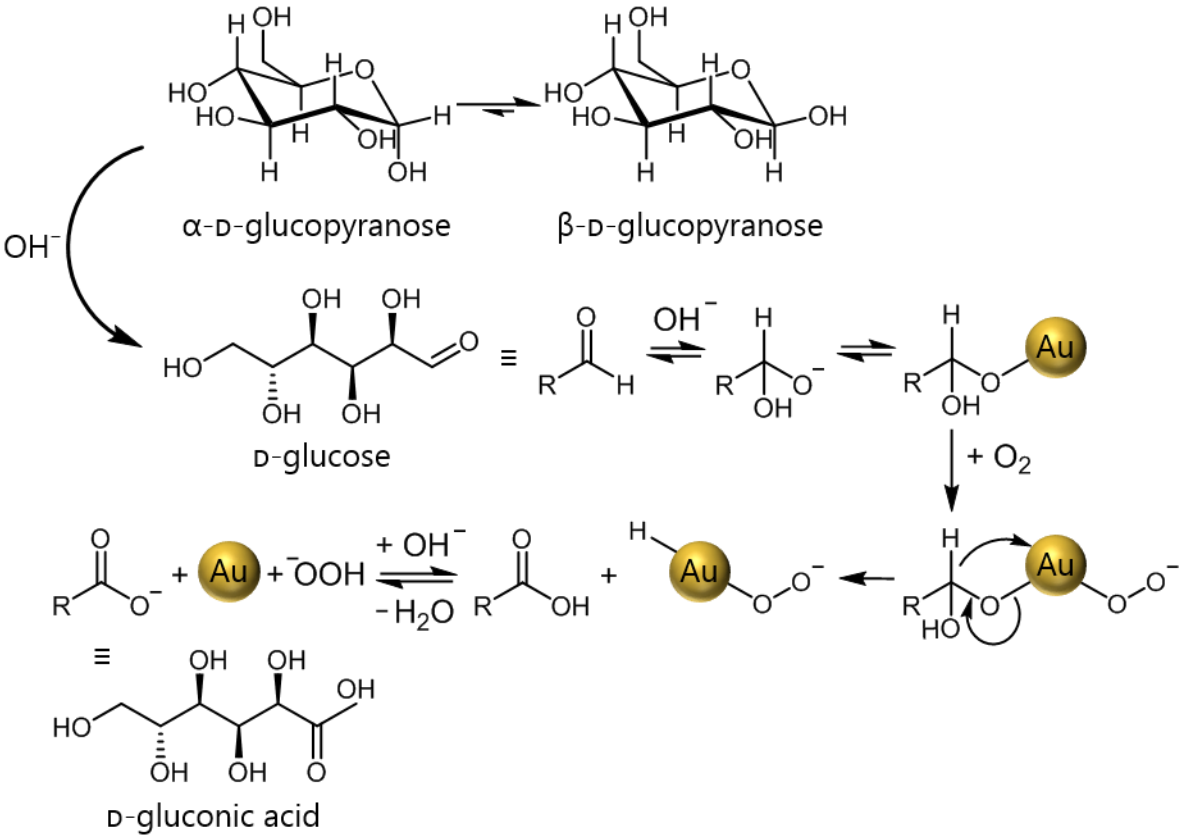

Figure 2.9. *Proposed mechanism of glucose oxidation to gluconic acid in basic medium.*

Glucose oxidation with molecular oxygen to sodium-gluconate catalyzed by supported AuNPs is believed to be a two-electron process following the Langmuir-Hinshelwood mechanism (**Figure 2.9**). Aldehydes in water undergo reversible hydration to geminal diols, and this is further accelerated at higher pH. Both diol and dioxygen adsorb on the Au surface, forming metal alkoxide and O_2^-, respectively. The adsorption of both substrates is supported by kinetic studies showing that the reaction order with respect to glucose and oxygen is lower than one.[208, 214] A β–hydride elimination of the geminal diol results in the formation of gluconate, a process that is facilitated by adsorbed hydroxide from the solution. The remaining hydrogen and the O_2^- species react, producing peroxide species, which can further react with water or decompose on the surface. The intermediate hydrogen peroxide decomposes under basic conditions, thus its role in the reaction as an oxidant can be ruled out.[215-218]

Because of its high activity and selectivity, the aforementioned reaction can serve as a suitable model system for studying support effects, in particular the interesting and important processes at the interfaces formed between gas, liquid, and solid.

3. Outline

As it was mentioned in the Motivation, the knowledge behind porous carbon materials is large, and the structure-related properties of these materials are widely studied. However, their further utilization in industrial applications requires an even better understanding of their porous structure, surface chemistry, and related properties. This thesis has the aim of broadening the fundamental knowledge of porous carbons, through studies on model systems and novel applications. This has been accomplished by using some of the synthesis approaches towards porous carbons described in Chapter 2.2. Different modes of templating are employed throughout this work, as they enable the controlled design of the porous architecture of materials. Furthermore, different applications of the prepared materials require various ways of functionalization, as was described in Chapter 2.3.

A rather novel potential application of carbon materials in chirality-related applications is reported in the present work. The method of nanocasting with chiral ionic liquids as carbon precursors is utilized for the synthesis of porous carbons with an enantioselective surface. This will be the content of Chapter 4.1. The interactions of the prepared materials with chiral compounds from the solution and the gas phase are tested. Chiral ionic liquids are used for the preparation of another set of carbons with an enantioselective surface in Chapter 4.2, although following a different approach. The creation of chirality is decoupled from the creation of porosity, and that through the formation of carbon–carbon composites. Their chiral interactions are also measured in the presence of a solvent, as well as in the gas phase.

Coordinative functionalization of carbons with metallic species yields catalysts with remarkable activity in the oxidation of glucose with molecular oxygen as will be reported in Chapter 5. This model reaction with selective catalysts consisting of gold nanoparticles on porous carbon supports serves as a good ground for studying the interactions happening on the interface between gas, liquid, and the solid. Chapter 5.1 demonstrates how the catalytic activity can be controlled by tuning the local environment of the active phase, through the confinement of the solvent in the pores of carbon material. The control that is established over the catalytic activity in this indirect way is employed in Chapter 5.2

for further increase in the local concentration of reactants by using perfluorocarbons, compounds with high gas dissolving capabilities. The properties of perfluorocarbons are combined with the gold-on-carbon catalyst to create particle-stabilized emulsions that are promoting the oxidation of glucose.

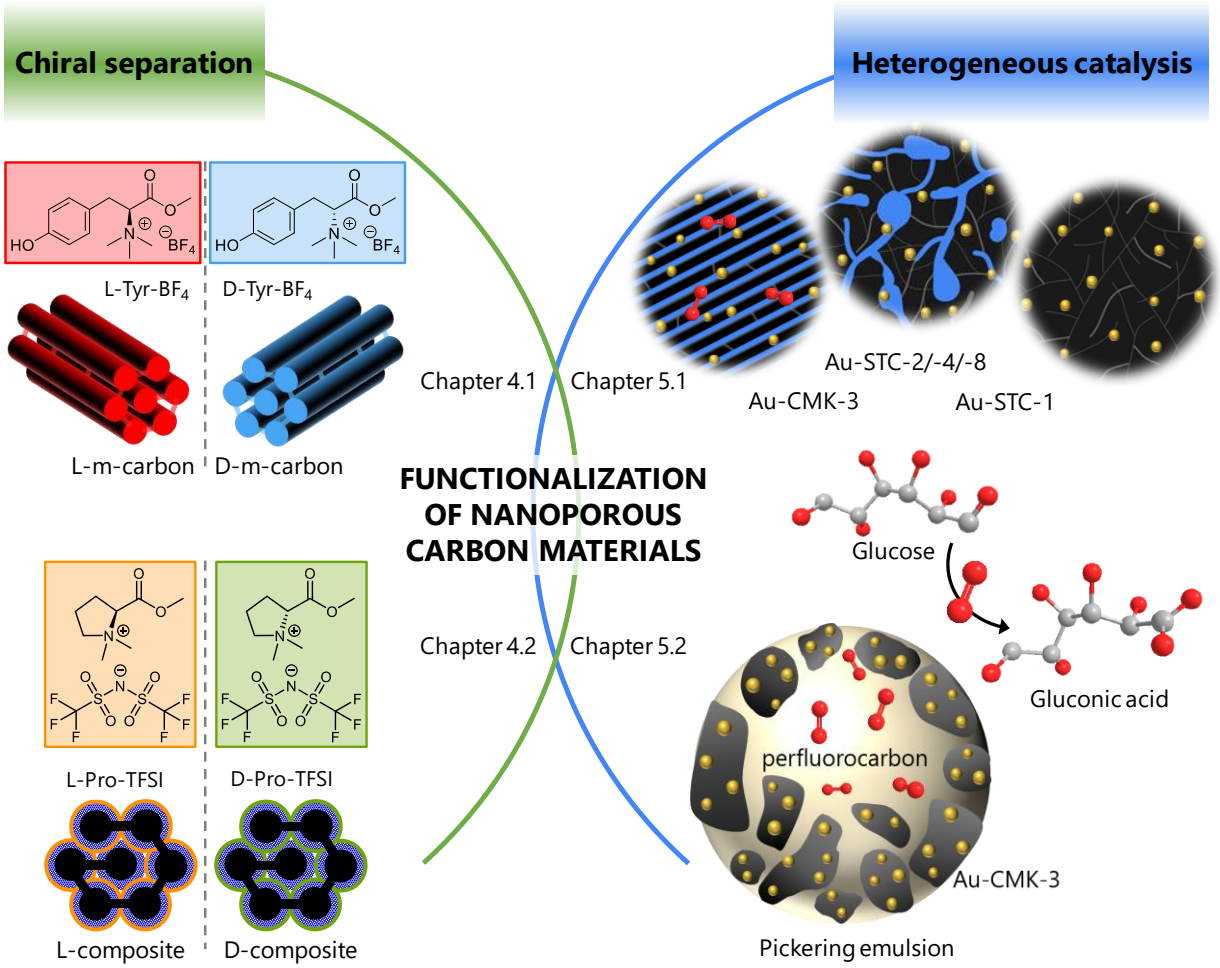

Figure 3.1. *Graphical overview of the materials reported in the thesis, together with their applications.*

4. Interaction of Carbon Materials with Chiral Species from the Solution and the Gas Phase[2]

The Chapter 2.4.1 revealed the importance of chirality in chemistry, catalysis, and synthesis of pharmaceuticals. Considering that chirality is of importance only when one chiral species is interacting with another chiral species, designing a suitable adsorbent material requires delivering chiral information into its structure. As it was previously emphasized, utilization of porous carbons for chirality-related applications has several benefits over commonly used porous materials. Their superior thermal and chemical stability are properties useful in various applications, but the possibility to tailor their pore size over a broad range is especially suitable for the adsorption of gases or molecules from the liquid phase.[29, 154, 220] In addition, carbons with hierarchical pore structure can be more easily synthesized, which is a valuable property for adsorption at high rate with unrestricted transport.[45, 59] In the context of enantioselective adsorption processes, asymmetric catalysis, or chiral sensing, electric conductivity is a unique intrinsic property of carbons.[175, 177, 221]

However, obtaining carbon materials with uniform distribution of chiral functionalities is rather challenging because the atoms of their network are usually chemically and electronically heterogeneous.[95] Thus, the synthetic approach that will be presented within this Chapter is based on direct carbonization of a chiral precursor, as this brings the chiral information into the resulting carbons in more regular manner. Together with strategies for heteroatom doping mentioned in the Chapter 2.3.1, like condensation of molecular building blocks, carbonization of metal-organic frameworks or porous polymers, usage of ionic liquids as chiral carbon precursors is an especially promising approach. The design of chiral ionic liquids (ILs) is feasible due to the possibility of tuning the cation and ion pairs. The first studies reporting the synthesis of enantioselective porous carbons have

[2] The results of this chapter are adapted with permission from the original work of the author:
[1] Perovic, M., Aloni, S. S., Mastai, Y., and Oschatz, M.: Mesoporous Carbon Materials With Enantioselective Surface Obtained by Nanocasting for Selective Adsorption of Chiral Molecules From Solution and the Gas Phase. *CARBON* 2020, *170*, 550 – 557. (Ref.[219])
[2] Perovic, M., Aloni, S. S., Zhang, W., Mastai, Y., Antonietti, M., and Oschatz, M.: Towards Efficient Synthesis of Porous All-Carbon-based Nanocomposites for Enantiospecific Separation. 2020, in preparation.

also used chiral ILs with the help of eutectic salt melts for establishing porosity.[124-125] Nevertheless, the inorganic salts used as templates act as Lewis acids and have strong interactions to polar ILs and the corresponding heteroatom-doped carbons. As mentioned in the Chapter 2.2.2, this results in high amount of residual inorganic impurities. Moreover, the resulting materials have a rather broad pore size distribution, dominated by small pores, which can hinder the thermodynamics of the adsorption. The efforts in developing carbon materials that possess chirality without chiral center resulted in right-handed helical cellulose-based carbon that adsorbs one enantiomer of tannic acid from the solution over the other.[222] This material, however, does not have its mirror-image counterpart, which may limit its field of application. Besides, its pore architecture cannot be tailored, and the pore sizes are distributed over a wide range of diameters.

To meet the demands of efficient adsorption, hard templating can be employed for narrower pore size distribution and better connectivity of the pore system.[61-62] This method, described in Chapter 2.2.2, is well established for achieving high surface area carbons, but the spatial confinement simultaneously prevents the thermal decomposition of the precursor.[115, 121] This is particularly important when the carbon precursor is IL without cross-linkable functional groups. In the following Chapter 4.1, a new synthetic approach towards mesoporous carbon materials with enantioselective surface is presented.

Despite their desirable properties as carbon precursors, ILs are a class of materials that are relatively high-priced. For a better economic utilization of these materials, a composite between IL-derived carbon and an inexpensive carbon material might be a good compromise.[96, 126-127, 136] This strategy is employed in Chapter 4.2, where a composite between pristine mesoporous carbon and chiral IL-derived carbon is prepared. The two sets of novel enantioselective carbon materials are applied for the chiral recognition of molecules in the gas phase, as well as in the solution.

4.1. Mesoporous Carbon Materials with Enantioselective Surface obtained by Nanocasting

Present study employs the method of nanocasting for the synthesis of porous carbon materials with enantioselective surface, in order to obtain larger pores with sufficient connectivity. Two mesoporous carbon materials with a different (mirror image) chirality are synthesized by infiltration of ordered mesoporous silica template, SBA-15, with chiral IL. The relatively low carbonization temperature of 500°C, as well as spatial confinement by hard template, allow for retention of chiral information originating from IL in the final carbonaceous material. The interaction of these novel carbon materials with chiral species from the solution shows specific interaction with the preference for one enantiomer of the same compound. The same is observed for the interaction of the carbons with chiral vapors.

4.1.1. Synthesis and Characterization of Mesoporous Carbons with Enantioselective Surface

Two mesoporous carbons were obtained by impregnation of ordered mesoporous silica, SBA-15, with an enantiopure solution of chiral IL and trimesic acid, followed by carbonization and finally a template removal (**Figure 4.1**).[67] Chiral ILs employed in the synthesis were N,N,N-trimethyl-L-Tyrosine methyl ester tetrafluoroborate (L-Tyr BF_4, in red rectangle in the **Figure 4.1**), and its D-enantiomer (D-Tyr BF_4, in blue rectangle in the **Figure 4.1**).[124, 223]

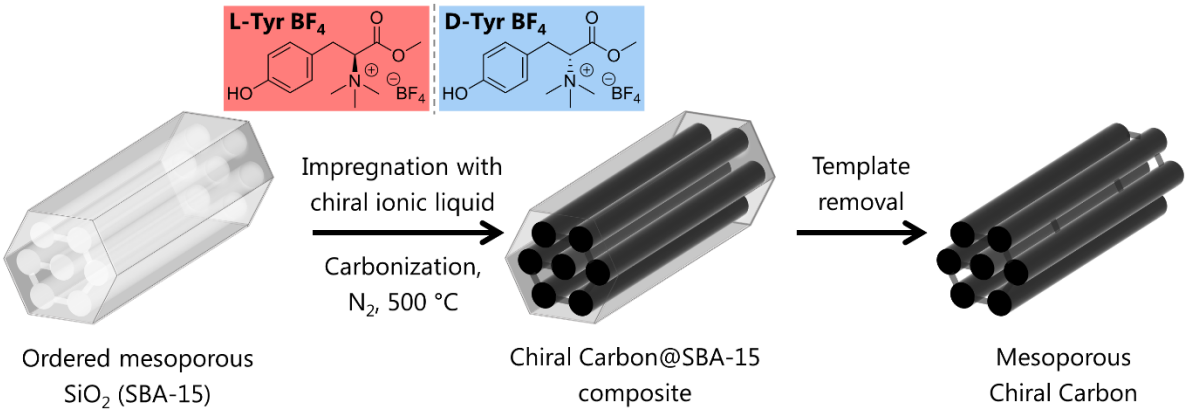

Figure 4.1. *Synthesis procedure of mesoporous carbons with enantioselective surface.*

Chiral ILs and trimesic acid have the role of chiral carbon precursor, and a crosslinking agent, respectively. The resulting carbonaceous materials are denoted as L-m-carbon and D-m-carbon, where "m" stands for "mesoporous". To minimize the decomposition of chiral precursor and prevent the unwanted reactions of chiral functional groups, materials were synthesized on a relatively low carbonization temperature of 500°C. Nitrogen physisorption isotherms (–196 °C) of the composite between chiral carbon and the SBA-15 silica template reveal that the filling of the pores of the silica was successfully accomplished (**Figure 4.2a**). This is supported by values of (multi-point) Brunauer–Emmett–Teller specific surface areas (SSA_{BET}) that decreased from 845.1 $m^2\ g^{-1}$ in SBA-15, to ≈ 43 $m^2\ g^{-1}$ in composites. The pore size distribution (PSD) of the materials before the template removal is rather broad, with no distinct prevalence of one porous system (**Figure 4.2b**).

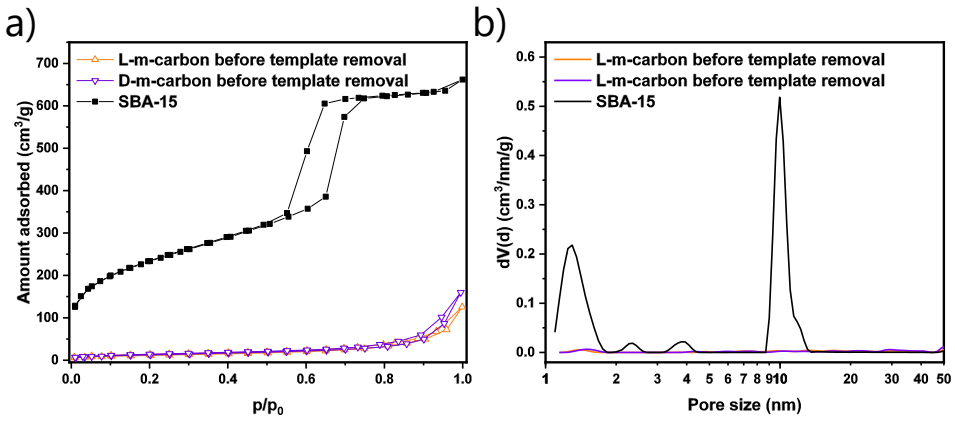

Figure 4.2. *a) Nitrogen physisorption isotherms (at –196 °C) with the corresponding b) semi-logarithmic plots of differential pore size distribution calculated with QSDFT (N_2 on carbons with slit/cylindrical/spherical pores at 77 K, adsorption branch kernel) of SBA-15 and carbon materials before template removal.*

After the removal of the silica template, final carbon materials with chiral surface were obtained. Results of the nitrogen physisorption experiments (–196 °C) show that the porosity of L-m-carbon and D-m-carbon is comparable, having mainly mesoporous structure (**Figure 4.3a**). According to the IUPAC classification, they display a type II isotherm with a H3 hysteresis loop, which points to a gradual monolayer – multilayer coverage of the adsorbent with adsorbate gas.[28] This shape of the isotherm reveals that there is no major pore blocking or cavitation effects during the adsorption, meaning that

the pore system of these materials is well accessible for guest molecules under the measurement conditions. Moreover, the presence of hysteresis throughout the entire range of relative pressures suggests a non-rigid nature of these materials, due to the comparably low carbonization temperature.

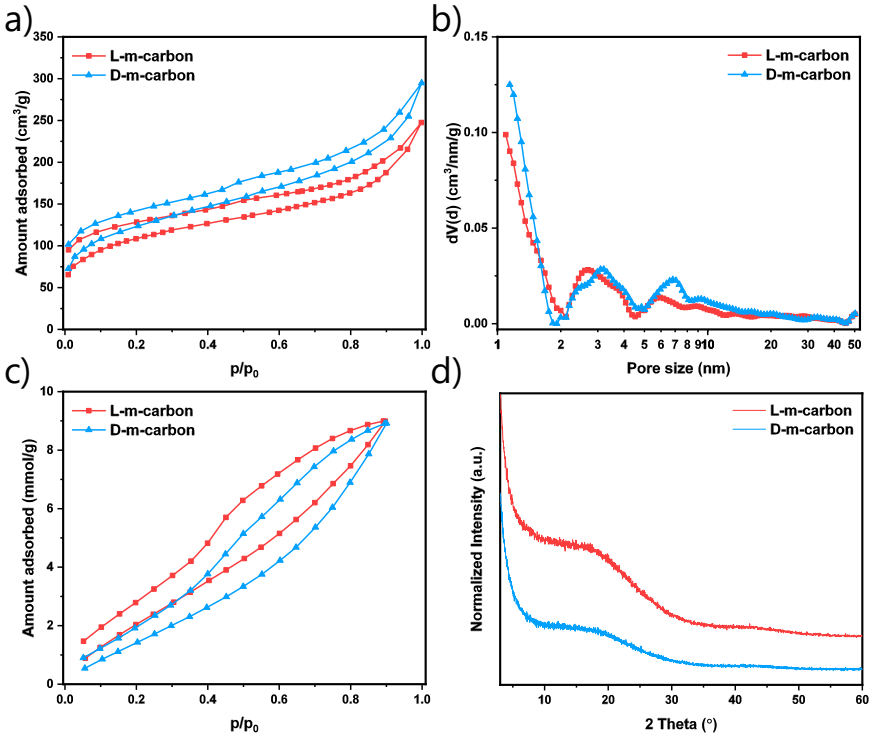

Figure 4.3. *a) N_2 physisorption isotherms (at –196 °C) with the corresponding b) semi-logarithmic plots of differential pore size distribution calculated with QSDFT (N_2 on carbons with slit/cylindrical/spherical pores at 77 K, adsorption branch kernel), c) water vapor adsorption isotherms (at 25 °C), and d) PXRD patterns of L-m-carbon and D-m-carbon.*

Table 4.1. *Specific surface area (SSA_{BET}) calculated using the BET equation, DFT micropore volume (V_{Micro}), DFT mesopore volume (V_{Meso}), and total pore volume (V_t), obtained from N_2 physisorption measurements (at –196 °C) of L-m-carbon and D-m-carbon.*

Sample	SSA_{BET} [$m^2\ g^{-1}$]	V_{Micro} [$cm^3\ g^{-1}$]	V_{Meso} [$cm^3\ g^{-1}$]	V_t [$cm^3\ g^{-1}$]
L-m-carbon	391.1	0.09	0.24	0.38
D-m-carbon	441.1	0.10	0.29	0.46

The pore size distributions (PSD) of L-m-carbon and D-m-carbon were analyzed using the quenched-solid density functional theory (QSDFT, adsorption branch kernel) for nitrogen adsorbed on carbon with slit/cylindrical/spherical pore shape, and were plotted as a semi-logarithmic plot (**Figure 4.3b**). Both materials have a very small volume of micropores, whose volume is below 0.1 $cm^3\ g^{-1}$ (**Table 4.1**). They exhibit relatively broad PSD or large mesopores, and a narrow PSD of the smallest mesopores centered around 3 nm. The mesopore volumes of L-m-carbon and D-m-carbon are 0.24 and 0.29 $cm^3\ g^{-1}$, respectively, and their total pore volumes are 0.38 and 0.46 $cm^3\ g^{-1}$, respectively. The SSA_{BET} of the materials is in a comparable range, and equals to 391.1 and 441.1 $m^2\ g^{-1}$ for L- and D-material, respectively.

Water vapor adsorption measurements (25 °C) were collected to further analyze the pore structure and the surface chemistry of the obtained materials (**Figure 4.3c**). The low onset point of water adsorption in both materials is a consequence of adsorption of water on primary adsorption sites on the surface of the carbons. The presence of heteroatoms and polar functional groups on the surface these materials make their surface relatively polar and therefore prone to high water uptake at low relative pressure. Due to the broad PSD of these materials, water gradually adsorbs over entire range of relative pressures.[224-226]

X-ray powder diffraction (XRD) measurements of L-m-carbon and D-m-carbon show patterns that are typical for disordered porous carbon materials without apparent crystalline inorganic impurities (**Figure 4.3d**). Moreover, they reveal very broad (002) and (101) carbon peaks at ≈ 25° and ≈ 44° 2θ.

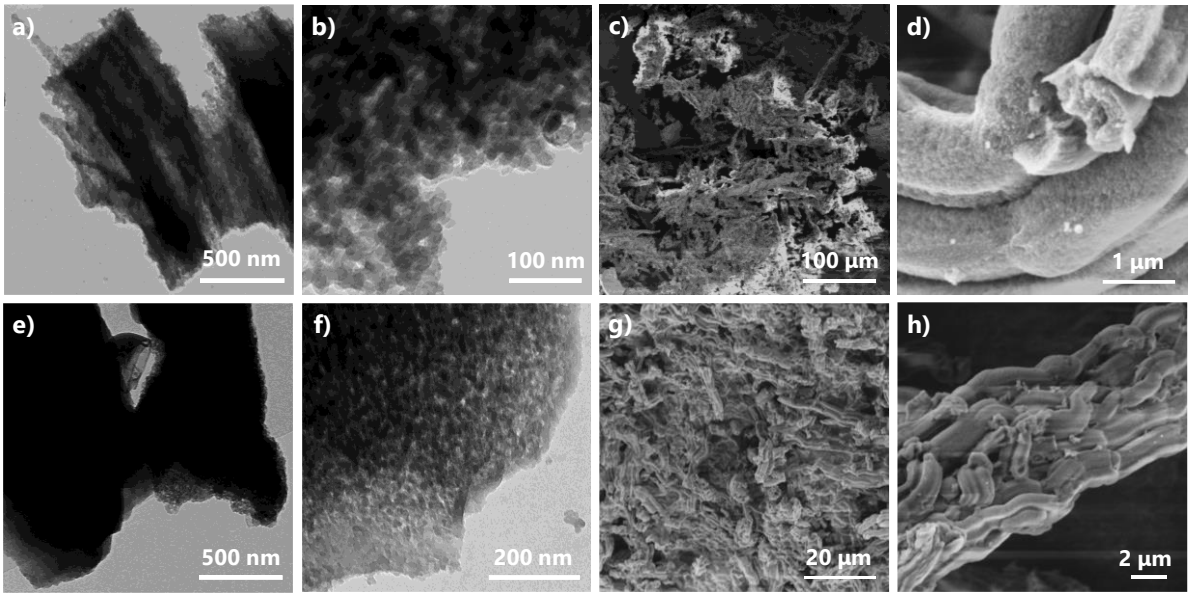

Figure 4.4. *Electron microscopy images of (a–d) L-m-carbon, and (e–h) D-m-carbon. TEM images are a, b, e, f, and SEM images are c, d, g, h.*

Transmission electron microscopy (TEM) images of the materials also confirm the similarity of two synthesized materials, independent of the chirality of the applied CIL precursor (**Figure 4.4**). Certain degree of directionality is observed in the form of nanorods, which originates from the cylindrically shaped mesoporous hard template used in the synthesis (**Figure 4.4a**). The morphology of L-m-carbon and D-m-carbon appears rather open, revealing the large amount of mesopores. As TEM, scanning electron microscopy (SEM) shows particle morphology that is comparable to the SBA-15 template and is typical for hexagonally ordered mesoporous materials (**Figure 4.4**).[67, 227] The electron microscopy investigations are revealing that the nanocasting approach can be successfully combined with the CILs as precursors and is thus applicable for the synthesis of porous carbon materials containing chiral information.

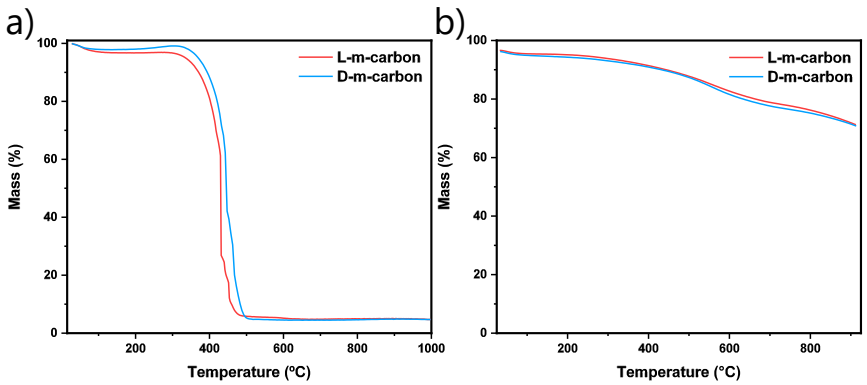

Figure 4.5. *Thermal analysis of L-m-carbon and D-m-carbon measured under a) synthetic air with a heating rate of 10 °C min^{-1}, and b) helium with a heating rate of 2.5 °C min^{-1}.*

To confirm the successful removal of the hard template and the absence of inorganic impurities in the carbon materials, thermogravimetric analysis (TGA) of the mesoporous materials was carried out under a flow of synthetic air (**Figure 4.5a**). Both samples show small ash-content (less than 5 wt %) at the temperatures above 500 °C, confirming the successful removal of SBA-15 after carbonization and washing with NaOH. TGA coupled with mass spectrometry (TGA-MS) under helium flow was employed to investigate the chemical functionalities present in the materials after the carbonization (**Figure 4.5b**). This allows determination of potential chiral functional groups that are still present after carbonization of the CIL precursors. Mass loss of around 30 % until 900 °C under helium shows that presumably a high fraction of heteroatom-containing groups together with some ordinary carbonization products are removed from the materials, since pure carbon materials are stable at high temperatures under an inert atmosphere. The temperature profiles of two carbon materials under synthetic air flow, as well as under helium flow are almost identical, which suggests that they have a comparable chemical composition. In addition, the temperature profiles of both ionic liquids under nitrogen flow are also comparable (**Figure S 1**, Appendix).

Table 4.2. *Elemental analysis and energy dispersive X-ray spectroscopy data summary of L-m-carbon and D-m-carbon. All the values are expressed in wt %.*

Sample	C		N		O_{EDX}	H_{EA}	S_{EA}	F_{EDX}
	EDX	EA	EDX	EA				
L-m-carbon	87.9	75.3	4.1	1.3	7.0	3.9	0.1	1.0
D-m-carbon	89.1	78.7	3.2	1.8	7.4	4.1	0.1	0.2

The bulk and surface chemical analysis of the samples was conducted through C/H/N/S elemental analysis (EA) and energy dispersive X-ray spectroscopy (EDX) (**Table 4.2** and **Figure S 2**, Appendix). The chemical composition of the carbons is very similar, and for both samples results in slightly higher values of nitrogen and carbon content given by EDX. This can be ascribed to several factors, including the polarity of the materials as a consequence of doping with heteroatoms. This makes the materials good adsorbents for moisture from air, which will constitute a part of the initial mass measured in EA. Other reason can also be that in EDX the sum of the contents of elements is normalized to 100 %. The remaining content of non-detected contributions in EA of both carbons is also comparable, 19 wt % in L-m-carbon, and 15 wt % in D-m-carbon. This can be attributed mainly to oxygen species, since the ash-content above 500 °C determined by TGA is less than 5 wt %, and thus there seems to be no major content of inorganic impurities.

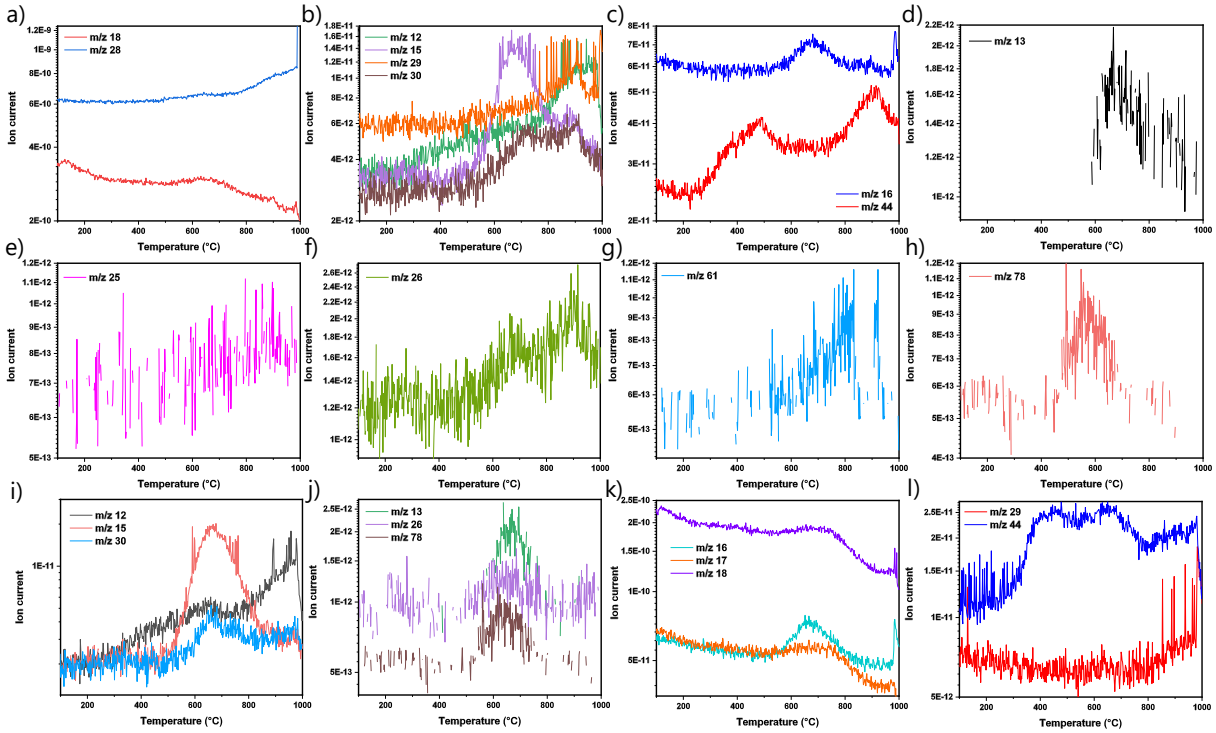

Figure 4.6. *Semi-logarithmic plots of MS ion currents obtained from TGA-MS measurements under helium of (a–h) L-m-carbon, and (i–l) D-m-carbon.*

Some of the most notable TGA-MS peaks emerging both for L-m-carbon (**Figure 4.6a–h**) and D-m-carbon (**Figure 4.6i–l**) are m/z 30, which is often denoted as a nitrogen indicator, 15 belonging to either NH or CH_3. m/z 26 is caused by CN or C_2H_2, and m/z 78 originates from benzene ring in the form of C_6H_6. Many of the observed peaks evolve from nitrogen-containing functional groups, which is important because nitrogen is a constituent of the functional group carrying the chiral information in chiral ionic liquid used as a precursor for the synthesis of mesoporous carbons (**Figure 4.1**). Structural characterization of L-m-carbon and D-m-carbon demonstrates that they have very similar porosity, morphology, and chemical composition of the bulk, as well as the surface of the materials. Therefore, it is expected that the differences in their interactions with enantiopure species from the solution, or the gas phase, will be caused the chiral nature of these carbon materials.

4.1.2. Interaction between Mesoporous Carbons with Enantioselective Surface and Chiral Species

Technique employed to determine the chiral nature of the prepared materials is isothermal titration calorimetry (ITC).[124-125, 228] ITC is commonly used for determination of the thermodynamic parameters of interactions in solution, and thus can be used for measuring the released or absorbed heat upon mixing of enantiopure compounds with chiral materials. For measuring the heat of interaction of studied carbons, small aliquots of enantiopure aqueous solutions of amino acids were injected into a dispersion of carbon in water (**Figure 4.7**). L-Phenylalanine (upper panel), and D-Phenylalanine (lower panel) were injected into dispersions of L-m-carbon (**Figure 4.7a**) and D-m-carbon (**Figure 4.7b**). From the measured heat flow upon titration with amino acid, it can be concluded that specific interactions between enantiomers of amino acid and carbon dispersed in water are occurring. Upon injection, the molecules of Phenylalanine adsorb on the pore walls of chiral carbon, which has to be preceded by desorption of water from the pore and its release in the bulk solution. The differences between the heat flow during adsorption of the amino acid and the heat flow caused by water desorption and dilution of solution are then recorded as an ITC signal. L-m-carbon has stronger interaction with D-Phenylalanine, with maximum heat flow of 25 μJ sec^{-1} per injection, than with L-Phenylalanine that causes maximum heat flow of 15 μJ sec^{-1} per injection (**Figure 4.7a**). As expected, the opposite

trend is observed for D-m-carbon, which has stronger interaction with L-Phenylalanine (maximum heat flow 17 μJ sec^{-1} per injection), than with D-Phenylalanine (maximum heat flow 12 μJ sec^{-1} per injection) (**Figure 4.7b**).

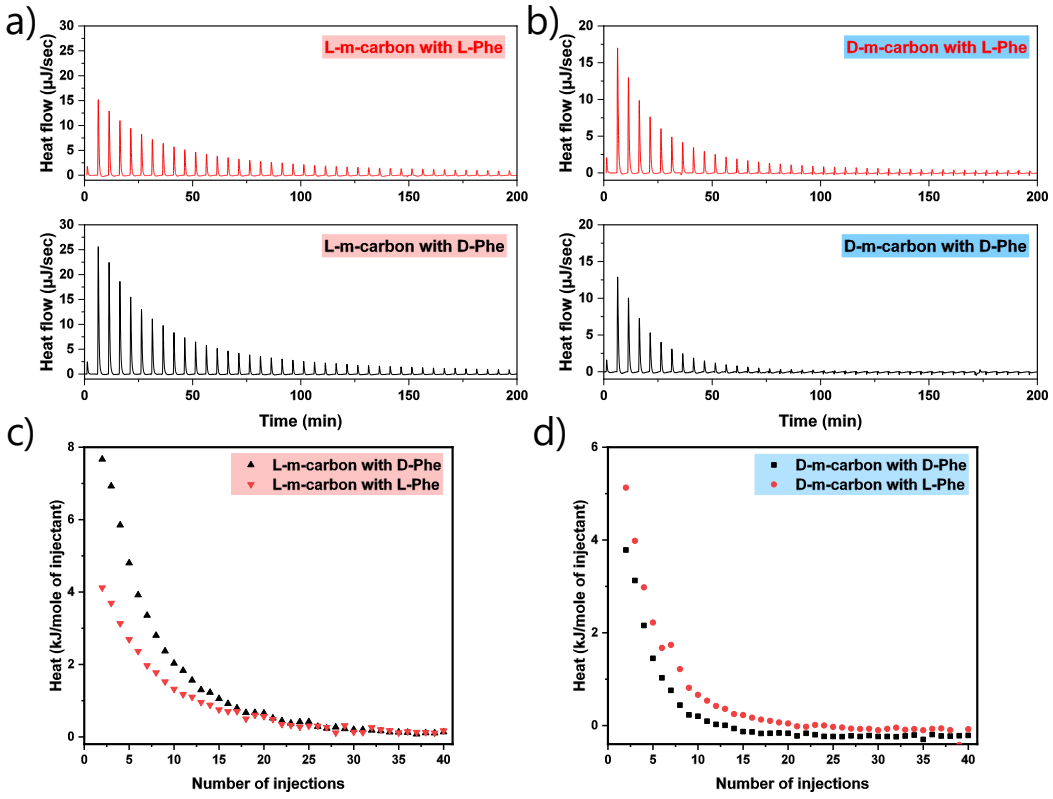

Figure 4.7. *a) and b) Raw isothermal titration calorimetry data from injecting L-Phenylalanine (upper panel), and D-Phenylalanine (lower panel), into a dispersion of a) L-m-carbon, and b) D-m-carbon. Heat per mole of injected D-Phenylalanine (black points), and L-Phenylalanine (red points), into a dispersion of c) L-m-carbon, and b) D-m-carbon.*

Integrating the individual heat flow peaks gives a more precise and quantitative overview over the heat of each injection (**Figure 4.7c** and **d**), and highlights the chiral nature of the materials even more obviously than raw ITC data. Interaction between L-m-carbon and D-Phenylalanine causes a heat of 7.7 kJ mol^{-1} per injection, in comparison to interaction with L-Phenylalanine with a maximum of 4.1 kJ mol^{-1} per injection (**Figure 4.7c**). On the other hand, injecting L-Phenylalanine into D-m-carbon dispersion reaches 5.1 kJ mol^{-1}, and injecting D-Phenylalanine yields less than 3.8 kJ mol^{-1} per injection (**Figure 4.7d**). From this we can express the enantiomeric ratio of L-m-carbon for Phenylalanine to be (D/L) = 1.88, and of D-m-carbon (L/D) = 1.34. The differences between the chiral carbon

adsorbents are more pronounced over the first injections because it can be assumed that the Phenylalanine molecules interact with the sites providing the strongest adsorption (and by that the most selective chiral recognition) at the lowest concentration. As the concentration of amino acid enantiomer in the solution increases, the contribution of non-specific interactions also increases and the differences in the heat flow become less pronounced.

The control experiments were conducted by titrating the amino acid solutions into pure water, or into dispersion of commercial activated carbon (AC) material (**Figure S 3**, Appendix). The released heat upon dilution (injection of Phenylalanine into water) reaches only 0.8 kJ mol^{-1} per injection, and when no specific interactions are taking place (injection of Phenylalanine into dispersion of AC) 4.7 kJ mol^{-1} per injection. Also when amino acid is titrated into solution of chiral ionic liquid (L-Tyr BF_4 and D-Tyr BF_4), no specific interactions were observed, with released heat in the range of heat of dilution (**Figure S 4**, Appendix).

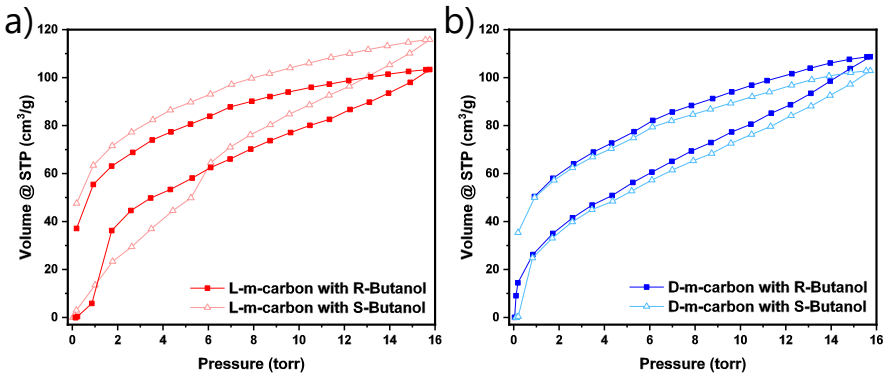

Figure 4.8. *Chiral vapor adsorption isotherms (at 25 °C) of a) L-m-carbon, and b) D-m-carbon with R-Butanol (solid squares) and S-Butanol (hollow triangles).*

Another technique employed to investigate the chiral recognition of the materials is the physisorption of chiral vapor. In comparison to ITC measurements, the advantage of this method is that there are only two phases involved into the adsorption process and interfering solvent effects can be ruled out. For these experiments, (R)-(−)-2-Butanol and (S)-(+)-2-Butanol were adsorbed on both enantiomers of carbon materials. Adsorption isotherms of L-m-carbon reveal a higher affinity of this material towards S-Butanol than R-

Butanol (**Figure 4.8a**). D-m-carbon shows the opposite behavior, with higher total uptake of R-Butanol than S-Butanol (**Figure 4.8b**), which confirms the results of ITC and shows that the chiral recognition of the materials is not limited to the enantioselective adsorption of species from solutions.

Carbons with enantioselective surface containing meso- and micropores have been successfully synthesized by nanocasting from chiral ionic liquid precursors. These carbonaceous materials have been exemplarily applied for chiral separation in gas and liquid phase. Although ILs present a good platform for carbon precursors, they are rather costly and usually have to be combined with a template to yield a porous carbon. To maximize the atomic efficiency of the IL precursors, and to ensure control over the porosity of the resulting carbon material, composite materials can be formed, combining two (or more) sets of properties in one material. This approach will be presented in the Chapter 4.2, by the formation of stable composites consisting of pristine porous carbon material, and a chiral carbon coating derived from CIL.

4.2. Porous All-Carbon-Based Nanocomposites with Enantioselective Surface

Because of the difficulties in chemical functionalization of the heterogeneous surface of porous carbon materials, it can be expected that the formation of homogeneous chiral coating is also challenging.[95, 126, 138] Pristine carbon that serves as a host material in the present study has a well-defined pore architecture and a stable backbone, although its surface atomic functions are rather hydrophobic and heterogeneous.[73] For this reason, the present Chapter includes a deposition of a C_2N-type polar mediator between a pristine carbon and a CIL-derived carbon coating. The coating ensures a homogeneous surface for interaction with CIL that is subsequently carbonized on a low temperature, to yield two composite materials with the opposite chiral surface. The chiral nature of prepared composites was investigated by the same techniques as in Chapter 4.1.

4.2.1. Synthesis and Characterization of Nanocomposites with Enantioselective Surface

Pristine carbon used as a support material was ordered mesoporous carbon (CMK-3, in further text denoted as C), obtained by impregnation of silica hard template (SBA-15) with sucrose, followed by its carbonization and template removal.[67, 73] For providing more homogeneous and polar surface chemistry, C was impregnated with hexaazatriphenylene-hexacarbonitrile (HAT-CN) (in blue rectangle in **Figure 4.9**), which was then heated to 550 °C under nitrogen flow.[229] The controlled condensation of this nitrogen-rich organic molecule yields a nitrogen-doped carbonaceous network with almost perfect C_2N-type stoichiometry.[107] The composite between nitrogen-doped carbon and a pristine carbon obtained in this way is labeled as C_2N/C composite. This material was subsequently coated with the N,N-dimethyl-L-Proline methyl ester bis(trifluoromethylsulfonyl)imide (L-Pro-TFSI) CIL (in orange rectangle in **Figure 4.9**), or its D-enantiomer (in green rectangle in **Figure 4.9**). L-Pro-TFSI and D-Pro-TFSI CILs were synthesized by a previously reported procedure.[124, 223] The final composite materials were obtained after the carbonization of the CIL-coating on C_2N/C composite on 500 °C in an inert atmosphere, labeled as "L-composite" and "D-composite".

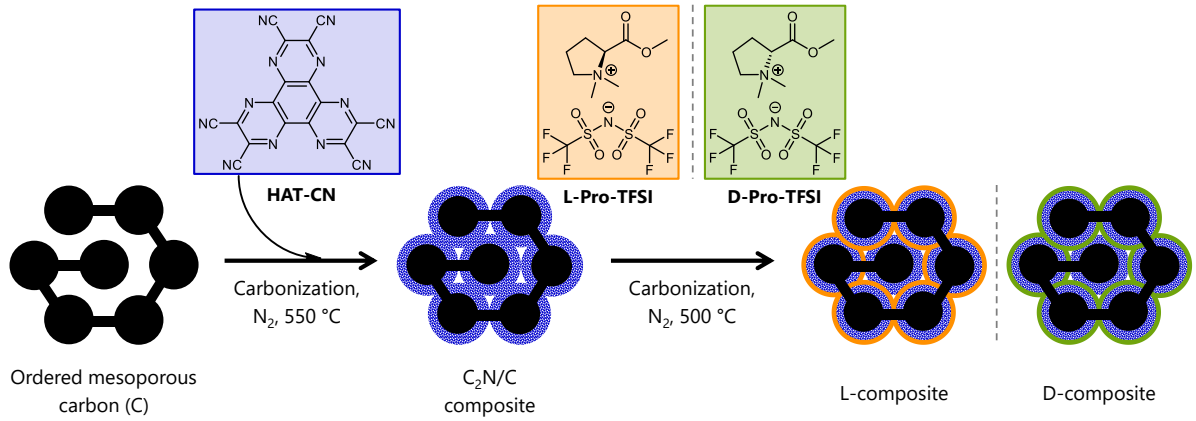

Figure 4.9. *Synthesis procedure of C_2N/C composite, and L- and D-composites.*

The pore structures of the prepared carbon, as well as the composite materials were investigated by N_2 physisorption experiments (–196 °C) (**Figure 4.10a–c**). C displays a type IV(a) isotherm according to IUPAC classification, with an H2(a) hysteresis loop in the

relative pressure range of 0.45 – 0.75, which is typical for ordered mesoporous adsorbents (**Figure 4.10a**). This material was chosen as a support material for the formation of composites due to its ordered structure with a large amount of well-interconnected mesopores. The hierarchical pore structure of C enables compete infiltration of HAT-CN precursor into the body of pristine carbon. Upon the formation of C_2N/C composite, a large number of pores of C carbon are occupied with C_2N material, which is leading to a substantial decrease in the porosity. C_2N-type material formed through a condensation of HAT-CN precursor is entirely microporous, and it is therefore expected that the resulting composite contains a considerable amount of micropores as well. C_2N/C composite, as well as L- and D-composite exhibit a combination of type I and type II isotherms, as typical for mainly microporous solids with a certain amount of external porosity, deduced from the nitrogen uptake above relative pressure of 0.95. All three composite materials show a minor hysteresis, originating from remaining mesopores of the C support material.

In the Chapter 2.3.1, the concept of sacrificial template ions in the carbonization of IL is described as an elegant approach for obtaining porous carbons without using external non-carbonizable template material. This has several advantages, among which the absence of inorganic impurities in the final material is the most essential one.[110, 116] In the present study, a large anion TFSI is utilized for the creation of pores in the CIL-derived coating. The carbonaceous materials derived from L- and D-Pro-TFSI are porous (**Figure S 5**, Appendix, CO_2 pore volume equals 0.25 $cm^3\ g^{-1}$), therefore it is not surprising that the nitrogen uptake of L- and D-composite is similar as in parent C_2N/C composite.

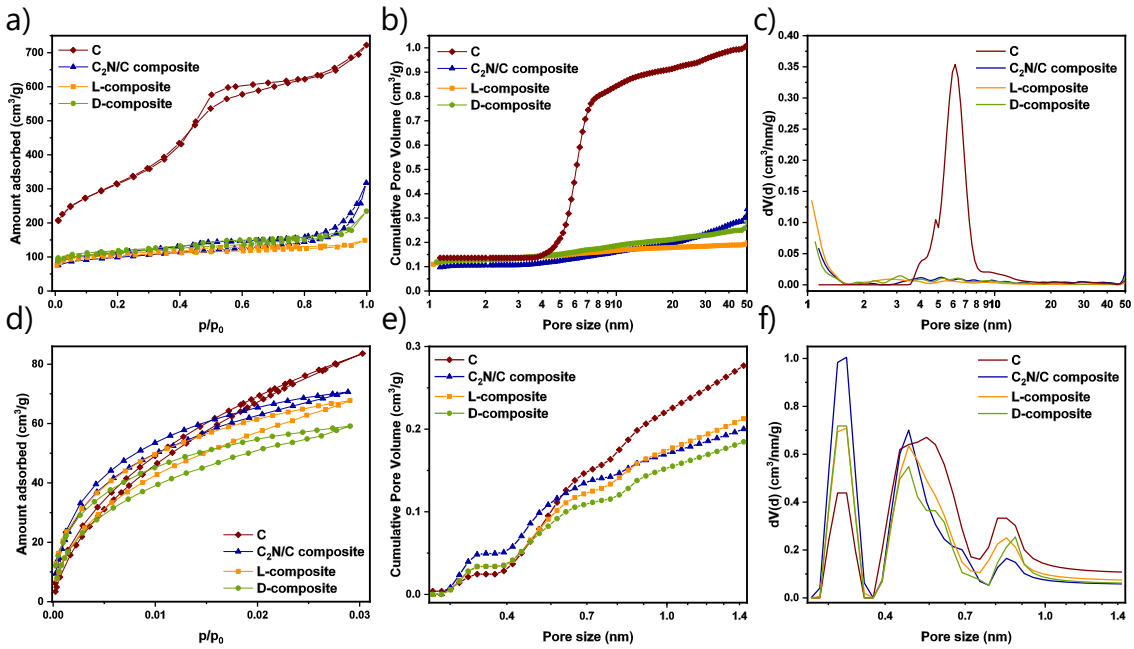

Figure 4.10. *a) N_2 physisorption isotherms (at –196 °C) with the corresponding b) cumulative and c) differential pore size distribution plots calculated with QSDFT, d) CO_2 physisorption isotherms (at 0 °C) with the corresponding e) cumulative and f) differential pore size distribution plots calculated with NLDFT of C, C_2N/C composite, L- and D-composite.*

Table 4.3. *SSA_{BET}, DFT mesopore volume (V_{Meso}), DFT micropore volume ($V_{N_2\ (<2\ nm)}$), obtained from N_2 physisorption measurements (at –196 °C), DFT pore volumes obtained from CO_2 physisorption measurements (0 °C)*

Sample	SSA_{BET} [$m^2\ g^{-1}$]	V_{Meso} [$cm^3\ g^{-1}$]	$V_{N_2\ (<2\ nm)}$ [$cm^3\ g^{-1}$]	$V_{CO_2\ (<1.5\ nm)}$ [$cm^3\ g^{-1}$]	$V_{CO_2\ (<0.7\ nm)}$ [$cm^3\ g^{-1}$]
C	1121.6	0.86	0.14	–	–
C_2N/C composite	355.8	0.22	0.10	0.20	0.14
L-composite	395.3	0.08	0.13	0.21	0.13
D-composite	418.5	0.14	0.13	0.18	0.11

For the analysis of narrow micropores, CO_2 physisorption (0 °C) experiments were carried out on all materials (**Figure 4.10d–f**). The convex shape of the isotherms of composite materials together with the presence of hysteresis reveal a high affinity to CO_2 at low relative pressure, due to the high content of nitrogen in the composites. The isotherm of C is rather linear, without the pronounced hysteresis. The porosity of composites for CO_2 is

comparable, as it is the case for N_2. The PSD of synthesized materials was further analyzed by the QSDFT (adsorption branch kernel) for N_2 adsorbed on carbon with slit/cylindrical/spherical pore shape, and nonlocal DFT analysis of CO_2 physisorption measurements (**Table 4.3**). C has a high mesopore volume of 0.86 $cm^3\ g^{-1}$, and a narrow PSD centered around a diameter of 6 nm. The volume of pores with a diameter below 1.5 nm, determined by CO_2 physisorption, is 0.21 and 0.18 $cm^3\ g^{-1}$, for L- and D-composite, respectively. The volume of ultramicropores (diameter < 0.7 nm) is significant for both composites, and equals 0.13 and 0.11 $cm^3\ g^{-1}$, for L- and D-composite, respectively. PSD of all composite materials indicates different diameters of micropores present in the materials (**Figure 4.10e** and **f**). L- and D-composite materials exhibit comparable SSA_{BET} of 395 and 418 $m^2\ g^{-1}$, respectively.

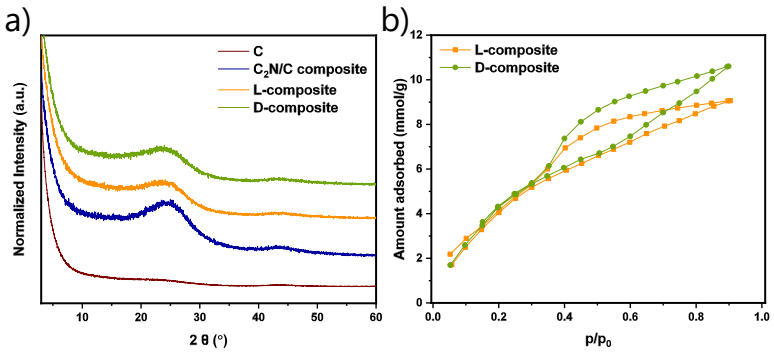

Figure 4.11. *a) XRD patterns of C, C_2N/C composite, L- and D-composite, and b) water vapor physisorption isotherms (25 °C) of L- and D-composites.*

Table 4.4. *Elemental analysis and energy dispersive X-ray spectroscopy data summary (in wt %), and I_D/I_G obtained from Raman spectra of C, C_2N/C composite, L- and D-composite.*

Sample	C		N		H_{EA}	S_{EA}	I_D/I_G
	EDX	EA	EDX	EA			
C	–	81.4	–	0.2	1.4	1.0	1.00
C_2N/C composite	–	65.7	–	18.0	1.6	0.3	1.02
L-composite	73.9	67.8	22.9	15.7	1.6	0.6	1.24
D-composite	77.1	67.9	19.7	16.4	1.5	0.2	1.23

*In addition to the elements in the table, the content of O_{EDX} in L-composite is 3.2 wt % and in D-composite it is 3.1 wt %.

XRD measurements of C and the composite materials show patterns that are typical for disordered porous carbon materials without crystalline inorganic impurities (**Figure 4.11a**). The composite materials reveal broad (002) and (101) carbon peaks at ≈ 25° and ≈ 44° 2θ, with (002) peak slightly shifted to lower angles in L- and D-composites. This can imply that that the carbonaceous layer obtained from CIL has a larger distance between graphitic layers. The absence of obvious carbon peaks and the high scattering at low angles in the C sample could be ascribed to its high porosity.

The results of EA illustrate the process of composite formation, through their bulk elemental composition values (**Table 4.4**, and **Figure S 6**, Appendix). From predominant carbon content and almost no nitrogen present in the C, the formation of C_2N/C composite results in decreased carbon content of 65.7 wt % while nitrogen content increases to 18.0 wt %. Upon deposition of CIL-derived carbon layer, the carbon content slightly increases, while nitrogen content decreases. L- and D-composites have almost identical chemical compositions, having 67.8 and 67.9 wt % C, and 15.7 and 16.4 wt % N in L- and D-composite, respectively. EDX presents slightly higher values for both elements and around 3 wt % of O, which is due to the same reasons as described in Chapter 4.1.1. Namely, large amount of non-detected contributions in EA are a consequence of adsorption of moisture and species from the atmosphere in the pores of these polar materials.

Water vapor adsorption (25 °C) was used as a probe for surface chemistry and pore structure characterization of the L- and D-composites (**Figure 4.11b**). Due to the high content of heteroatoms in these materials, the onset point of water adsorption is already at low relative pressures. Below p/p_0 of 0.4, specific interactions between water and nitrogen functionalities are responsible for a steep increase in the water uptake. The materials have identical shape of the isotherms below p/p_0 of 0.6, where surface-water interactions are dominant. Based on this, it can be concluded that the surface polarity of L- and D-composite is also very comparable. The minor difference above this pressure with a slightly higher total uptake for the D-composite is due to the adsorption in the wider micropores and narrow mesopores, and it is following the behavior observed in N_2 physisorption.

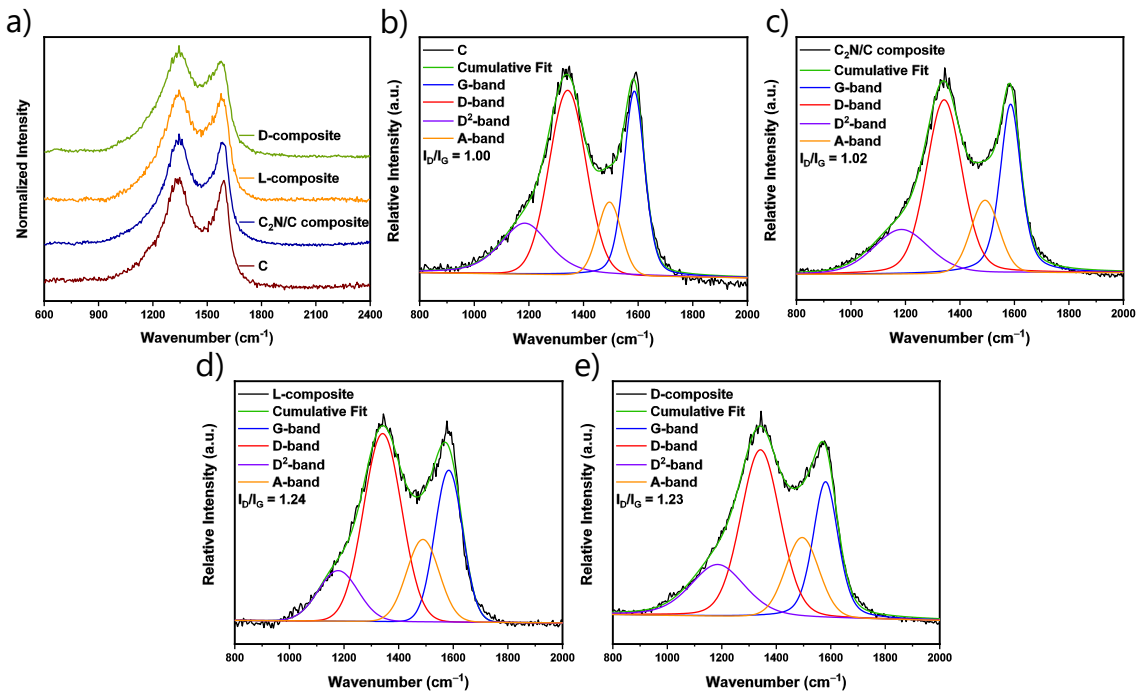

Figure 4.12. *a) Normalized Raman spectra, and deconvoluted Raman spectra of b) C, c) C_2N/C composite, d) L-composite, and e) D-composite.*

Raman spectra of the prepared materials were fitted by using a 4-band model with mixed Gaussian/Lorentzian peaks (**Figure 4.12**).[230] C carbon exhibits a spectrum as it is typical for disordered carbon materials, with the D-band at ~1340 cm^{-1} and the G-band at ~1595 cm^{-1}. The D-band (disordered) originates from the breathing mode of sp^2-hybridized carbon atoms in aromatic rings neighbored by a defect. The G-band (graphite-like) originates from vibrations of all sp^2 carbons organized in chains or rings. The origin of A-band and D^2-band is less understood, but the A-band is often related with the amorphous component of sp^2 carbon materials, as well as with five- and seven-membered rings. The D^2-band can be correlated with trans-polyacetylene-like chains at layer edges. The peak intensity ratio of D- and G-band (I_D/I_G) is a useful parameter for determining the degree of carbon ordering in porous carbon materials.[231-232] For the composite materials, the standard interpretation of Raman spectra for porous carbons cannot be directly implemented, because nitrogen doping causes vibrational dissymmetry. However, certain conclusions about their structure can indeed be made through a comparison with their non-doped support material. The values of I_D/I_G for C and C_2N/C composite are almost identical (1.00 and 1.02 cm^{-1}, respectively), which indicates a comparably high degree of

aromatization, and that the Raman signal of C remains almost unaffected by coating (**Table 4.4**). This is probably due to a high level of ordering during the controlled condensation of HAT-CN into the C_2N material. L- and D-composites have almost identical values of I_D/I_G, 1.24 and 1.23 cm^{-1}, respectively, suggesting a more disordered structure than their support materials. Furthermore, this is also supported by the higher contribution of A-band in the composite materials, in comparison to the C and C_2N/C composite. This can be ascribed to the low-temperature carbonization of CIL coating, which does not undergo a controlled carbonization pathway like C_2N material and results in a disordered structure.

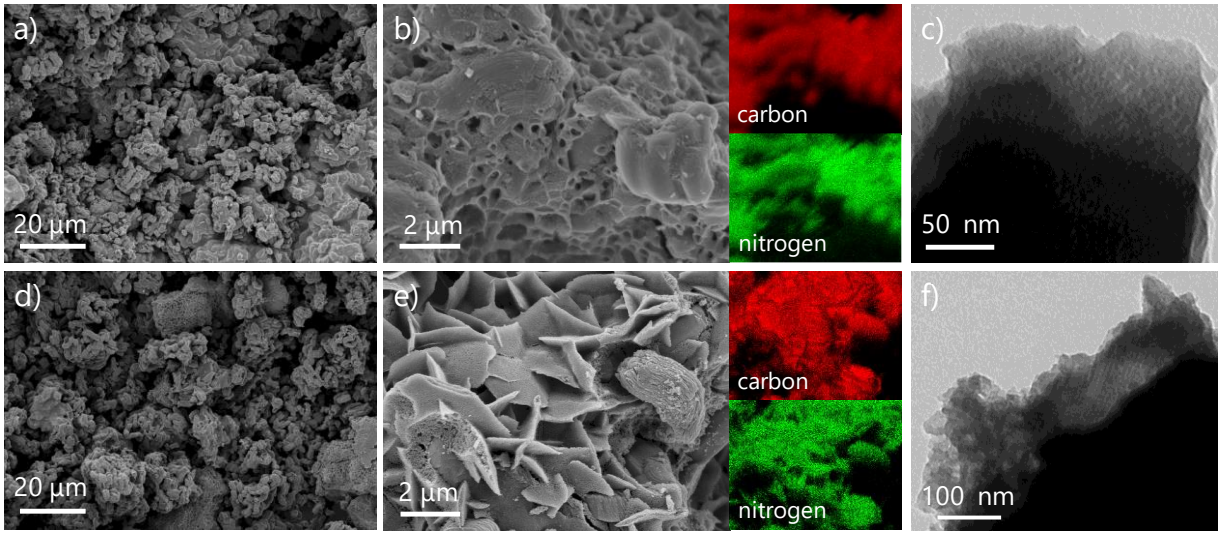

Figure 4.13. *SEM images with elemental mapping of a–b) L-composite, d–e) D-composite, and TEM images of c) L-composite, and f) D-composite.*

SEM shows very similar morphologies between L- and D-composites (**Figure 4.13**). The images exhibit hexagonally arranged cylindrical shapes originating from ordered mesoporous C support material. In most cases, these structures have a coating made of a material with a smooth surface, which can be assigned to C_2N material, since it is known that it exhibits this kind of morphology.[107] However, although the C_2N material is visible in the micrographs, the infiltration of C can be confirmed by disappearance of hysteresis in the composite material. Additional features observed in both analyzed composites are sponge- and shell-like structures, arising from carbonized CIL and C_2N material. EDX spectroscopy mapping patterns display a homogeneous distribution of carbon and nitrogen in L- and D-composites (**Figure 4.13b** and **e**). This indicates that the carbonized

CILs are evenly distributed on the surface of C_2N/C composite, probably due to its homogeneous surface that readily interacts with ionic liquid. TEM images of L- and D-composite also demonstrate the ordered mesoporous system of the C host, together with typical microporous amorphous carbon morphology (**Figure 4.13c** and **f**). The C_2N/C composite shows similar microporous morphology (**Figure S 7**, Appendix).

4.2.2. Interaction between Nanocomposites with Enantioselective Surface and Chiral Species

Structural and chemical characterization of L- and D-composites reveal their almost identical structure, including porosity, morphology, surface and bulk chemistry. They are, however, synthesized from the enantiopure ionic liquids, and it can be expected that they interact differently with the enantiomers of the same compound if the chiral information of the CIL could be transferred to the composites. For further investigation of this hypothesis, ITC was employed. In the experiments, equal aliquots of one enantiomer of Phenylalanine (Phe) were titrated into the dispersion of L- or D-composite, and the heat response upon injection is monitored.

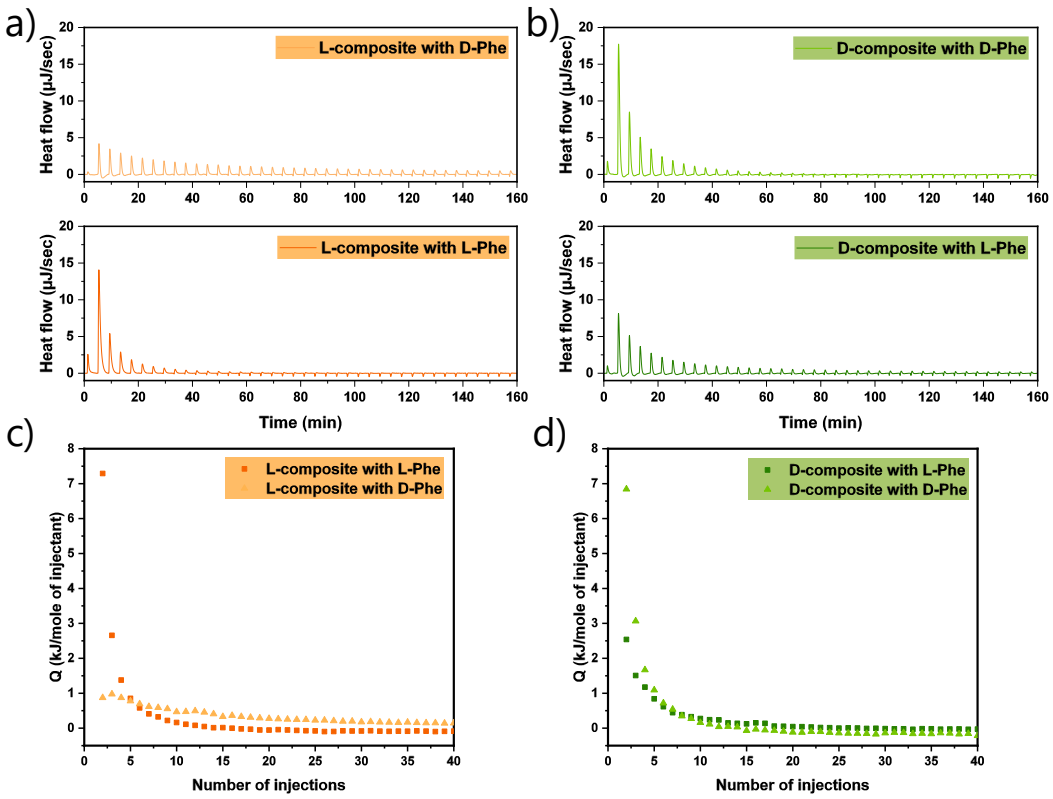

Figure 4.14. *a) and b) Raw isothermal titration calorimetry data from injecting D-Phenylalanine (upper panel), and L-Phenylalanine (lower panel), into a dispersion of a) L-composite, and b) D-composite. Heat per mole of injected L-Phenylalanine (square points), and D-Phenylalanine (triangle points), into a dispersion of c) L-composite, and b) D-composite.*

The absorbed heat upon the addition of L-Phe in the dispersion of the L-composite is higher than the heat upon the addition of D-Phe in the same material (**Figure 4.14a**). At the beginning of the titration, the pores of the composite are filled with water, and the first molecules of the titrant are therefore inducing the highest heat response. First injections are responsible for specific interactions between the porous composite with the chiral surface, and a chiral molecule. The first injection of L-Phe into the dispersion of the L-composite is causing 8.4 times more heat flow than the interaction with D-Phe, reaching 7.3 kJ per mole of the amino acid (**Figure 4.14c**). Upon further addition of L-Phe, this difference substantially decreases, yielding 2.8 and 1.6 times more heat in the second and third injection, respectively, in comparison to titration with D-Phe. As the solution becomes saturated with amino acid, the non-specific interactions increase, and therefore not only the heat responses of both samples but also their relative difference decreases. Due to the

complex processes happening throughout the titration, including desolvation, dilution, desorption of solvent from the pores, and adsorption of a chiral molecule on the surface of a material, and due to the very hydrophilic properties of the C_2N coating, it is difficult to precisely determine the single contributions of each factor, especially after the first couple of injections. The interactions upon titration of D-composite reveal the opposite trend than for L-composite, with higher heat flow upon injection with D-Phe, than with L-Phe (**Figure 4.14b**). This corresponds to 2.7, 2.0, and 1.4 times more heat absorbed after first, second, and third injection with D-Phe in comparison to L-Phe (**Figure 4.14d**). Similarly to L-composite, these differences become less pronounced when the concentration of amino acid in the solution increases. Based on this, the enantiomeric ratio of L-composite for Phenylalanine is (L/D) = 8.4, and of D-composite is (D/L) = 2.7.

However, the adsorption capacity of these composites is relatively limited due to their narrow micropores, which are partially also filled with the solvent molecules. To decouple it from the influence of the solvent, chiral recognition of the composites was also investigated by the physisorption of chiral vapor. The probe adsorbates used in these experiments are the same as in the Chapter 4.1.2 – enantiomerically pure forms of 2-Butanol, namely (R)-(−)-2-Butanol and (S)-(+)-2-Butanol. The enantiomers of the vapor were adsorbed on the activated (outgassed) composites at 25 °C.

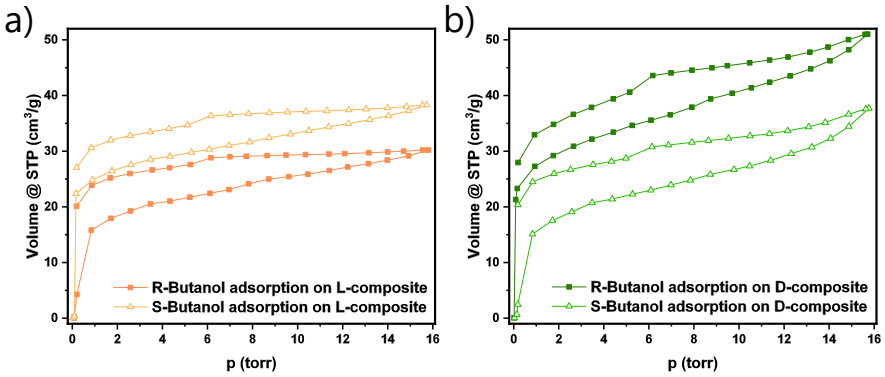

Figure 4.15. *Chiral vapor adsorption isotherms (25 °C) of a) L-composite, and b) D-composite with R-Butanol (solid squares) and S-Butanol (hollow triangles).*

Adsorption of S-Butanol on the L-composite has considerably higher vapor uptake than adsorption of R-Butanol, throughout the entire range of applied pressures (**Figure 4.15a**).

The trend is opposite for adsorption on D-composite (**Figure 4.15b**). Similarly as in ITC, it is expected that the specific chiral interactions between the composite material and the adsorbate take place predominantly in the low-pressure region when the chiral centers in the material are still accessible and adsorbent-adsorbate interactions are dominant. N_2 and CO_2 physisorption measurements have shown that the (ultra)micropore structures of L- and D-composite are almost identical (**Figure 4.10**). Moreover, their interaction with water vapor in the low relative pressure region is also the same (**Figure 4.11b**). Thus, it is not surprising that the shape of Butanol adsorption isotherms in the low-pressure region is comparable for both materials and both enantiomers of Butanol. However, different uptakes of enantiomers of Butanol can be assigned to chiral recognition taking place between the vapor and the pore walls of the composite. For instance, at 1.7 torr (corresponds to a relative pressure of 0.09), L-composite adsorbed 17.9 $cm^3\ g^{-1}$ of R-Butanol, and 26.4 $cm^3\ g^{-1}$ of S-Butanol, whereas D-composite adsorbed 29.2 $cm^3\ g^{-1}$ of R-Butanol, and 17.5 $cm^3\ g^{-1}$ of S-Butanol. In the higher pressure region, and close to the saturation pressure of Butanol, the shape of the isotherms is similar to N_2 and water vapor isotherms, with a distinct rise in the uptake of the adsorbate on the D-composite. Considering that in this range it comes to multilayer adsorption, it can be assumed that chiral recognition does no longer have a significant influence on the resulting vapor uptake and the slope of the isotherms remains comparable for both composites. The enantiomeric ratio expressed on 1.7 torr of L-composite for Butanol is (S/R) = 1.5, and of D-composite is (R/S) = 1.7. If the enantiomeric ratio is expressed at the highest uptake of Butanol, it equals (S/R) = 1.3 for L-composite, and (R/S) = 1.3 for D-composite.

Chapter 4 provided an insight into a promising novel application of porous carbons that has not been extensively studied so far. It has been exemplarily shown that porous heteroatom-doped carbons synthesized from chiral ionic liquid precursors can indeed express specific interactions with enantiopure compounds from the solution and the gas phase. The hard template has successfully been employed in Chapter 4.1 to deliver a well-connected porous system into the carbon materials while providing spatial confinement for the precursors. In addition, the resulting materials were free from inorganic impurities that are usually present in the heteroatom-doped carbons templated by salt. A different

template-free approach that offers better economic utilization of chiral precursors and separates the creation of pores from the creation of chiral carbon has been described in Chapter 4.2. The creation of nanocomposites between the pristine carbon and heteroatom-doped carbon that contains chiral information has been presented as a viable solution for establishing carbonaceous materials with an enantioselective surface.

5. Control of Catalytic Activity in Liquid-Phase Oxidation of D-Glucose by the Local Environment of a Catalyst[3]

Chirality-related applications may present some of the future applications of porous carbon materials, especially in separation sciences, as sensors, or in asymmetric catalysis. However, this field is still rather unexplored and exotic, and the most notable discoveries will follow. On the other hand, the applications of carbons that are well established encompass, among others, traditional chemocatalysis. They are predominantly used as porous supports for metals that serve as the active phase, in the form of single atoms, clusters or nanoparticles (NPs). Expectedly, numerous studies exist about the electronic or geometric effects that carbons have on the active phase and utilization of these impacts for the regulation of catalytic activity. However, these porous materials are also expected to influence the liquid reaction medium, and this phenomenon is by far less explored. Considering that the local environment of the catalytically active phase (i.e., the coverage of the metal by reactants) can drastically influence the kinetics of the reaction, this can indeed be used as a regulation screw in catalysis. In the following Chapter 5, different approaches for increasing the local concentration of reactants and by that the catalytic activity will be presented.

In Chapter 2.4.2, it was presented that NPs supported on porous support are a part of one complex system that is mutually connected and interrelated. In this sense, the support material can influence the catalytic activity of the NPs by changing the NP morphology, charge transfer, changing the chemical composition of a NP, or even by direct participation in catalysis, which is often the case for oxide supports.[33, 189, 234] On the other hand, even when the support is considered inert, like porous pristine carbons, it can affect the surrounding fluid phase of the catalyst.

[3] The results of this chapter are adapted with permission from the original work of the author:
[1] Perovic, M., Tarakina, N.V., Hofmann, J.P., and Oschatz, M.: Influence of Local Environments in Pores of Different Size on the Catalytic Liquid-Phase Oxidation of D-Glucose by Au Nanoparticles Supported on Nanoporous Carbon. *ACS Applied Nano Materials* 2020, *3*, 8, 7695 – 7703. (Ref.[233])
[2] Perovic, M., Zeininger, L., and Oschatz, M.: Immobilization of Gold-on-Carbon Catalysts onto Perfluorocarbon Emulsion Droplets to Promote Oxygen Delivery in Aqueous Phase D-Glucose Oxidation. *ChemCatChem* 2020, DOI: 10.1002/cctc.202001590. (Ref.[283])

In this sense, pores represent a unique environment that influences not only the properties of a material, but also the chemical species inside the pores. For similar reasons that NPs of even the most inert metals like gold exhibit catalytic activity, the properties of confined phase differ to those of bulk. In narrow pores, the "break-down" of thermodynamics occurs, hence the Gibbs phase rules no longer describe the system appropriately, and these effects together are called confinement effects.[191, 235-236] For example, many characteristic properties of water, such as maximum density at 4 °C, large heat capacity, and others, are a consequence of its molecular structure and the ability to form an extended network of hydrogen bonds. However, these properties of bulk water differ significantly when water is confined within cavities, leading to a shift in temperature of liquid–solid transition, critical point, or even introduction of novel phase transitions.[237-241] Moreover, in response to capillary pressure and changed molecular orientations, the solubility of gases in a confined water increases, especially when the bulk is liquid.[242-245] In the context of heterogeneous catalysis with porous supports, the confinement effect can be a powerful internal regulation screw for increasing catalytic activity. Especially when one reactant in a liquid phase reaction is a gas and its dissolution in the liquid medium represents a crucial contribution for the overall kinetics of a reaction. Since the surface coverage of the NPs with reactants is determining their activity, the solubility of the gas and the accessibility of the solvent and reactants to the active phase play an important role in heterogeneous catalysis. From this perspective, NPs of similar size should show different catalytic properties when confined in or surrounded by pores of different sizes provided by support material. A proof of concept to this theory is reported in Chapter 5.1 by using a model system of D-glucose oxidation to gluconic acid in water with molecular oxygen, catalyzed by AuNPs supported on carbon materials of different porosity.

Contrary to a highly structured network of hydrogen-bonded bulk water, less cohesive liquids have a higher gas uptake. One class of compounds with remarkably weak intermolecular forces and low polarity are perfluorocarbons (PFCs). The solubility of oxygen in PFCs is up to one order of magnitude higher than in water, making them an attractive oxygen carrier.[246-253] Along with their exceptional property of dissolving gases, they are also omniphobic and thus immiscible with water. To increase the interfacial area

of PFCs in water, it is beneficial to create dispersed droplets – emulsions, which are commonly stabilized by various surfactants or with solid particles. Pickering emulsions are emulsions in which oil or water can be dispersed into the other phase in the form of micrometer-sized droplets that are stabilized by solid particles instead of molecular amphiphiles.[254-258] To further promote the catalytic activity of the most active catalyst from the Chapter 5.1, the following Chapter 5.2 presents the strategy for increasing the local concentration of oxygen in the proximity to the active phase by a formation of PFC emulsions stabilized by solid particles of a catalyst.

5.1. Influencing the Local Environments by Pores of Different Size

In liquid-phase catalysis, porous catalyst supports can induce nanoconfinement of solvent and the solute molecules within the porous network. This can influence their local concentration and structure around the catalyst, and thus the surface coverage of the active phase of the catalyst. Such nanoconfinement effects are of particular importance in reactions carried out in liquid-phase where one reactant is a gas.[242-244, 259] The significant influence of the pore structure of carbon materials on the catalytic activity of gold nanoparticles (AuNPs) with nearly similar size is demonstrated in the following Chapter. The results on the oxidation of D-glucose with molecular oxygen in aqueous solution show that the "apparent catalytic activity" of AuNPs is a function of the carbon pore size and geometry. This is presented on a series of AuNP catalysts supported on salt-templated carbons (STCs), as well as on ordered mesoporous carbon material (CMK-3).

5.1.1. Synthesis and Characterization of Au Nanoparticles Supported on Nanoporous Carbon Catalysts

Salt-templated carbons (STCs) have been used as model supports because their porous structure can be controlled and easily tuned by varying the ratio between the carbon precursor and the salt template.[84, 87] $ZnCl_2$ and sucrose have been used as a porogen, and as carbon precursor, respectively. After the carbonization of the carbohydrate-salt mixture, the template removal was accomplished by thorough washing with HCl solution. The carbon materials obtained in this way contain micro- and mesopores, and they are labeled

as STC-X, where X stands for mass ratio of $ZnCl_2$ to sucrose. The ordered mesoporous carbon material (CMK-3) investigated in this study has been obtained as previously described (**Figure 5.1**).[62, 67, 73]

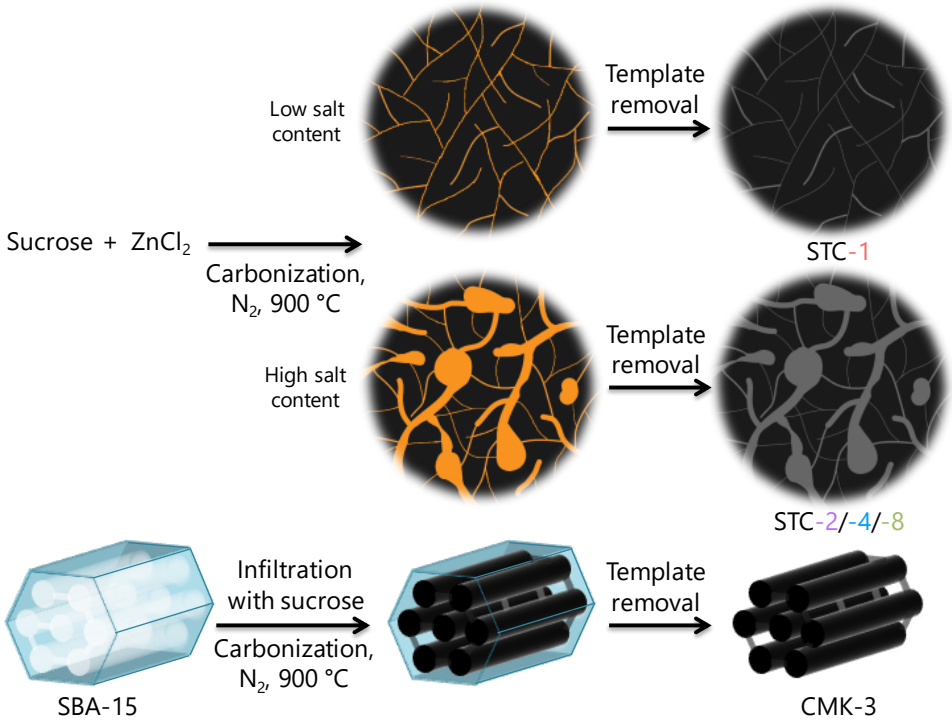

Figure 5.1. *Synthesis procedure of STC and CMK-3 carbon supports.*

N_2 physisorption experiments (–196 °C) were carried out to investigate the pore structures of the prepared carbons (**Figure 5.2a** and **Table 5.1**). STC-1 has a type I(a) isotherm according to the IUPAC classification, typical for solids with mainly narrow micropores. STC-2 exhibits a type I(b) isotherm with a narrow hysteresis loop, indicating a presence of small amount of mesopores in addition to the micropores. The type IV(a) isotherms of STC-4 and STC-8, together with their H4 type hysteresis loops in the relative pressure range between 0.5 and 0.9 indicate larger disordered mesopores in these materials. CMK-3 also reveals a type IV(a) isotherm but with a type H2(a) hysteresis loop in the p/p_0 range of 0.4 – 0.7, demonstrating its ordered mesoporous nature. The PSD of synthesized carbon materials was analyzed using QSDFT (adsorption branch kernel) for N_2 adsorbed on carbon with slit/cylindrical/spherical pore shape (**Figure 5.2b** and **c**). STCs have comparable micropore volumes in the range of 0.25 to 0.45 $cm^3\ g^{-1}$, whereas CMK-3 shows a much lower micropore volume of 0.09 $cm^3\ g^{-1}$ (**Table 5.1**). The mesopore volume

gradually increases with increasing salt template content in the series from STC-1 to STC-8, from 0.11 $cm^3\ g^{-1}$ for STC-1 to 1.75 $cm^3\ g^{-1}$ for STC-8. The volume of ordered mesopores of CMK-3 is 1.00 $cm^3\ g^{-1}$, and this material has a narrow pore size distribution centered around a diameter of 6 nm. On the other hand, all of the mesoporous STCs show an N_2 uptake over a wider range of relative pressures due to their rather broad pore size distribution. All of the materials provide high SSA_{BET} in the range of ~1200 – 2500 $m^2\ g^{-1}$. SSA_{BET} is gradually increasing in the range from STC-1 to STC-8 and CMK-3 has a SSA_{BET} that is comparable to STC-1.

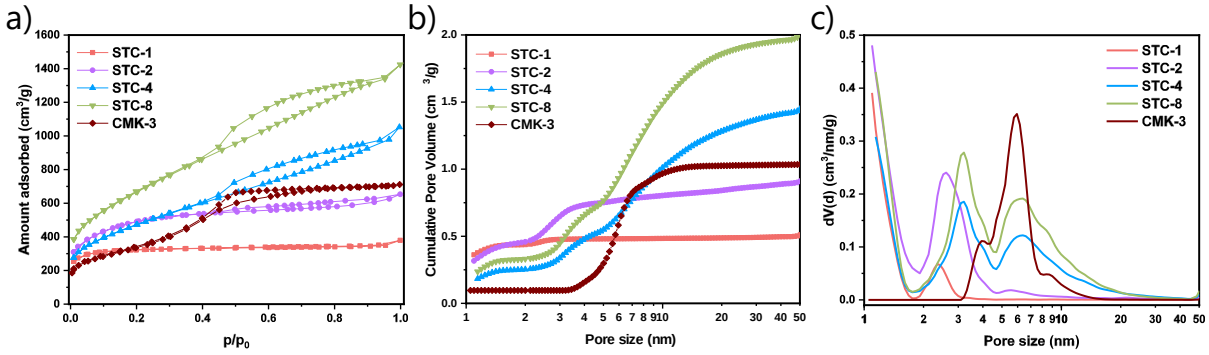

Figure 5.2. *a) N_2 physisorption isotherms (at –196 °C) with the corresponding b) cumulative and c) differential pore size distribution plots calculated with QSDFT (N_2 on carbons with slit/cylindrical/spherical pores at 77 K, adsorption branch kernel) of STCs and CMK-3.*

Table 5.1. *Specific surface areas (SSA_{BET}) calculated using the BET equation, total pore volume (V_t), DFT micropore volume (V_{micro}), DFT mesopore volume (V_{meso}), obtained from N_2 physisorption isotherms (at –196 °C), and I_D/I_G ratio, and FWHM of the D-band of STCs and CMK-3 obtained by Raman spectroscopy.*

Sample	SSA_{BET} [$m^2\ g^{-1}$]	V_t [$cm^3\ g^{-1}$]	V_{Micro} [$cm^3\ g^{-1}$]	V_{Meso} [$cm^3\ g^{-1}$]	I_D/I_G	FWHM of the D-band [cm^{-1}]
STC-1	1210.2	0.59	0.43	0.11	1.8	213
STC-2	1748.5	1.01	0.45	0.52	1.1	153
STC-4	1711.3	1.63	0.25	1.27	1.1	159
STC-8	2429.4	2.21	0.33	1.75	1.3	155
CMK-3	1208.0	1.10	0.09	1.00	1.0	171

TGA of the carbon materials under synthetic air show small ash-content (less than 3 wt %) above 600 °C for STCs, and no remaining mass above 500 °C for CMK-3 (**Figure S 8**,

Appendix). From this, it can be concluded that there are no significant amounts of inorganic residuals in the carbons, and thus the removal of Zn species and SiO_2 template from the STCs and CMK-3, respectively, was successfully accomplished.

Raman spectra of the carbon supports were fitted by a 4-band model, similarly to the previously described fitting procedure in Chapter 4.2.1. All of the carbons, independent of the templating method, show typical spectra of the disordered carbon nanomaterials, with the D-band at ~1340 cm^{-1} and the G-band at ~1595 cm^{-1} (**Figure S 9**, Appendix). Full-width of the half-maximum (FWHM) of the D-band for all carbon supports is relatively wide, indicating a large number of structurally disordered units within these materials. With the exception of STC-1, which has a slightly more disordered structure dominated by narrow pores, the values of I_D/I_G and the FWHM of the D-band for all STCs and CMK-3 are in the same range (**Table 5.1**). This implies that the support materials have a comparable degree of aromatization and no distinct differences that could affect their interaction with supported NPs.

A series of catalysts was synthesized by depositing a nominal loading of 1 wt % of AuNPs on the carbon supports (denoted as Au-STC-X, and Au-CMK-3). Colloidal gold dispersion was synthesized by a modified Turkevich method, with a sodium citrate stabilizer.[260] XRD measurements of the catalysts show typical amorphous carbon patterns, together with four peaks corresponding to Bragg reflections of the (111), (200), (220), and (311) planes of the face-centered cubic lattice of gold (**Figure 5.3**). The broad peaks of gold indicate that it is indeed deposited on the carbons as nanoparticles. The low intensity of Au reflections in Au-STC-8 could be ascribed to the high background noise of highly porous carbon support STC-8.

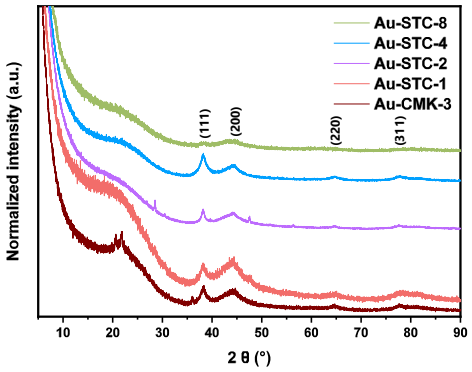

Figure 5.3. *XRD patterns of Au-STCs and Au-CMK-3 catalysts.*

TEM images reveal that in the series of Au-STCs, the morphology of the carbon support changes from a rather dense structure for the microporous Au-STC-1 to a gradually more porous appearance in the series from Au-STC-2 to Au-STC-8 (**Figure 5.4**). TEM of Au-CMK-3 reveals its mesoporous system with ordered carbon nanorods, a type of morphology that was observed already in previous chapters. Despite the different porosities of the support materials, the deposition of AuNPs resulted in comparable particle size distributions (**Figure 5.4f**). The average AuNP sizes in the studied catalysts determined by high-resolution TEM (HRTEM) span over a narrow range, from 4.1 nm for Au-CMK-3 to 4.7 nm for Au-STC-1 (**Table 5.2**).

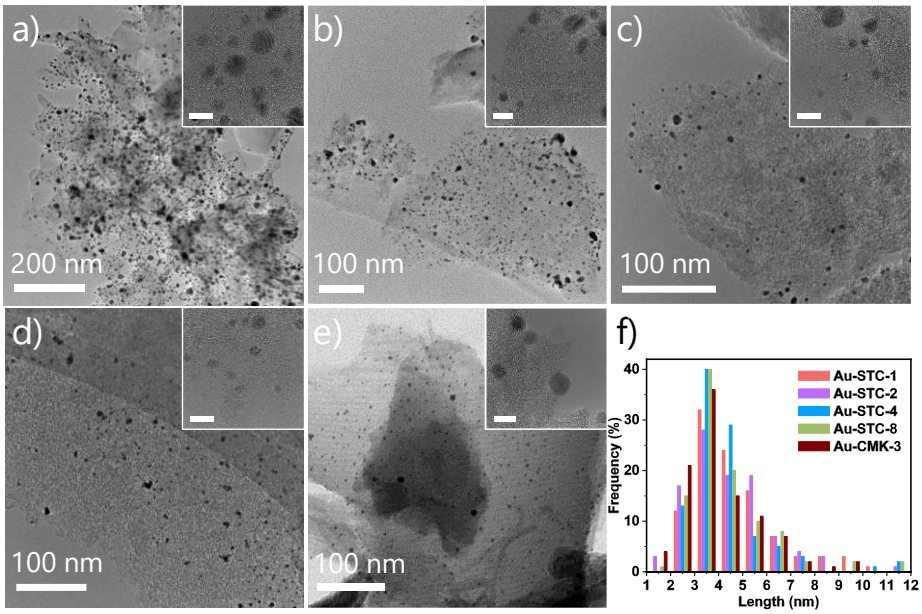

Figure 5.4. *TEM images of catalysts: a) Au-STC-1, b) Au-STC-2, c) Au-STC-4, d) Au-STC-8, e) Au-CMK-3, and f) corresponding AuNP size distributions. Insets show HRTEM images of the catalysts, the length of the scale bar is 10 nm.*

The deposition of stabilized AuNPs from dispersion to the carbon surfaces can be compared with a ligand-exchange mechanism.[261] Citrate stabilizer is thereupon replaced by surface oxygen groups present on the carbon or by the π-electrons of the supports, resulting in the formation of donor-acceptor couples. TEM images show that particles are mainly inhomogeneously deposited on the external surface of all carbon supports. One has to notice that before the TEM investigations the particles were washed/centrifuged and then sonicated for electron microscopy sample preparation. It is likely that the AuNPs cannot easily enter the bulk of large carbon support particles, because the pore sizes of the supports (**Figure 5.2b** and **c**) and the AuNPs sizes are in the same range. Furthermore, the ligand exchange from citrate to the surface of porous carbon occurs rapidly and the speed of migration of the AuNPs into the narrow pores of the support materials is further limited by the presence of stabilizer and solvation shell. Recently it has been shown that the surface chemistry of carbon supports, or in other words the strength of the carbon as a ligand for the AuNPs, plays a crucial role in the degree of agglomeration of the AuNPs during deposition.[262] Moreover, even when the metal NP size is in a comparable range, the surface chemistry of carbon supports can have a decisive role in the catalytic activity of deposited NPs.[33, 263-264] To minimize this influence, the surface chemistry of all carbon

supports under investigation has been adjusted by thermal treatment under reducing atmosphere, the aim of which is to provide similar strength of interactions of the AuNPs the supports during deposition. The rather hydrophobic surface atomic structure of carbonaceous support materials leads to a slower ligand exchange between the citrate stabilizer and the carbon support. This results in less agglomeration and coalescence, and therefore better stabilization of smaller AuNPs.

X-ray photoelectron spectroscopy (XPS) was employed to characterize the oxidation state and surface amount of elements present in the catalysts. The survey XPS spectra of Au-STCs and the Au-CMK-3 catalysts reveal the presence of C, O, and Au (**Figure 5.5a**). The high-resolution Au 4f spectra display the main Au $4f_{7/2}$ peak at 84.0-84.2 eV with a spin-orbit splitting of 3.67 eV, which corresponds to metallic Au species (**Figure 5.5b–f**, and **Table S 1**, Appendix). The additional smaller doublet located at 86.0-86.2 eV can be discussed as $Au^{\delta+}$ or Au^{+}.[210, 265-266] However, the content of this contribution is less than 5% of the Au peak in all catalysts, thus pinpointing the oxidation state of such minor species is difficult. The content of gold determined by XPS on the surfaces of the catalyst is between 0.3 and 1.4 at.% (**Table 5.2**). These values are significantly higher than the bulk Au content determined by inductively coupled plasma – optical emission spectrometry (ICP-OES) (**Table 5.2**), which is an indication that the AuNPs are mainly located on the external surface of the carbon supports.

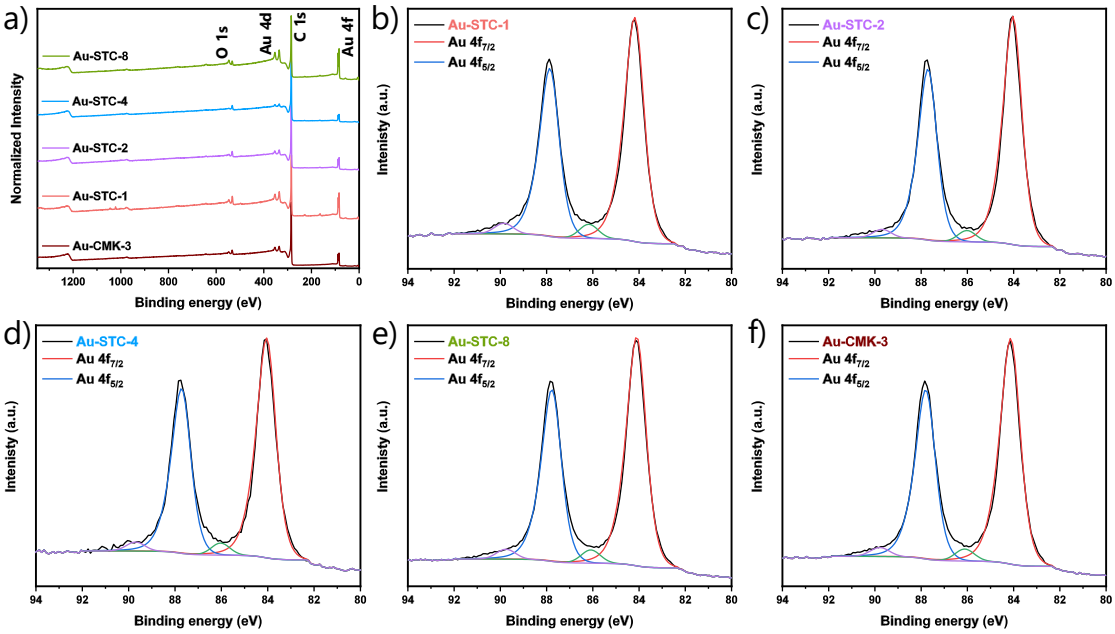

Figure 5.5. *a) XPS survey scans of the catalysts, and Au 4f XPS spectra with fitted components of b) Au-STC-1, c) Au-STC-2, d) Au-STC-4, e) Au-STC-8, and f) Au-CMK-3.*

Table 5.2. *XPS*, ICP-OES results, average AuNP sizes before and after (values in brackets) the D-glucose oxidation reaction, determined by TEM, and catalytic activity (metal time yield) for the D-glucose oxidation reaction.*

Sample	C $[at.\%]_{XPS}$	O $[at.\%]_{XPS}$	Au $[at.\%]_{XPS}$	Au $[wt\%]_{ICP}$	Average AuNP size $[nm]_{TEM}$	Catalytic activity $[mol_{Glc}\ min^{-1}\ mol_{Au}^{-1}]$
Au-STC-1	91	5.4	1.2	0.8	4.7 ± 1.7 (4.0 ± 1.5)	0
Au-STC-2	95	3.7	0.6	1.0	4.5 ± 1.7 (4.5 ± 1.9)	3.9
Au-STC-4	96	2.8	0.4	1.0	4.4 ± 1.6 (4.4 ± 1.8)	12.9
Au-STC-8	95	2.4	1.4	0.9	4.4 ± 1.7 (3.7 ± 1.4)	30.2
Au-CMK-3	96	2.9	0.7	1.0	4.1 ± 1.6 (4.0 ± 1.6)	60.6

*In addition to the elements in the table, XPS showed the presence of S in following samples: Au-STC-1 (2.4 at.%), Au-STC-2 (0.5 at.%), Au-STC-4 (0.4 at.%), Au-STC-8 (0.9 at.%), as well as the presence of Zn in Au-STC-1 (0.2 at.%).

C 1s (**Figure S 10**, Appendix) and O 1s spectra (**Figure S 11**, Appendix) show comparable shapes and relative contents for the entire series of the catalysts as well. The content of carbon (expressed through the integrated C 1s peaks) ranges between 90.8 and 96.4 at.%, and the oxygen content (expressed through O 1s peaks) is between 2.4 and 5.4 at.% (**Table 5.2**).There is no obvious correlation between the oxygen contents and the catalytic activity of the carbon supports discussed below (**Figure S 12**, Appendix). Together with C, O, and Au, STC-supported catalysts contain a small amount of S (0.4–2.4 at.%), which is due to the usage of sulfuric acid in the synthesis. It is expected that S is stable in the carbons, since this species resisted the carbonization under an inert atmosphere, as well as treatment in the reducing atmosphere. In addition, 0.2 at.% of Zn is found in Au-STC-1, which originates from the use of $ZnCl_2$ as a salt template.

After the comprehensive characterization of the carbon supports and the gold catalysts, it can be concluded that the surface chemistry of all of the samples is comparable. The XPS analysis has shown that the content and oxidation state of Au in the catalysts is in the same range, and the average AuNPs sizes determined from HRTEM are in the same range in all Au-STCs and Au-CMK-3 catalysts. Thus, it can be concluded that the performance of these catalysts will be mainly affected by the pore structures of the carbonaceous supports. One would not expect a significant difference in the catalytic activity of these materials in a liquid phase oxidation reaction with molecular oxygen as it is generally accepted that the size of AuNPs and the chemical properties of the support material are the factors with crucial influence.

5.1.2. Activity of the Au Nanoparticles Supported on Nanoporous Carbon Catalysts in Liquid-Phase D-Glucose Oxidation

Catalytic activities of the catalysts were tested on the oxidation of D-glucose with molecular oxygen in aqueous solution at pH = 9 and 45°C as a model reaction. The results are expressed as a conversion of D-glucose to gluconic acid as a function of time, which is followed by titration with aqueous NaOH (**Figure 5.6a**). The analysis of the products by nuclear magnetic resonance spectroscopy (NMR) revealed the presence of glucose and gluconic acid, confirming that there are no side reactions or isomerizations taking place

(Appendix). Conversion is increasing with mesopore volume in the series of Au-STCs, starting from no detectable conversion for Au-STC-1, to full conversion in 189 minutes given by reaction with Au-STC-8. The fastest full conversion is accomplished with Au-CMK-3 after 53 minutes. This can be translated to the catalytic activity, expressed as a metal time yield (MTY), which is the overall rate of the catalytic reaction normalized by the total amount of metal. The MTY when Au-CMK-3 is used equals to 60.6 mol_{Glc} min^{-1} mol_{Au}^{-1}. In comparison, the least active mesoporous catalyst, Au-STC-2 shows the significantly lower activity of 3.9 mol_{Glc} min^{-1} mol_{Au}^{-1} (**Table 5.2** and **Figure 5.6b**).

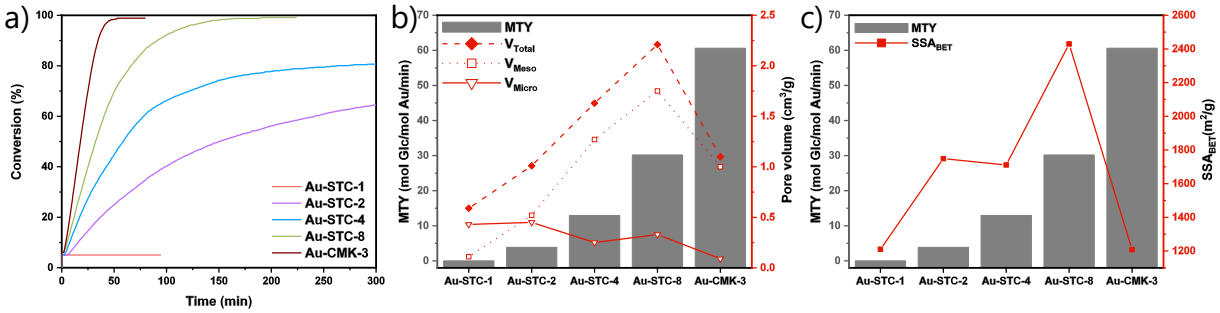

Figure 5.6. *a) Conversion of D-glucose vs. time diagram. Correlation between catalytic activities (metal time yield) of the catalysts and their porosities, expressed through: b) total pore volume (V_{total}), DFT mesopore volume (V_{meso}), DFT micropore volume (V_{micro}), and c) SSA_{BET}.*

TEM investigations of the catalysts after the reaction show no significant changes in the morphology or average AuNP size distribution (**Table 5.2**, and **Figure S 13**, Appendix). Therefore, the effects of particle agglomeration during the reaction can be ruled out for all catalysts, as it is expected in such mild reaction conditions. As it was previously mentioned, there is indeed a minor difference in the average AuNP sizes ranging between 4.7 nm for the least active Au-STC-1, to 4.1 nm for the most active Au-CMK-3. However, although AuNP sizes are a crucial parameter in this reaction, the differences in MTY span over more than one order of magnitude, thus the minor AuNPs size differences as present here alone cannot explain the trends in activity (**Table 5.2**, and **Figure S 14**, Appendix). Moreover, the catalysts having identical average AuNPs size, Au-STC-4 and Au-STC-8, differ significantly in their activity, and slightly larger particles in Au-STC-1 can hardly be responsible for the complete absence of its catalytic activity. To ensure that the catalysis solely occurs on supported AuNPs and there is no contribution from unsupported AuNPs

in the D-glucose solution, the metal leaching test of the reaction solution was conducted.[267-268] The ICP-OES measurements reveal an Au concentration between 0.031 and 0.072 mg L^{-1} in the solution after the reaction. This corresponds to less than 1% of the overall added Au and confirms that the supported AuNPs are the major source of catalytic activity (**Table S 2**, Appendix). The results suggest that for the series of STC-supported catalysts, the catalytic activity of AuNPs increases with increasing the amount of mesopores, leading to higher and faster D-glucose conversion (**Figure 5.6b**). This is in agreement with previous studies where catalysis with supported metal NPs requires a high surface area of the porous support, because of sufficient dispersion of the active phase.[210, 212, 266, 269] However, all of the supports studied here are highly porous, and the most active catalyst Au-CMK-3, and the one exhibiting no catalytic activity, Au-STC-1, have a comparable surface area. The porous system of Au-CMK-3 suggests that the presence, amount, and architecture of mesopores, together with the overall porosity, play a crucial role. Namely, the pores of ordered mesoporous CMK-3 have narrow diameter distribution around 6 nm, which are well interconnected without bottlenecks. Together with micropores present inside the hexagonally arranged carbon rods, this material has a hierarchical network of pores. On the other hand, the pores in STC materials are built based on the clustering of $ZnCl_2$ as a salt template. The resulting porous system is still interconnected but with a larger portion of pores that are less accessible for the solvent or the solute. In all the catalysts, the active phase is mainly located on the surface of the material, as supported by XPS measurements. The possibility of AuNPs being deposited inside and confined within the mesopores can be ruled out by the relation between porosity and TEM particle size analysis, as discussed above. With respect to similar surface chemistry of the carbons and comparable average AuNPs size and their position on the supports, it can be concluded that the local concentration of oxygen and D-glucose around AuNPs is a decisive parameter for the catalytic activity of these materials. STCs have broad distribution of mesopore diameters and their porous system has a low connectivity with the surface of the material, where the AuNPs are located. Therefore, pores of STCs can poorly contribute to the enhancement of oxygen and D-glucose dissolution and thus the concentration of the reactants near the catalytically active sites remains limited. On the contrary, a large amount of uniform narrow mesopores connected to the surface of the

catalyst, as in Au-CMK-3, can lead to a nanoconfinement effect that significantly enhances the activity of the catalyst. The water that is under nanoconfinement shows higher gas solubility than bulk water.[242-243, 259] That is, the nanoconfinement increases the catalytic activity of Au-CMK-3 catalyst by increasing the concentration of the reactant in the proximity of the active sites. This sort of "direct communication" between oxygen-enriched pores and AuNPs on the external particle surface is not present for the STC supports that suffer from a significant contribution of blocked or closed mesopores with restricted connection to the AuNPs. Since the catalytic activity of the metal NPs of similar size and electronic state on the support with similar chemical structure must be the same, the term "apparent catalytic activity" will be introduced to distinguish the observed phenomena from intrinsic catalytic activity. In other terms, the difference in the rate of D-glucose oxidation is not a consequence of the properties of the active phase of the catalyst, but is caused by changes of their local environment induced by the catalytic support. It can be further seen from the absence of apparent catalytic activity for the purely microporous STC-1 that micropores do not contribute to this enhancement of the concentration of reactants near the catalytically active centers. This is likely caused by the limited wetting of narrow hydrophobic pores with the polar water molecules. In contrast, the open mesopores in CMK-3 can serve as a reservoir of confined water with a high concentration of oxygen and D-glucose, leading to a significantly enhanced apparent catalytic activity in D-glucose conversion.

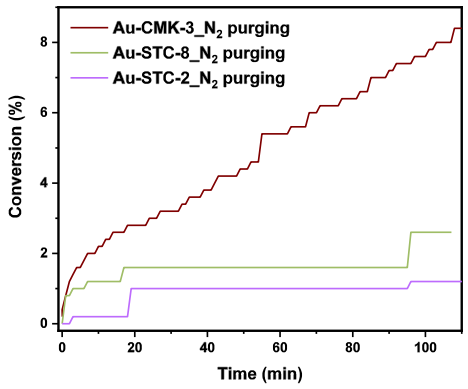

Figure 5.7. *Conversion of D-glucose vs. time diagram without the additional supply of oxygen during the reaction using the catalysts Au-STC-2, Au-STC-8, and Au-CMK-3.*

Control experiments testing the hypothesis that water confined in the mesopores of Au-CMK-3 acts as an oxygen reservoir were performed by saturating the dispersion of a catalyst in water with oxygen, and subsequently starting the catalytic reaction without further addition of gas. To ensure that the contribution of oxygen from the atmosphere is minimized, the reaction vessel was purged with nitrogen. Au-STC-8 and Au-STC-2 with disordered mesopores showed minor catalytic activity in the D-glucose oxidation reaction, whereas Au-CMK-3 exhibited a steady conversion (**Figure 5.7**). This indicates that a larger amount of oxygen is dissolved and stored in the pores of Au-CMK-3, which enables oxidation of a significant amount of D-glucose even without a continued supply of oxygen to the reaction medium.

In Chapter 5.1, it has been shown that the pore architecture of carbon materials can have a crucial influence on the apparent catalytic activity of supported AuNPs. This was experimentally proved on a series of catalysts consisting of AuNPs supported on carbons with different pore volumes and geometry in the micropore and mesopore region and comparable surface chemistry. The open and ordered mesopores in hierarchical carbon provide a network for nanoconfined water, which then enriches reactants near to the active sites, leading to higher apparent catalytic activity. To promote the apparent catalytic activity of the most active catalyst additionally, an approach in the following Chapter 5.2 will be based on the introduction of less cohesive liquids such as perfluorinated compounds near the active phase of the catalyst.

5.2. Promoting the Oxygen Delivery by Formation of Pickering Emulsions with Perfluorocarbon

After increasing the oxygen concentration in the internal area of the catalyst in previous chapter, the present chapter focuses on increasing the concentration of oxygen in the external environment of the catalyst. This is accomplished by providing an adequate medium for each phase of the catalytic system, and by bringing them in close contact. PFC serve as efficient solvent for oxygen and water as a solvent for glucose, which are effectively brought together through a formation of emulsions. The most active catalyst established in Chapter 5.1, Au-CMK-3 (further denoted as Au-C), was used as a stabilizer of

PFC (Au-C-PFC) in aqueous D-glucose solution. Although confinement at the interface of emulsion droplets causes a lowering of the active surface area, the introduction of 2 vol.% increased the "apparent catalytic activity" of the Au-C catalyst. A comparison with the dispersion of the catalyst alone, as well as with Pickering emulsion containing hydrocarbon instead of perfluorocarbon (Au-C-HC) is given.

5.2.1. Synthesis and Characterization of the Catalyst and its Pickering Emulsion with Perfluorocarbon

The Au-C catalyst has been obtained by deposition of 1 wt % of AuNPs on the ordered mesoporous carbon CMK-3, synthesized by a procedure described in Chapter 5.1.1. Afterward, the Au-C catalyst dispersed in water was used to emulsify small volumes of PFC by vortex mixing (**Figure 5.8**).

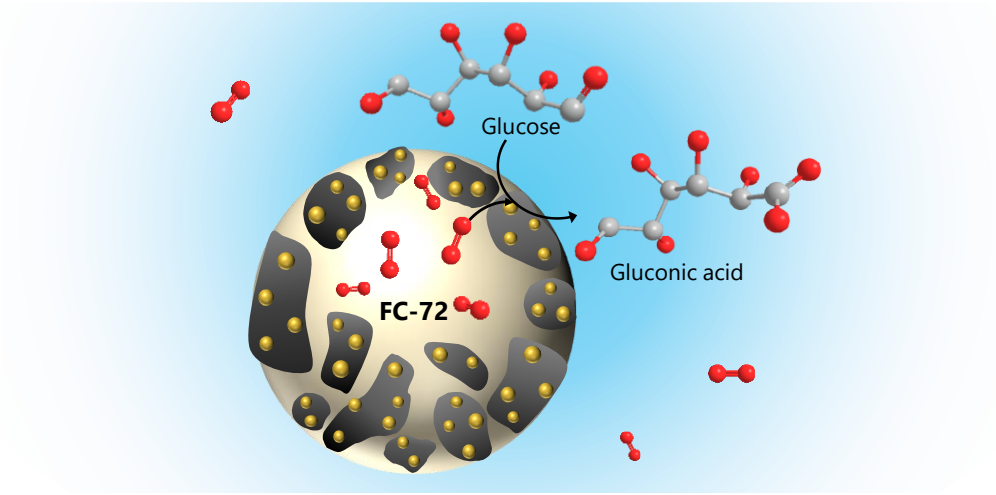

Figure 5.8. *Structure of the Au-C-PFC Pickering emulsion, consisting of perfluorohexane stabilized by particles of Au-C catalyst in aqueous solution of glucose.*

To truly utilize the exceptional property of PFCs for dissolving gases, it is beneficial to bring the PFC into close contact with the catalyst. This is effectively accomplished by increasing the interfacial area of PFCs in water, by the formation of particle-stabilized (Pickering) emulsions. Small volumes of fluorocarbon oil FC-72 (perfluorohexane) were emulsified within aqueous dispersions of the Au-C catalyst (0.2 mg mL^{-1}) by vortex mixing. The hydrophobic particles of carbon-supported catalyst preferentially reside at the oil/water interface, thereby effectively creating the perfluorocarbon droplets (Au-C-PFC) (**Figure**

5.9). A series of particle-stabilized PFC emulsions were prepared to investigate the optimal volume fraction of PFC. When high volume fractions of PFCs (≥4 vol.%) were used for the creation of emulsions, the coverage of the emulsion surface was incomplete and droplet coalescence occurred, thus decreasing the effective surface area. Lowering the volume of the dispersed oil phase (≈2 vol.%) resulted in stable emulsion droplets with an average diameter of 245 μm. Further decreasing of the PFC volume in the system (>2 vol.%) resulted in densely congregated Au-C particles at the oil/water interface. Moreover, a control system comprising of hydrocarbon Pickering emulsion was prepared in the same fashion, by stabilizing 2 vol.% of bromohexane with Au-C catalyst (Au-C-HC). Hydrocarbon has comparable interactions with Au-C like perfluorocarbon, yielding stable droplets at this volume fraction.

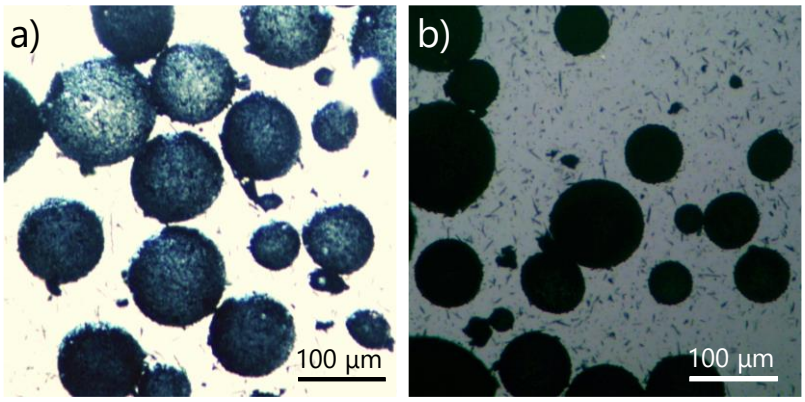

Figure 5.9. *Microscopy images of Au-C-PFC Pickering emulsion in water.*

After the preparation and characterization of the series of particle-stabilized emulsions of PFCs in the aqueous phase, the feasibility of using these oxygen-loaded microcontainers for increasing the activity of D-glucose oxidation was tested.

5.2.2. Activity of the Perfluorocarbon Emulsions Stabilized by Au-Carbon Catalysts in Liquid-Phase D-Glucose Oxidation

The catalytic activities of the newly prepared emulsion systems for the model reaction of D-glucose oxidation with molecular oxygen were compared to the activity of the Au-C catalyst alone, as well as to Au-C-HC system. The reactions were operated in aqueous solution at pH = 9 and 30 °C. The conditions used in Chapter 5.1.2 were modified because

of the physical properties of perfluorohexane, such as low boiling point (56 °C at 101.3 kPa) and relatively high vapor pressure (30.9 kPa at 25 °C). For this reason, also the oxygen flow was decreased from ≈ 250 mL min^{-1} to ≈ 50 mL min^{-1}, and concentration of D-glucose increased from 0.1 M to 0.2 M. This corresponds to molar ratio of D-glucose to Au of ≈ 20000, in comparison to 2000 in Chapter 5.1.2. The basicity of the solution was maintained by titration with NaOH, and the volume of the added base can be directly correlated with the conversion of D-glucose to gluconic acid (**Figure 5.10a** and **b**).

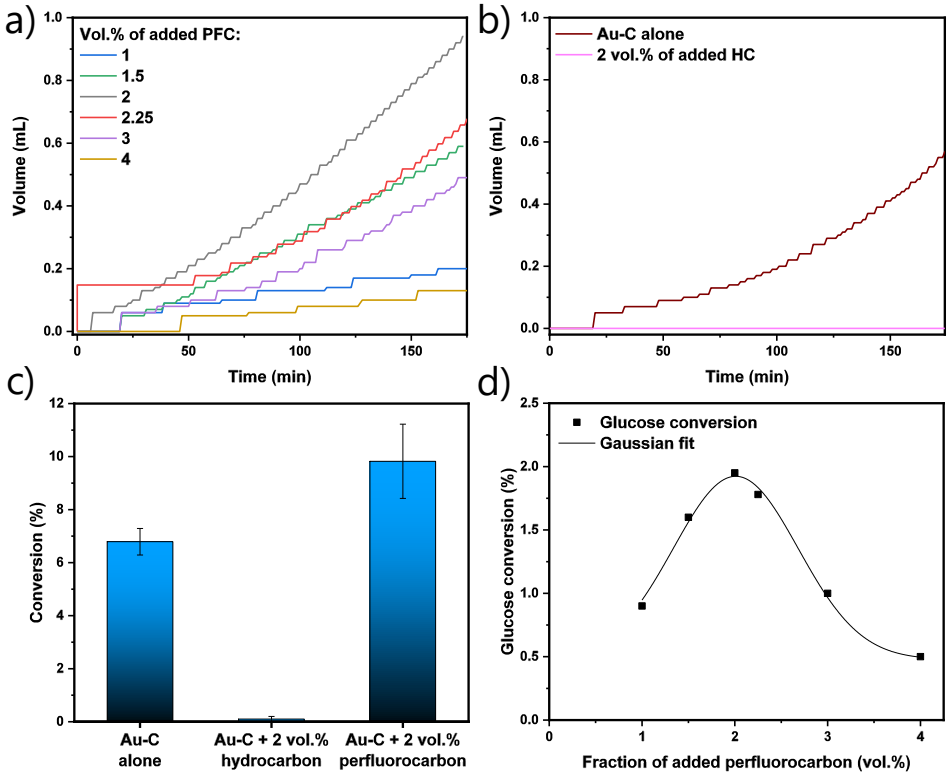

Figure 5.10. *Volume of added NaOH vs. time diagrams of D-glucose oxidation using Au-C catalyst with a) different volume fractions of added perfluorocarbon and b) with 2 vol.% of added hydrocarbon. c) Diagram comparing three tested catalytic systems, and d) dependence of D-glucose conversion on the fractions of added PFC.*

When optimal volume fractions of PFC (≈2 vol.%) were utilized for the preparation of particle-stabilized emulsions, the rate of the reaction and thus the apparent catalytic activity is higher than the reaction without added PFC, or with added HC (**Figure 5.10c**). One hour after the start of the reaction, the Au-C catalyst dispersed in the aqueous solution of D-glucose achieves a glucose conversion of 1.3 %, while the same amount of catalyst in

the Au-C-HC system shows no detectable catalytic activity (**Figure 5.10b** and **Figure S 15**, **Appendix**). This difference is even more pronounced in the later stage of reaction when after 170 minutes Au-C converts 6.8 % of D-glucose, and the Au-C-HC remains inactive (**Figure 5.10b** and **c**). This can be explained by a lower active surface of the catalyst, due to its position on the droplet interface. Therefore, a part of the Au-C surface immobilized on the interface is not in contact with the solution of the reactants – D-glucose and oxygen, and by that not involved in the catalytic reaction. As previously seen, this is the case for both PFC and HC emulsions. However, Au-C-PFC shows noticeably higher catalytic activity than the Au-C catalyst alone, with a conversion of 9.8 % after 170 minutes (**Figure 5.10c**). This can be ascribed to the ability of PFCs to dissolve gases exceptionally well, behaving like nearly ideal gas-like fluids. Fluorine has extremely low polarizability, meaning that the van der Waals interactions between PFC molecules are also very weak, which makes PFCs the best class of liquids for the solubility of the gases. In the Au-C-PFC system, the described property of PFCs leads to the increase of the local concentration of oxygen in the proximity of the catalyst. In this way, the oxidation of D-glucose on the surface of AuNPs is promoted by increasing the concentration of an oxidant. Consequently, the gas-dissolving effect of PFCs promotes the catalytic activity of the Au-C catalyst only when the stable emulsion is created. This is described by the volcano-like dependence of D-glucose conversion on the volume fraction of PFC in the Au-C-PFC system after 1 h (**Figure 5.10d**). The highest conversion is obtained with the optimal fraction of 2 vol.% of PFC, where both less and more PFC lead to a decrease in the activity of the catalytic system. When the PFC fraction is lower than the optimal volume, the Au-C particles stack at the droplet interface. This effect in combination with the lower capability of such a small PFC volume to deliver oxygen leads to lower apparent catalytic activity. On the other hand, when the PFC content is too high, the amount of Au-C particles surface is not sufficient for the stabilization of droplets. Therefore, the instability of emulsion negatively influences the catalytic activity. Expectedly, under the conditions applied, the overall conversion 170 minutes after the start of the reaction are lower than in the previous chapter, due to the lower temperature and oxygen flow rate, as well as the higher molar ration between glucose and gold.

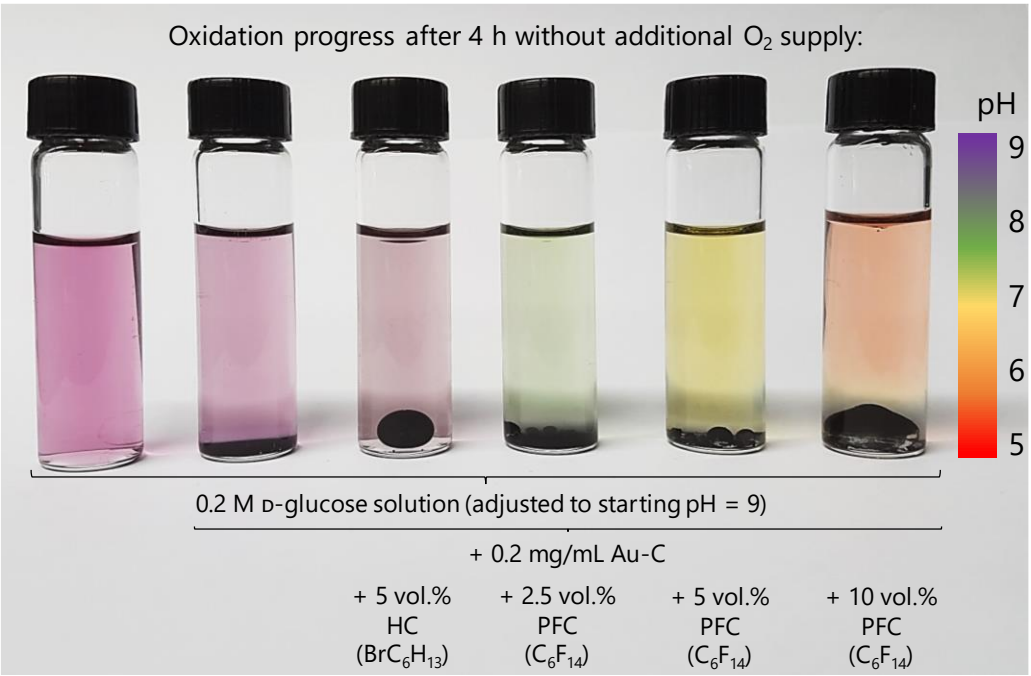

Figure 5.11. *The progress of D-glucose oxidation after 4 h without additional oxygen supply, comparing different catalytic systems.*

Furthermore, the effect of oxygen delivery through the PFC phase is observed even without additional oxygen supply during the reaction. The catalytic reactions in the absence of oxygen were conducted for three previously compared systems, including Au-C catalyst in aqueous solution, Au-C-HC, and Au-C-PFC with different volume fractions of PFC (**Figure 5.11**). The reaction progress was monitored by the universal pH indicator, which was added to the D-glucose solution before the reaction. The starting pH value was adjusted to 9, catalysts were added, and the vials were closed. After 4 h, the pH values lowered only in systems with PFC, whereas Au-C and Au-C-HC showed no significant change in the pH value. In the series from 2.5 to 10 vol.% PFC, an increasing amount of PFC led to a more notable decrease in pH, meaning that more gluconic acid was formed when a higher fraction of PFC was present in the system. This is not surprising since in this sort of static experiment, without additional oxygen supply or stirring, the stability of the emulsion is less important, and available oxidant is a decisive factor. The experiments reported here prove that with the addition of PFC and the Au-C catalyst to the solution of D-glucose, it is possible to obtain the oxidation product even without the external supply of oxidant.

It was shown that the remarkable capability of perfluorocarbons to dissolve gases may be employed to promote the catalytic activity of the Au-CMK-3 catalyst in the reaction of D-glucose oxidation with molecular oxygen. This is enabled by increasing the local concentration of the oxidant in the surroundings of the gold nanoparticles. Compared to catalysts immobilized at the interface of hydrocarbons with lower O_2 carrier capabilities, the introduction of 2 vol.% PFC increased the throughput of the oxidation reaction by a 5-fold.

In Chapter 5, it was demonstrated that the control over the catalytic activity of the reaction in the three-phase system can be indirectly established by nanoconfinement or introduction of less cohesive liquids such as perfluorinated compounds. In this way, the enhancement of catalytic activity is not a consequence of intrinsic differences in the active phase of the catalyst, but the differences arise from changes in their local environment. This opens up new possibilities for the rational design of catalysts, beyond the design of the porous support material and the active phase of the catalyst. With the same reaction conditions, the concentration of reactants, and physicochemical properties of the active phase, nanoconfinement of the solvent molecules can drastically increase the kinetics of the reaction, as it was presented in Chapter 5.1. This study also illustrates that higher surface area of the support and therefore better dispersion of NPs does not necessarily yield a more active material. The pore system of the carbon has to meet certain requirements, to be able to affect the local environment of the catalyst. In addition to the increased concentration of oxygen due to the water confinement in the mesopores of carbon, the local concentration of the oxidant can also be increased by introducing a potent gas carrier into the reaction medium. Such compounds are perfluorocarbons introduced in Chapter 5.2, which are optimally utilized in water solution by the formation of emulsions. Stabilization of droplets by solid particles of the catalyst enables to avoid the use of surfactants and provides an interface between oxygen-rich PFC phase, Au-C catalyst, and D-glucose solution. This strategy offers a possibility to overcome the limited solubility of gases in aqueous reaction media, which is often the rate-limiting step of catalytic reactions.

6. Summary, Conclusions, and Perspectives

The central motivation of this thesis was to gain a deeper understanding of structural characteristics and structure-activity relationships of porous carbon materials. Various approaches were taken for these purposes, including different synthesis techniques, means of functionalization, and applications. The materials reported in this work include hierarchical carbons, carbon–carbon composites, heteroatom-doped carbons, and metal-functionalized carbons that are utilized in two different applications, for chiral separation, and in heterogeneous catalysis.

Chapter 4.1 described an approach for obtaining mesoporous carbons with an enantioselective surface by direct carbonization of a chiral precursor. This ensured the introduction of chiral information in the resulting carbons in a regular manner, throughout the body of material. Two enantiomers of chiral ionic liquids (CIL) based on amino acid tyrosine were used as carbon precursors and ordered mesoporous silica SBA-15 served as a hard template for obtaining porosity (4.1.1). The structural characterization of synthesized carbons revealed that their porosity, morphology, and chemical composition of the bulk and the surface is almost identical, thus the differences in interactions with chiral species arise because of their chiral nature (4.1.2). The chiral recognition of the prepared carbons has been tested in the solution by isothermal titration calorimetry with enantiomers of Phenylalanine as probes, resulting in the enantiomeric ratio of L-m-carbon for Phenylalanine of (D/L) = 1.88, and of D-m-carbon (L/D) = 1.34. Chiral vapor adsorption with 2-butanol enantiomers as probes also revealed the differences in the affinity of carbons towards two enantiomers.

The atomic efficiency of the chiral ionic liquid precursors was increased in Chapter 4.2, through the formation of stable composites of pristine carbon and CIL-derived coating. Moreover, the control over the porosity was established independently from the formation of a chiral carbon. A C_2N-type polar coating deposited between a pristine carbon and chiral coating ensured a homogeneous layer that promoted the interactions with CIL based on amino acid proline. Following the lessons from the previous chapter, it was expected that the L- and D-composites have the opposite interactions with chiral molecules, despite their

very similar structural and chemical properties (4.2.1). After the same set of experiments for the investigation of chirality, the enantiomeric ratios for phenylalanine of the composites reported herein were even higher, and they equaled (L/D) = 8.4 for L-composite, and (D/L) = 2.7 for D-composite (4.2.2). The chiral recognition was more pronounced in the gas phase, without the influence of the solvent. The enantiomeric ratio expressed on 1.7 torr of the adsorption isotherm of L-composite for butanol is (S/R) = 1.5, and of D-composite is (R/S) = 1.7, whereas at the highest uptake of butanol (S/R) = 1.3 for L-composite, and (R/S) = 1.3 for D-composite. Chapter 4 has expanded the knowledge about porous carbons and their potential novel application that has not been extensively studied so far. It was presented that the chiral information can be translated from the precursor to the carbon material, as well as how different porosity of the obtained materials can affect the chiral recognition.

Chapter 5 presented a more common application of carbon materials, but in a rather interesting system on the interface between gas, liquid, and solid. In Chapter 5.1 it was shown that the kinetics of D-glucose oxidation reaction can be enhanced by increasing the local concentration of the reactants around the active phase of the catalyst. This was accomplished by preparing a series of gold nanoparticles catalysts supported on salt-templated carbons with different porosities, as well as on the ordered mesoporous carbon, CMK-3. The characterization of the catalysts led to the conclusion that the surface chemistry, content, and the oxidation state of gold, and the average nanoparticle sizes are comparable in the entire series, meaning that their performance was affected by the pore structures (5.1.1). In contrast to purely microporous carbon support with the less wettable internal surface without any detectable catalytic activity, AuNPs supported on mesoporous carbons showed much higher activity (metal time yield), between 3.8 and 60.6 $mol_{Glc}\ min^{-1}\ mol_{Au}^{-1}$, depending on volume and geometry of the mesopores (5.1.2). A large amount of uniform narrow mesopores connected to the surface of the Au-CMK-3 catalyst lead to the water confinement, which increased the solubility of the oxygen in the proximity of the catalyst and thereby increased the apparent catalytic activity of this catalyst.

The possibility of indirect tuning of the catalytic activity, by the control of the local environment of the catalyst was employed in Chapter 5.2. The approach taken for further promoting the activity of the Au-CMK-3 catalyst was the introduction of less cohesive liquids such as perfluorinated compounds near the active phase of the catalyst. This was achieved by a formation of catalyst particle-stabilized emulsions of perfluorocarbon in aqueous D-glucose solution (5.2.1). When a stable emulsion was created, the gas-dissolving effect of perfluorocarbons promotes the catalytic activity of the catalyst. Furthermore, oxygen delivery through the perfluorocarbon phase lead to catalytic activity even in the absence of additional oxygen supply (5.2.2).

The findings reported within this thesis are an important step in the understanding of the structure-related properties of carbon materials. Notwithstanding, there is a perspective for improving the characteristics of newly synthesized materials, or expanding their field of application. Porous carbons and carbon composites with the enantioselective surface presented in Chapter 4 could be further applied for the separation of racemic mixtures, as this is closer to realistic conditions of chiral separations. This could also be accomplished in more harsh conditions of temperature and pH, or under applied electric potential, to underline the clear advantage of carbons over other less robust porous materials. More pronounced chiral recognition could potentially be accomplished with precursors containing higher amount of chiral functions, such as CILs with multiple chiral centers. Enantioselective porous carbons could be designed to be spatially selective and thus possess inherent chirality, ideally resulting in two types of carbons with opposite curvature. The control of catalytic activity by the local environment of a catalyst, established in Chapter 5, has a general character and it is not limited to the particular D-glucose oxidation reaction. These concepts could be applied in any liquid phase catalytic reaction that involves gaseous reactants. Moreover, they are not limited to carbons as support materials, since the solvent confinement can occur in any porous material with appropriate pore structure. Another parameter that can possibly affect the gas solubility within the pores is the surface chemistry of carbon materials. Additional studies involving a series of ordered mesoporous carbons with different pore sizes can likely result in even more pronounced nanoconfinement effects. Further investigation of the porous structure

of carbons, including the interconnectivity of the pores and the architecture of the materials in general could be pursued.

7. References

1. de Jong, K.P., *General Aspects*, in *Synthesis of Solid Catalysts*, de Jong, Editor. **2009**, Wiley‐VCH: Weinheim, Germany. p. 1-11.
2. Grand View Research, *Catalyst Market Size, Share & Trends Analysis Report* **2020**.
3. Ertl, G., Knözinger, H., Schüth, F., and Weitkamp, J., *Handbook of Heterogeneous Catalysis*. **2008**, Wiley-VCH: Weinheim, Germany.
4. Thomas, J.M. and Thomas, W.J., *Principles and Practice of Heterogeneous Catalysis*. **2015**, Wiley-VCH: Weinheim, Germany.
5. Wilson, K. and Lee, A.F., *Heterogeneous Catalysts for Clean Technology*. **2014**, Wiley-VCH: Weinheim, Germany.
6. Chorkendorff, I. and Niemantsverdriet, J.W., *Concepts of Modern Catalysis and Kinetics*. **2003**, Wiley‐VCH: Weinheim, Germany.
7. Nguyen, L.A., He, H., and Pham-Huy, C., *International journal of biomedical science : IJBS* **2006**, *2*, 2, 85-100.
8. Brooks, W.H., Guida, W.C., and Daniel, K.G., *Current topics in medicinal chemistry* **2011**, *11*, 7, 760-770.
9. Jeschke, P., *Pest Management Science* **2018**, *74*, 11, 2389-2404.
10. European Medicines Agency, Directive 75/318/EEC as amended, *Investigation of Chiral Active Substances* **1993**, Available from: https://www.ema.europa.eu/en/documents/scientific-guideline/investigation-chiral-active-substances_en.pdf.
11. U.S. Food and Drug Administration, Center for Drug Evaluation and Research, *Development of New Stereoisomeric Drugs* **1992**, Available from: https://www.fda.gov/regulatory-information/search-fda-guidance-documents/development-new-stereoisomeric-drugs.
12. Lewis, D.L., Garrison, A.W., Wommack, K.E., Whittemore, A., Steudler, P., and Melillo, J., *Nature* **1999**, *401*, 6756, 898-901.
13. Smith, S.W., *Toxicological Sciences* **2009**, *110*, 1, 4-30.
14. Scriba, G.K.E., *Chiral Separations: Methods and Protocols*. **2019**, Humana: New York, NY, USA.
15. Henry, C.R., *Surface Science Reports* **1998**, *31*, 7, 231-325.
16. Schauermann, S., Nilius, N., Shaikhutdinov, S., and Freund, H.-J., *Accounts of Chemical Research* **2013**, *46*, 8, 1673-1681.
17. Gogotsi, Y. and Presser, V., *Carbon Nanomaterials*. **2014**, CRC Press: Boca Raton, FL, USA.
18. Riedel, E., *Anorganische chemie*. **2011**, Walter de Gruyter: Berlin, Germany.
19. Jelley, R.E. and Blackman, A.G., *Nature Chemistry* **2019**, *11*, 9, 751-756.
20. Wöhler, F., *Annalen der Physik* **1828**, *88*, 2, 253-256.
21. Shorter, J., *Chemical Society Reviews* **1978**, *7*, 1, 1-14.
22. Müllen, K., *ACS Nano* **2014**, *8*, 7, 6531-6541.
23. Scott, L.T., *Angewandte Chemie International Edition* **2004**, *43*, 38, 4994-5007.
24. Iijima, S., *Physica B: Condensed Matter* **2002**, *323*, 1, 1-5.

25. Krueger, A., *Advanced Materials* **2008**, *20*, 12, 2445-2449.
26. Ugarte, D., *Carbon* **1995**, *33*, 7, 989-993.
27. Oschatz, M. and Walczak, R., *C* **2018**, *4*, 4, 56.
28. Thommes, M., Kaneko, K., Neimark, A.V., Olivier, J.P., Rodriguez-Reinoso, F., Rouquerol, J., and Sing, K.S.W., *Pure Appl. Chem.* **2015**, *87*, 1051-1069.
29. Oschatz, M. and Antonietti, M., *Energy & Environmental Science* **2018**, *11*, 1, 57-70.
30. Morris, R.E. and Wheatley, P.S., *Angewandte Chemie International Edition* **2008**, *47*, 27, 4966-4981.
31. Dai, L., Chang, D.W., Baek, J.-B., and Lu, W., *Small* **2012**, *8*, 8, 1130-1166.
32. Feng, X., *Nanocarbons for advanced energy storage*. **2015**, Wiley Online Library: Weinheim, Germany.
33. Gerber, I.C. and Serp, P., *Chemical Reviews* **2020**, *120*, 2, 1250-1349.
34. Philippe Serp, J.L.F., *Carbon Materials for Catalysis*. **2009**, John Wiley & Sons, Inc.: Hoboken, NJ, USA.
35. Antonietti, M., Lopez-Salas, N., and Primo, A., *Advanced Materials* **2019**, *31*, 13, 1805719.
36. Ahmadpour, A. and Do, D.D., *Carbon* **1996**, *34*, 4, 471-479.
37. Marsh, H. and Rodríguez-Reinoso, F., *Activation Processes (Thermal or Physical)*, in *Activated Carbon*. **2006**, Elsevier Science Ltd: Oxford, UK. p. 243-321.
38. Molina-Sabio, M. and Rodríguez-Reinoso, F., *Colloids and Surfaces A: Physicochemical and Engineering Aspects* **2004**, *241*, 1, 15-25.
39. Caturla, F., Molina-Sabio, M., and Rodríguez-Reinoso, F., *Carbon* **1991**, *29*, 7, 999-1007.
40. Wang, J. and Kaskel, S., *Journal of Materials Chemistry* **2012**, *22*, 45, 23710-23725.
41. Marsh, H. and Rodríguez-Reinoso, F., *Activation Processes (Chemical)*, in *Activated Carbon*. **2006**, Elsevier Science Ltd: Oxford, UK. p. 322-365.
42. Figueiredo, J.L., *Journal of Materials Chemistry A* **2013**, *1*, 33, 9351-9364.
43. Pekala, R.W., *Journal of Materials Science* **1989**, *24*, 9, 3221-3227.
44. Biener, J., Stadermann, M., Suss, M., Worsley, M.A., Biener, M.M., Rose, K.A., and Baumann, T.F., *Energy & Environmental Science* **2011**, *4*, 3, 656-667.
45. Yang, X.-Y., Chen, L.-H., Li, Y., Rooke, J.C., Sanchez, C., and Su, B.-L., *Chemical Society Reviews* **2017**, *46*, 2, 481-558.
46. Xia, Y., Yang, Z., and Mokaya, R., *Nanoscale* **2010**, *2*, 5, 639-659.
47. Liang, C., Li, Z., and Dai, S., *Angewandte Chemie International Edition* **2008**, *47*, 20, 3696-3717.
48. Nishihara, H. and Kyotani, T., *Advanced Materials* **2012**, *24*, 33, 4473-4498.
49. Benzigar, M.R., Talapaneni, S.N., Joseph, S., Ramadass, K., Singh, G., Scaranto, J., Ravon, U., Al-Bahily, K., and Vinu, A., *Chemical Society Reviews* **2018**, *47*, 8, 2680-2721.
50. Lee, J., Kim, J., and Hyeon, T., *Advanced Materials* **2006**, *18*, 16, 2073-2094.
51. Gilbert, M.T., Knox, J.H., and Kaur, B., *Chromatographia* **1982**, *16*, 1, 138-146.
52. Göltner, C.G. and Weißenberger, M.C., *Acta Polymerica* **1998**, *49*, 12, 704-709.
53. Schüth, F., *Angewandte Chemie International Edition* **2003**, *42*, 31, 3604-3622.
54. Liu, B., Shioyama, H., Akita, T., and Xu, Q., *Journal of the American Chemical Society* **2008**, *130*, 16, 5390-5391.

55. Hwang, J., Ejsmont, A., Freund, R., Goscianska, J., Schmidt, B.V.K.J., and Wuttke, S., *Chemical Society Reviews* **2020**.
56. Hwang, J., Walczak, R., Oschatz, M., Tarakina, N.V., and Schmidt, B.V.K.J., *Small* **2019**, *15*, 37, 1901986.
57. Bhadra, B.N., Vinu, A., Serre, C., and Jhung, S.H., *Materials Today* **2019**, *25*, 88-111.
58. Shen, K., Chen, X., Chen, J., and Li, Y., *ACS Catalysis* **2016**, *6*, 9, 5887-5903.
59. Oschatz, M., Borchardt, L., Thommes, M., Cychosz, K.A., Senkovska, I., Klein, N., Frind, R., Leistner, M., Presser, V., Gogotsi, Y., and Kaskel, S., *Angewandte Chemie International Edition* **2012**, *51*, 30, 7577-7580.
60. Borchardt, L., Oschatz, M., and Kaskel, S., *Materials Horizons* **2014**, *1*, 2, 157-168.
61. Lu, A.-H., Zhao, D., and Wan, Y., *Nanocasting: A Versatile Strategy for Creating Nanostructured Porous Materials*. **2009**, The Royal Society of Chemistry: Cambridge, UK.
62. Lu, A.-H. and Schüth, F., *Advanced Materials* **2006**, *18*, 14, 1793-1805.
63. Kyotani, T., Nagai, T., Inoue, S., and Tomita, A., *Chemistry of Materials* **1997**, *9*, 2, 609-615.
64. Rodriguez-Mirasol, J., Cordero, T., Radovic, L.R., and Rodriguez, J.J., *Chemistry of Materials* **1998**, *10*, 2, 550-558.
65. Itoi, H., Nishihara, H., Kogure, T., and Kyotani, T., *Journal of the American Chemical Society* **2011**, *133*, 5, 1165-1167.
66. Kresge, C.T., Leonowicz, M.E., Roth, W.J., Vartuli, J.C., and Beck, J.S., *Nature* **1992**, *359*, 6397, 710-712.
67. Zhao, D., Feng, J., Huo, Q., Melosh, N., Fredrickson, G.H., Chmelka, B.F., and Stucky, G.D., *Science* **1998**, *279*, 5350, 548-552.
68. Sakamoto, Y., Kaneda, M., Terasaki, O., Zhao, D.Y., Kim, J.M., Stucky, G., Shin, H.J., and Ryoo, R., *Nature* **2000**, *408*, 6811, 449-453.
69. Ryoo, R., Kim, J.M., Ko, C.H., and Shin, C.H., *The Journal of Physical Chemistry* **1996**, *100*, 45, 17718-17721.
70. Liu, X., Tian, B., Yu, C., Gao, F., Xie, S., Tu, B., Che, R., Peng, L.-M., and Zhao, D., *Angewandte Chemie International Edition* **2002**, *41*, 20, 3876-3878.
71. Che, S., Garcia-Bennett, A.E., Yokoi, T., Sakamoto, K., Kunieda, H., Terasaki, O., and Tatsumi, T., *Nature Materials* **2003**, *2*, 12, 801-805.
72. Ryoo, R., Joo, S.H., and Jun, S., *The Journal of Physical Chemistry B* **1999**, *103*, 37, 7743-7746.
73. Jun, S., Joo, S.H., Ryoo, R., Kruk, M., Jaroniec, M., Liu, Z., Ohsuna, T., and Terasaki, O., *Journal of the American Chemical Society* **2000**, *122*, 43, 10712-10713.
74. Wan, Y. and Zhao, *Chemical Reviews* **2007**, *107*, 7, 2821-2860.
75. Ruthstein, S., Schmidt, J., Kesselman, E., Talmon, Y., and Goldfarb, D., *Journal of the American Chemical Society* **2006**, *128*, 10, 3366-3374.
76. Khodakov, A.Y., Zholobenko, V.L., Impéror-Clerc, M., and Durand, D., *The Journal of Physical Chemistry B* **2005**, *109*, 48, 22780-22790.
77. Flodström, K., Wennerström, H., Teixeira, C.V., Amenitsch, H., Lindén, M., and Alfredsson, V., *Langmuir* **2004**, *20*, 23, 10311-10316.
78. Meng, Y., Gu, D., Zhang, F., Shi, Y., Yang, H., Li, Z., Yu, C., Tu, B., and Zhao, D., *Angewandte Chemie International Edition* **2005**, *44*, 43, 7053-7059.

79. Florent, M., Xue, C., Zhao, D., and Goldfarb, D., *Chemistry of Materials* **2012**, *24*, 2, 383-392.
80. Liu, J., Yang, T., Wang, D.-W., Lu, G.Q., Zhao, D., and Qiao, S.Z., *Nature Communications* **2013**, *4*, 1, 2798.
81. Zhang, F., Meng, Y., Gu, D., Yan, Yu, C., Tu, B., and Zhao, D., *Journal of the American Chemical Society* **2005**, *127*, 39, 13508-13509.
82. Chuenchom, L., Kraehnert, R., and Smarsly, B.M., *Soft Matter* **2012**, *8*, 42, 10801-10812.
83. Lu, Y., *Angewandte Chemie International Edition* **2006**, *45*, 46, 7664-7667.
84. Fechler, N., Fellinger, T.P., and Antonietti, M., *Advanced Materials* **2013**, *25*, 1, 75-9.
85. Zhu, J., Sakaushi, K., Clavel, G., Shalom, M., Antonietti, M., and Fellinger, T.-P., *Journal of the American Chemical Society* **2015**, *137*, 16, 5480-5485.
86. Liu, X., Fechler, N., and Antonietti, M., *Chemical Society Reviews* **2013**, *42*, 21, 8237-8265.
87. Yan, R., Antonietti, M., and Oschatz, M., *Advanced Energy Materials* **2018**, *8*, 18, 1800026.
88. Liu, X., Giordano, C., and Antonietti, M., *Small* **2014**, *10*, 1, 193-200.
89. Sevilla, M. and Fuertes, A.B., *Carbon* **2006**, *44*, 3, 468-474.
90. Maldonado-Hódar, F.J., Moreno-Castilla, C., Rivera-Utrilla, J., Hanzawa, Y., and Yamada, Y., *Langmuir* **2000**, *16*, 9, 4367-4373.
91. Stein, A., Wang, Z., and Fierke, M.A., *Advanced Materials* **2009**, *21*, 3, 265-293.
92. Li, Y. and Shi, J., *Advanced Materials* **2014**, *26*, 20, 3176-3205.
93. Borchardt, L., Zhu, Q.-L., Casco, M.E., Berger, R., Zhuang, X., Kaskel, S., Feng, X., and Xu, Q., *Materials Today* **2017**, *20*, 10, 592-610.
94. Liu, J., Wickramaratne, N.P., Qiao, S.Z., and Jaroniec, M., *Nature Materials* **2015**, *14*, 8, 763-774.
95. Perovic, M., Qin, Q., and Oschatz, M., *Advanced Functional Materials* **2020**, *30*, 41, 1908371.
96. Paraknowitsch, J.P. and Thomas, A., *Energy & Environmental Science* **2013**, *6*, 10, 2839-2855.
97. Boehm, H.P., *Carbon* **1994**, *32*, 5, 759-769.
98. Oschatz, M., Hofmann, J.P., van Deelen, T.W., Lamme, W.S., Krans, N.A., Hensen, E.J.M., and de Jong, K.P., *ChemCatChem* **2017**, *9*, 4, 620-628.
99. Zhao, L., Fan, L.-Z., Zhou, M.-Q., Guan, H., Qiao, S., Antonietti, M., and Titirici, M.-M., *Advanced Materials* **2010**, *22*, 45, 5202-5206.
100. Sevilla, M., Valle-Vigón, P., and Fuertes, A.B., *Advanced Functional Materials* **2011**, *21*, 14, 2781-2787.
101. Zheng, F., Yang, Y., and Chen, Q., *Nature Communications* **2014**, *5*, 5261.
102. Zhu, X., Tian, C., Chai, S., Nelson, K., Han, K.S., Hagaman, E.W., Veith, G.M., Mahurin, S.M., Liu, H., and Dai, S., *Advanced Materials* **2013**, *25*, 30, 4152-4158.
103. Xiang, Z., Cao, D., Huang, L., Shui, J., Wang, M., and Dai, L., *Advanced Materials* **2014**, *26*, 20, 3315-3320.
104. Yuan, J., Márquez, A.G., Reinacher, J., Giordano, C., Janek, J., and Antonietti, M., *Polymer Chemistry* **2011**, *2*, 8, 1654-1657.
105. Yuan, J., Giordano, C., and Antonietti, M., *Chemistry of Materials* **2010**, *22*, 17, 5003-5012.

106. Walczak, R., Savateev, A., Heske, J., Tarakina, N.V., Sahoo, S., Epping, J.D., Kühne, T.D., Kurpil, B., Antonietti, M., and Oschatz, M., *Sustainable Energy & Fuels* **2019**, *3*, 2819.
107. Walczak, R., Kurpil, B., Savateev, A., Heil, T., Schmidt, J., Qin, Q., Antonietti, M., and Oschatz, M., *Angewandte Chemie International Edition* **2018**, *57*, 33, 10765-10770.
108. Fechler, N., Zussblatt, N.P., Rothe, R., Schlögl, R., Willinger, M.-G., Chmelka, B.F., and Antonietti, M., *Advanced Materials* **2016**, *28*, 6, 1287-1294.
109. Welton, T., *Chemical Reviews* **1999**, *99*, 8, 2071-2084.
110. Paraknowitsch, J.P. and Thomas, A., *Macromolecular Chemistry and Physics* **2012**, *213*, 10 - 11, 1132-1145.
111. Zhang, S., Dokko, K., and Watanabe, M., *Materials Horizons* **2015**, *2*, 2, 168-197.
112. Paraknowitsch, J.P., Zhang, J., Su, D., Thomas, A., and Antonietti, M., *Advanced Materials* **2010**, *22*, 1, 87-92.
113. Lee, J.S., Wang, X., Luo, H., and Dai, S., *Advanced Materials* **2010**, *22*, 9, 1004-1007.
114. Yuan, J. and Antonietti, M., *Polymer* **2011**, *52*, 7, 1469-1482.
115. Paraknowitsch, J.P., Thomas, A., and Antonietti, M., *Journal of Materials Chemistry* **2010**, *20*, 32, 6746-6758.
116. Lee, J.S., Wang, X., Luo, H., Baker, G.A., and Dai, S., *Journal of the American Chemical Society* **2009**, *131*, 13, 4596-4597.
117. Wooster, T.J., Johanson, K.M., Fraser, K.J., MacFarlane, D.R., and Scott, J.L., *Green Chemistry* **2006**, *8*, 8, 691-696.
118. Thomas, A., *Angewandte Chemie International Edition* **2010**, *49*, 45, 8328-8344.
119. Kuhn, P., Antonietti, M., and Thomas, A., *Angewandte Chemie International Edition* **2008**, *47*, 18, 3450-3453.
120. Schneider, A., Weidmann, C., Suchomski, C., Sommer, H., Janek, J., and Brezesinski, T., *Chemistry of Materials* **2015**, *27*, 5, 1674-1683.
121. Yang, W., Fellinger, T.-P., and Antonietti, M., *Journal of the American Chemical Society* **2011**, *133*, 2, 206-209.
122. Antonietti, M., Kuang, D., Smarsly, B., and Zhou, Y., *Angewandte Chemie International Edition* **2004**, *43*, 38, 4988-4992.
123. Wang, X. and Dai, S., *Angewandte Chemie International Edition* **2010**, *49*, 37, 6664-6668.
124. Aloni, S.S., Perovic, M., Weitman, M., Cohen, R., Oschatz, M., and Mastai, Y., *Nanoscale Advances* **2019**, *1*, 12, 4981-4988.
125. Fuchs, I., Fechler, N., Antonietti, M., and Mastai, Y., *Angewandte Chemie International Edition* **2015**, *55*, 1, 408-412.
126. Gong, J., Antonietti, M., and Yuan, J., *Angewandte Chemie International Edition* **2017**, *56*, 26, 7557-7563.
127. Ranjbar Sahraie, N., Paraknowitsch, J.P., Göbel, C., Thomas, A., and Strasser, P., *Journal of the American Chemical Society* **2014**, *136*, 41, 14486-14497.
128. Li, X.-H. and Antonietti, M., *Chemical Society Reviews* **2013**, *42*, 16, 6593-6604.
129. Du, A., Sanvito, S., Li, Z., Wang, D., Jiao, Y., Liao, T., Sun, Q., Ng, Y.H., Zhu, Z., Amal, R., and Smith, S.C., *Journal of the American Chemical Society* **2012**, *134*, 9, 4393-4397.
130. Yao, Z., Postma, H.W.C., Balents, L., and Dekker, C., *Nature* **1999**, *402*, 6759, 273-276.

131. Fuhrer, M.S., Lim, A.K.L., Shih, L., Varadarajan, U., Zettl, A., and McEuen, P.L., *Physica E: Low-dimensional Systems and Nanostructures* **2000**, *6*, 1, 868-871.
132. Wehling, T.O., Novoselov, K.S., Morozov, S.V., Vdovin, E.E., Katsnelson, M.I., Geim, A.K., and Lichtenstein, A.I., *Nano Letters* **2008**, *8*, 1, 173-177.
133. Kahn, A., *Materials Horizons* **2016**, *3*, 1, 7-10.
134. Paulus, G.L.C., Wang, Q.H., Ulissi, Z.W., McNicholas, T.P., Vijayaraghavan, A., Shih, C.-J., Jin, Z., and Strano, M.S., *Small* **2013**, *9*, 11, 1954-1963.
135. Wang, Q., Yang, S.-W., Yang, Y., Chan-Park, M.B., and Chen, Y., *The Journal of Physical Chemistry Letters* **2011**, *2*, 9, 1009-1014.
136. Tuaev, X., Paraknowitsch, J.P., Illgen, R., Thomas, A., and Strasser, P., *Physical Chemistry Chemical Physics* **2012**, *14*, 18, 6444-6447.
137. Kuzmicz, D., Prescher, S., Polzer, F., Soll, S., Seitz, C., Antonietti, M., and Yuan, J., *Angewandte Chemie International Edition* **2014**, *53*, 4, 1062-1066.
138. Yan, R., Josef, E., Huang, H., Leus, K., Niederberger, M., Hofmann, J.P., Walczak, R., Antonietti, M., and Oschatz, M., *Advanced Functional Materials* **2019**, *29*, 26, 1902858.
139. Bender, H.L., *Chemisches Zentralblatt* **1921**, *2*, 14, 645.
140. Roduner, E., *Nanoscopic Materials: Size-Dependent Phenomena*. **2006**, The Royal Society of Chemistry: Cambridge, UK.
141. Terrones, H., Lv, R., Terrones, M., and Dresselhaus, M.S., *Reports on Progress in Physics* **2012**, *75*, 6, 062501.
142. Campisi, S., Chan-Thaw, C.E., and Villa, A., *Applied Sciences* **2018**, *8*, 7, 1159.
143. Antonietti, M. and Oschatz, M., *Advanced Materials* **2018**, *30*, 21.
144. Stakheev, A.Y. and Kustov, L.M., *Applied Catalysis A: General* **1999**, *188*, 1, 3-35.
145. Mavrikakis, M., Hammer, B., and Nørskov, J.K., *Physical Review Letters* **1998**, *81*, 13, 2819-2822.
146. Nilsson Pingel, T., Jørgensen, M., Yankovich, A.B., Grönbeck, H., and Olsson, E., *Nature Communications* **2018**, *9*, 1, 2722.
147. Adams, D.M., Brus, L., Chidsey, C.E.D., Creager, S., Creutz, C., Kagan, C.R., Kamat, P.V., Lieberman, M., Lindsay, S., Marcus, R.A., Metzger, R.M., Michel-Beyerle, M.E., Miller, J.R., Newton, M.D., Rolison, D.R., Sankey, O., Schanze, K.S., Yardley, J., and Zhu, X., *The Journal of Physical Chemistry B* **2003**, *107*, 28, 6668-6697.
148. Zhou, L. and Zachariah, M.R., *Chemical Physics Letters* **2012**, *525-526*, 77-81.
149. Skriver, H.L. and Rosengaard, N.M., *Physical Review B* **1992**, *46*, 11, 7157-7168.
150. Garg, R., Dutta, N.K., and Choudhury, N.R., *Nanomaterials* **2014**, *4*, 2, 267-300.
151. Qin, Q., Heil, T., Antonietti, M., and Oschatz, M., *Small Methods* **2018**, *2*, 12, 1800202.
152. Oschatz, M. and Antonietti, M., *Energy & Environmental Science* **2018**.
153. Hao, G.-P., Li, W.-C., Wang, S., Zhang, S., and Lu, A.-H., *Carbon* **2010**, *48*, 12, 3330-3339.
154. Li, L., Quinlivan, P.A., and Knappe, D.R.U., *Carbon* **2002**, *40*, 12, 2085-2100.
155. Tascón, J.M., *Novel carbon adsorbents*. **2012**, Elsevier: Amsterdam, Netherlands.
156. Pasteur, M.L., *Annales de chimie et de physique* **1848**, *24*, 442 – 459.
157. Stadler, A.-M. and Harrowfield, J., *Chemical Society Reviews* **2011**, *40*, 5, 2061-2108.
158. Podlech, J., *Cellular and Molecular Life Sciences CMLS* **2001**, *58*, 1, 44-60.

159. Kasprzyk-Hordern, B., *Chemical Society Reviews* **2010**, *39*, 11, 4466-4503.
160. Cahn, R.S., Ingold, C., and Prelog, V., *Angewandte Chemie International Edition* **1966**, *5*, 4, 385-415.
161. De Camp, W.H., *Chirality* **1989**, *1*, 1, 2-6.
162. Gibb, B.C., *Nature Chemistry* **2012**, *4*, 4, 237-238.
163. Ma, W., Xu, L., de Moura, A.F., Wu, X., Kuang, H., Xu, C., and Kotov, N.A., *Chemical Reviews* **2017**, *117*, 12, 8041-8093.
164. Liu, M., Zhang, L., and Wang, T., *Chemical Reviews* **2015**, *115*, 15, 7304-7397.
165. Zaera, F., *Chemical Society Reviews* **2017**, *46*, 23, 7374-7398.
166. Scriba, G.K.E., *Journal of Chromatography A* **2016**, *1467*, 56-78.
167. Xie, S.-M. and Yuan, L.-M., *Journal of Separation Science* **2017**, *40*, 1, 124-137.
168. Che, S., Liu, Z., Ohsuna, T., Sakamoto, K., Terasaki, O., and Tatsumi, T., *Nature* **2004**, *429*, 6989, 281-284.
169. Stein, A., Melde, B.J., and Schroden, R.C., *Advanced Materials* **2000**, *12*, 19, 1403-1419.
170. Ma, L.Q., Abney, C., and Lin, W.B., *Chemical Society Reviews* **2009**, *38*, 5, 1248-1256.
171. Padmanaban, M., Müller, P., Lieder, C., Gedrich, K., Grünker, R., Bon, V., Senkovska, I., Baumgärtner, S., Opelt, S., Paasch, S., Brunner, E., Glorius, F., Klemm, E., and Kaskel, S., *Chemical Communications* **2011**, *47*, 44, 12089-12091.
172. Shen, J. and Okamoto, Y., *Chemical Reviews* **2016**, *116*, 3, 1094-1138.
173. Ibanez, J.G., Rincón, M.E., Gutierrez-Granados, S., Chahma, M.h., Jaramillo-Quintero, O.A., and Frontana-Uribe, B.A., *Chemical Reviews* **2018**, *118*, 9, 4731-4816.
174. Jenkins, S.J., *Chirality at Solid Surfaces*. **2018**, John Wiley & Sons, Ltd.: Hoboken, USA.
175. Guo, P. and Wong, K.-Y., *Electrochemistry Communications* **1999**, *1*, 11, 559-563.
176. Tiwari, J.N., Vij, V., Kemp, K.C., and Kim, K.S., *ACS Nano* **2016**, *10*, 1, 46-80.
177. Jáč, P. and Scriba, G.K.E., *Journal of Separation Science* **2013**, *36*, 1, 52-74.
178. Nishitani, S., Sekiya, R., and Haino, T., *Angewandte Chemie International Edition* **2020**, *59*, 2, 669-673.
179. Filippone, S., Maroto, E.E., Martín-Domenech, Á., Suarez, M., and Martín, N., *Nature Chemistry* **2009**, *1*, 7, 578-582.
180. Karousis, N., Tagmatarchis, N., and Tasis, D., *Chemical Reviews* **2010**, *110*, 9, 5366-5397.
181. Ding, J. and Armstrong, D.W., *Chirality* **2005**, *17*, 5, 281-292.
182. Kapnissi-Christodoulou, C.P., Stavrou, I.J., and Mavroudi, M.C., *Journal of Chromatography A* **2014**, *1363*, 2-10.
183. Boudart, M., *Kinetics of Chemical Processes*. **1991**, Butterworth-Heinemann: Oxford, UK.
184. Thomas, J.M. and Zamaraev, K., *Perspectives in catalysis*. **1991**, Blackwell Scientific Publications: Oxford, Boston, USA.
185. Thomas, J.M. and Williams, R.J.P., *Philosophical Transactions of the Royal Society A* **2005**, *363*, 765–791.
186. Deutschmann, O., Knözinger, H., Kochloefl, K. and Turek, T., *Heterogeneous Catalysis and Solid Catalysts*, in *Ullmann's Encyclopedia of Industrial Chemistry*. **2009**, Wiley - VCH: Weinheim, Germany.

187. Ma, Z. and Dai, S., *Stabilizing Gold Nanoparticles by Solid Supports*, in *Heterogeneous Gold Catalysts and Catalysis*. **2014**, The Royal Society of Chemistry: Cambridge, UK. p. 1-26.
188. White, R.J., Luque, R., Budarin, V.L., Clark, J.H., and Macquarrie, D.J., *Chemical Society Reviews* **2009**, *38*, 2, 481-494.
189. van Deelen, T.W., Hernández Mejía, C., and de Jong, K.P., *Nature Catalysis* **2019**, *2*, 11, 955-970.
190. Roduner, E., *Chemical Society Reviews* **2014**, *43*, 24, 8226-8239.
191. Roduner, E., *Chemical Society Reviews* **2006**, *35*, 7, 583-592.
192. Navalon, S., Dhakshinamoorthy, A., Alvaro, M., Antonietti, M., and García, H., *Chemical Society Reviews* **2017**, *46*, 15, 4501-4529.
193. Su, D.S., Perathoner, S., and Centi, G., *Chemical Reviews* **2013**, *113*, 8, 5782-5816.
194. Climent, M.J., Corma, A., and Iborra, S., *Green Chemistry* **2011**, *13*, 3, 520-540.
195. Song, J., Fan, H., Ma, J., and Han, B., *Green Chemistry* **2013**, *15*, 10, 2619-2635.
196. Singh, O.V. and Kumar, R., *Applied Microbiology and Biotechnology* **2007**, *75*, 4, 713-722.
197. Dimitratos, N., Lopez-Sanchez, J.A., and Hutchings, G.J., *Chemical Science* **2012**, *3*, 1, 20-44.
198. Mallat, T. and Baiker, A., *Chemical Reviews* **2004**, *104*, 6, 3037-3058.
199. Cañete-Rodríguez, A.M., Santos-Dueñas, I.M., Jiménez-Hornero, J.E., Ehrenreich, A., Liebl, W., and García-García, I., *Process Biochemistry* **2016**, *51*, 12, 1891-1903.
200. Savas Anastassiadis, I.G.M., *Recent Patents on Biotechnology* **2007**, *1*, 2, 167-180.
201. Kamide, K., *Cellulose and Cellulose Derivatives*. **2005**, Elsevier Science.
202. Besson, M., Lahmer, F., Gallezot, P., Fuertes, P., and Fleche, G., *Journal of Catalysis* **1995**, *152*, 1, 116-121.
203. Wenkin, M., Ruiz, P., Delmon, B., and Devillers, M., *Journal of Molecular Catalysis A: Chemical* **2002**, *180*, 1, 141-159.
204. Biella, S., Prati, L., and Rossi, M., *Journal of Catalysis* **2002**, *206*, 2, 242-247.
205. Haruta, M., *The Chemical Record* **2003**, *3*, 2, 75-87.
206. Hutchings, G.J., *ACS Central Science* **2018**, *4*, 9, 1095-1101.
207. Liu, C., Zhang, J., Huang, J., Zhang, C., Hong, F., Zhou, Y., Li, G., and Haruta, M., *ChemSusChem* **2017**, *10*, 9, 1976-1980.
208. Okatsu, H., Kinoshita, N., Akita, T., Ishida, T., and Haruta, M., *Applied Catalysis A: General* **2009**, *369*, 1, 8-14.
209. Ma, C., Xue, W., Li, J., Xing, W., and Hao, Z., *Green Chemistry* **2013**, *15*, 4, 1035-1041.
210. Qi, P., Chen, S., Chen, J., Zheng, J., Zheng, X., and Yuan, Y., *ACS Catalysis* **2015**, *5*, 4, 2659-2670.
211. Comotti, M., Pina, C.D., Matarrese, R., Rossi, M., and Siani, A., *Applied Catalysis A: General* **2005**, *291*, 1, 204-209.
212. Bianchi, C., Biella, S., Gervasini, A., Prati, L., and Rossi, M., *Catalysis Letters* **2003**, *85*, 91-96.
213. Önal, Y., Schimpf, S., and Claus, P., *Journal of Catalysis* **2004**, *223*, 1, 122-133.
214. Prüße, U., Heidinger, S., and Baatz, C., *Landbauforschung vTI Agriculture and Forestry Research* **2011**, *2011*, 261-272.
215. Davis, S.E., Ide, M.S., and Davis, R.J., *Green Chemistry* **2013**, *15*, 1, 17-45.
216. Pina, C.D., Falletta, E., and Rossi, M., *Chemical Society Reviews* **2012**, *41*, 1, 350-369.

217. Cattaneo, S., Stucchi, M., Villa, A., and Prati, L., *ChemCatChem* **2019**, *11*, 1, 309-323.
218. Zope, B.N., Hibbitts, D.D., Neurock, M., and Davis, R.J., *Science* **2010**, *330*, 6000, 74-78.
219. Perovic, M., Aloni, S.S., Mastai, Y., and Oschatz, M., *Carbon* **2020**, *170*, 550 – 557.
220. Rouquerol, F., Rouquerol, J., Sing, K.S.W., Maurin, G., and Llewellyn, P., *Adsorption by Powders and Porous Solids,* Second Edition. **2014**, Academic Press: Oxford, UK.
221. Ariga, K., Vinu, A., Yamauchi, Y., Ji, Q.M., and Hill, J.P., *Bulletin of the Chemical Society of Japan* **2012**, *85*, 1, 1-32.
222. Guo, Z., Wang, J., Qin, F., Ge, L., Li, Z., and Shen, W., *ACS Sustainable Chemistry & Engineering* **2020**, *8*, 8, 3401-3411.
223. Silva, S.G., Rodríguez-Borges, J.E., Marques, E.F., and do Vale, M.L.C., *Tetrahedron* **2009**, *65*, 21, 4156-4164.
224. Sarkisov, L., Centineo, A., and Brandani, S., *Carbon* **2017**, *118*, 127-138.
225. Liu, L., Tan, S., Horikawa, T., Do, D.D., Nicholson, D., and Liu, J., *Advances in Colloid and Interface Science* **2017**, *250*, 64-78.
226. Velasco, L.F., Guillet-Nicolas, R., Dobos, G., Thommes, M., and Lodewyckx, P., *Carbon* **2016**, *96*, 753-758.
227. Yan, R., Heil, T., Presser, V., Walczak, R., Antonietti, M., and Oschatz, M., *Advanced Sustainable Systems* **2017**, *2*, 1700128.
228. Shval, A. and Mastai, Y., *Chemical Communications* **2011**, *47*, 20, 5735-5737.
229. Rademacher, J.T., Kanakarajan, K., and Czarnik, A.W., *Synthesis (Stuttgart)* **1994**, 4, 378-380.
230. Oschatz, M., Pré, P., Dörfler, S., Nickel, W., Beaunier, P., Rouzaud, J.-N., Fischer, C., Brunner, E., and Kaskel, S., *Carbon* **2016**, *105*, 314-322.
231. Casiraghi, C., Ferrari, A.C., and Robertson, J., *Physical Review B* **2005**, *72*, 8, 085401.
232. Ferrari, A.C. and Robertson, J., *Physical Review B* **2000**, *61*, 20, 14095-14107.
233. Perovic, M., Tarakina, N.V., Hofmann, J.P., and Oschatz, M., *ACS Applied Nano Materials* **2020**, *3*, 8, 7695 – 7703.
234. Ishida, T., Murayama, T., Taketoshi, A., and Haruta, M., *Chemical Reviews* **2020**, *120*, 2, 464-525.
235. Berry, R.S., *Phases and Phase Changes of Small Systems*, in *Theory of Atomic and Molecular Clusters: With a Glimpse at Experiments*, Jellinek, Editor. **1999**, Springer: Berlin, Heidelberg, Germany. p. 1-26.
236. Goettmann, F. and Sanchez, C., *Journal of Materials Chemistry* **2007**, *17*, 1, 24-30.
237. Striolo, A., *Nano-confined water*, in *Theoretical and Computational Chemistry*, Balbuena and Seminario, Editors. **2007**, Elsevier: Amsterdam, Netherlands. p. 245-274.
238. Bellissent‐Funel, M.C., Sridi‐Dorbez, R., and Bosio, L., *The Journal of Chemical Physics* **1996**, *104*, 24, 10023-10029.
239. Evans, R., Marconi, U.M.B., and Tarazona, P., *The Journal of Chemical Physics* **1986**, *84*, 4, 2376-2399.
240. Radhakrishnan, R., Gubbins, K.E., and Sliwinska-Bartkowiak, M., *The Journal of Chemical Physics* **2002**, *116*, 3, 1147-1155.
241. Giaya, A. and Thompson, R.W., *The Journal of Chemical Physics* **2002**, *117*, 7, 3464-3475.

242. Pera-Titus, M., El-Chahal, R., Rakotovao, V., Daniel, C., Miachon, S., and Dalmon, J.-A., *ChemPhysChem* **2009**, *10*, 12, 2082-2089.
243. Luzar, A. and Bratko, D., *The Journal of Physical Chemistry B* **2005**, *109*, 47, 22545-22552.
244. Miachon, S., Syakaev, V.V., Rakhmatullin, A., Pera-Titus, M., Caldarelli, S., and Dalmon, J.-A., *ChemPhysChem* **2008**, *9*, 1, 78-82.
245. Lidon, P., Marker, S.C., Wilson, J.J., Williams, R.M., Zipfel, W.R., and Stroock, A.D., *Langmuir* **2018**, *34*, 40, 12017-12024.
246. Gladysz, J.A., Curran, D.P., and Horváth, I.T., *Handbook of Fluorous Chemistry*. **2004**, Wiley - VCH: Weinheim, Germany.
247. Horváth, I.T., *Accounts of Chemical Research* **1998**, *31*, 10, 641-650.
248. Riess, J.G., *Artificial Cells, Blood Substitutes, and Biotechnology* **2005**, *33*, 1, 47-63.
249. Riess, J.G. and Le Blanc, M., *Angewandte Chemie International Edition* **1978**, *17*, 9, 621-634.
250. Clark, L.C. and Gollan, F., *Science* **1966**, *152*, 3730, 1755-1756.
251. Lowe, K.C., *Artificial Cells, Blood Substitutes, and Biotechnology* **2000**, *28*, 1, 25-38.
252. Dias, A.M.A., Freire, M., Coutinho, J.A.P., and Marrucho, I.M., *Fluid Phase Equilibria* **2004**, *222-223*, 325-330.
253. Zeininger, L., Stiegler, L.M.S., Portilla, L., Halik, M., and Hirsch, A., *ChemistryOpen* **2018**, *7*, 4, 282-287.
254. Ku, K.H., Li, J., Yoshinaga, K., and Swager, T.M., *Advanced Materials* **2019**, *31*, 51, 1905569.
255. Wu, J. and Ma, G.-H., *Small* **2016**, *12*, 34, 4633-4648.
256. Goodarzi, F. and Zendehboudi, S., *The Canadian Journal of Chemical Engineering* **2019**, *97*, 1, 281-309.
257. Yang, Y., Fang, Z., Chen, X., Zhang, W., Xie, Y., Chen, Y., Liu, Z., and Yuan, W., *Frontiers in Pharmacology* **2017**, *8*, 287.
258. Jeon, I., Peeks, M.D., Savagatrup, S., Zeininger, L., Chang, S., Thomas, G., Wang, W., and Swager, T.M., *Advanced Materials* **2019**, *31*, 21, 1900438.
259. Soubeyrand-Lenoir, E., Vagner, C., Yoon, J.W., Bazin, P., Ragon, F., Hwang, Y.K., Serre, C., Chang, J.-S., and Llewellyn, P.L., *Journal of the American Chemical Society* **2012**, *134*, 24, 10174-10181.
260. Turkevich, J., Stevenson, P.C., and Hillier, J., *Discussions of the Faraday Society* **1951**, *11*, 0, 55-75.
261. Casavola, M., Hermannsdörfer, J., de Jonge, N., Dugulan, A.I., and de Jong, K.P., *Advanced Functional Materials* **2015**, *25*, 33, 5309-5319.
262. Lama, S.M.G., Schmidt, J., Malik, A., Walczak, R., Silva, D.V., Völkel, A., and Oschatz, M., *ChemCatChem* **2018**, *10*, 2458.
263. Galeano, C., Meier, J.C., Peinecke, V., Bongard, H., Katsounaros, I., Topalov, A.A., Lu, A., Mayrhofer, K.J.J., and Schüth, F., *Journal of the American Chemical Society* **2012**, *134*, 50, 20457-20465.
264. Perazzolo, V., Brandiele, R., Durante, C., Zerbetto, M., Causin, V., Rizzi, G.A., Cerri, I., Granozzi, G., and Gennaro, A., *ACS Catalysis* **2018**, *8*, 2, 1122-1137.
265. Casaletto, M.P., Longo, A., Martorana, A., Prestianni, A., and Venezia, A.M., *Surface and Interface Analysis* **2006**, *38*, 4, 215-218.

266. Ishida, T., Kinoshita, N., Okatsu, H., Akita, T., Takei, T., and Haruta, M., *Angewandte Chemie - International Edition* **2008**, *47*, 48, 9265-9268.
267. Comotti, M., Pina, C.D., Matarrese, R., and Rossi, M., *Angewandte Chemie International Edition* **2004**, *43*, 43, 5812-5815.
268. Oliver-Meseguer, J., Cabrero-Antonino, J.R., Domínguez, I., Leyva-Pérez, A., and Corma, A., *Science* **2012**, *338*, 6113, 1452-1455.
269. Xiong, H., Jewell, L.L., and Coville, N.J., *ACS Catalysis* **2015**, *5*, 4, 2640-2658.
270. Inkson, B.J., *Scanning electron microscopy (SEM) and transmission electron microscopy (TEM) for materials characterization*, in *Materials Characterization Using Nondestructive Evaluation (NDE) Methods*, Hübschen, et al., Editors. **2016**, Woodhead Publishing: Cambridge, UK. p. 17-43.
271. Yao, N. and Wang, Z.L., *Handbook of microscopy for nanotechnology*. **2005**, Springer US: New York, USA.
272. Iwashita, N., *X-ray Powder Diffraction*, in *Materials science and engineering of carbon: characterization*, Inagaki and Kang, Editors. **2016**, Butterworth-Heinemann: Oxford, UK.
273. Raman, C.V. and Krishnan, K.S., *Nature* **1928**, *121*, 3048, 501-502.
274. Schrader, B., *Infrared and Raman spectroscopy: methods and applications*. **2008**, John Wiley & Sons, Inc.: Hoboken, NJ, USA.
275. Kumar, J., *Photoelectron Spectroscopy: Fundamental Principles and Applications*, in *Handbook of Materials Characterization*, Sharma, Editor. **2018**, Springer International Publishing: Cham, Switzerland. p. 435-495.
276. Thompson, M., *Handbook of Inductively Coupled Plasma Spectrometry*. **1989**, Springer US: New York, USA.
277. de Bruin, T.J.M., Marcelis, A.T.M., Zuilhof, H., and Sudhölter, E.J.R., *Langmuir* **2000**, *16*, 22, 8270-8275.
278. Jelesarov, I. and Bosshard, H.R., *Journal of Molecular Recognition* **1999**, *12*, 1, 3-18.
279. Leavitt, S. and Freire, E., *Current Opinion in Structural Biology* **2001**, *11*, 5, 560-566.
280. Wiseman, T., Williston, S., Brandts, J.F., and Lin, L.-N., *Analytical Biochemistry* **1989**, *179*, 1, 131-137.
281. Aue, W.P., Bartholdi, E., and Ernst, R.R., *The Journal of Chemical Physics* **1976**, *64*, 5, 2229-2246.
282. Armstrong, R.D., Hirayama, J., Knight, D.W., and Hutchings, G.J., *ACS Catalysis* **2019**, *9*, 1, 325-335.
283. Perovic, M., Zeininger, L., and Oschatz, M., *ChemCatChem* **2020**, DOI: 10.1002/cctc.202001590.

8. Appendix

8.1. List of Abbreviations

(Au)NP	(gold) nanoparticles
(C)IL	(chiral) ionic liquids
(HR)TEM	(high-resolution) transmission electron microscopy
AC	activated carbon
at.%	atomic percentage
B.E.	binding energy
BET	Brunauer–Emmett–Teller method
BJH	Barrett-Joyner-Halenda method
CDC	carbide-derived carbons
CMK	carbon mesostructured by KAIST
CNT	carbon nanotubes
EA	elemental analysis
EDX	energy dispersive X-ray spectroscopy
EISA	(solvent) evaporation induced self-assembly
eV	electronvolt
FC-72	Fluorinert™ liquid (tetradecafluorohexane)
FWHM	full width at half maximum (of the peak)
HAT-CN	hexaazatriphenylene-hexacarbonitrile
HC	hydrocarbon
HMBC	heteronuclear multiple-bond correlation
HSQC	heteronuclear single-quantum correlation
ICP-OES	inductively coupled plasma – optical emission spectrometry
ITC	isothermal titration calorimetry
IUPAC	International Union of Pure and Applied Chemistry
K.E.	kinetic energy
KAIST	Korea Advanced Institute of Science and Technology
KIT	KAIST silica material
MCM	Mobil Composition of Matter
MOF	metal-organic framework

µm	micrometer
MPIKG	Max-Planck-Institut für Kolloid- und Grenzflächenforschung
MTY	metal time yield
NLDFT	nonlocal density functional theory
nm	nanometer
NMR	nuclear magnetic resonance
PF	phloroglucinol–formaldehyde
PFC	perfluorocarbon
Phe	phenylalanine
Pro-TFSI	N,N-dimethyl-Proline methyl ester bis(trifluoromethylsulfonyl)imide
PS-*b*-PEO	polystyrene-b-poly(ethylene oxide)
PSD	pore size distribution
QSDFT	quenched-solid density functional theory
RF	resorcinol–formaldehyde
SBA	Santa Barbara Amorphous type material
SDA	structure-directing agent
SEM	scanning electron microscopy
SSA	specific surface area
STC	salt-templated carbon
TEOS	tetraethyl orthosilicate
TGA(-MS)	thermogravimetric analysis (coupled with mass spectrometry)
Tyr-BF_4	N,N,N-trimethyl-Tyrosine methyl ester tetrafluoroborate
V_{meso}	mesopore volume
V_{micro}	micropore volume
vol.%	volume percentage
V_t	total pore volume
wt %	weight percentage
XPS	X-ray photoelectron spectroscopy
XRD	X-ray diffraction

8.2. Applied Methods

Gas/Vapor Physisorption Measurements

N_2 Physisorption

The term "adsorption" is generally defined as the enrichment of one or more components at the interface between a solid (the *adsorbent*) and a fluid. The fluid in the adsorbed state is known as the *adsorbate*, while the *adsorptive* is the same component in the fluid phase. *Physisorption* involves attractive dispersion forces, short-range repulsive forces, and specific molecular interactions, whereas *chemisorption* leads to the formation of covalent chemical bonds and has thus a higher enthalpy. Physisorption is a widely used analytical tool for the characterization of the texture of porous solids and powders. Measurements of N_2 and Ar adsorption at cryogenic temperatures (−196 °C and −186 °C, respectively) are primarily used for surface area and pore size characterization. A physisorption isotherm expresses the amount of adsorbed gas on the adsorbent with respect to the relative pressure ($p\ p_0^{-1}$), where p is the absolute pressure and p_0 is the saturation pressure of the adsorptive at a given temperature. The isotherms obtained in this way can be classified into eight types, according to the latest IUPAC recommendations (**Figure 8.1**).[28]

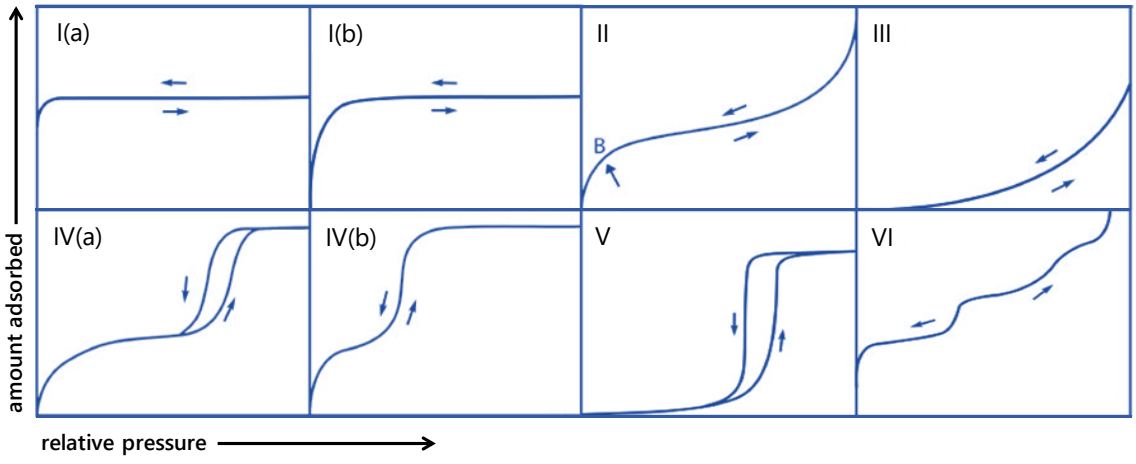

Figure 8.1. *Classification of physisorption isotherms. Adapted with permission.[28] Copyright 2015, De Gruyter.*

The type I isotherms are characteristic for microporous materials, where the filling of ultramicropores (approx. width < 0.7 nm) and supermicropores (wide micropores, 0.7-

2.0 nm) corresponds to type I(a) and I(b) isotherms, respectively. A steep uptake at low relative pressure is a consequence of enhanced solid–gas interactions in micropores. The type II isotherm is given by non-porous or macroporous materials, due to unrestricted monolayer-multilayer adsorption up to high relative pressures. The monolayer is complete if the knee (point B in **Figure 8.1**) is sharp, and a more gradual knee is a sign of simultaneous monolayer and multilayer formation. Type III isotherm indicates weak adsorbent-adsorbate interactions, where the adsorption is based on the clustering of adsorbate around the favorable sites on the surface of the adsorbent. Isotherms of type IV are characteristic for mesoporous solids. Type IV(a) isotherm contains a hysteresis that is a consequence of capillary condensation in the pores wider than ~ 4 nm for N_2 physisorption at 77 K (the relation between pore width and capillary condensation depends on the adsorption system and temperature). Permanent hysteresis is a result of adsorption metastability, because of the vapor–liquid phase transition that is delayed because it involves nucleation. In contrast, desorption does not involve nucleation, and thermodynamic equilibrium is accomplished on the desorption branch. Adsorbents with smaller mesopores give isotherm of type IV(b). Type V isotherms are obtained when the adsorbate is not entirely wetting the surface of the adsorbent, similarly to type III isotherms. This results in small amounts of adsorbed gas at low relative pressures, followed by pore filling at higher p p_0^{-1}. The type VI isotherm is rarely observed and is characteristic for layer-by-layer formation on uniform nonporous surfaces.

The evaluation of the surface area of porous materials is most often accomplished by the Brunauer–Emmett–Teller (BET) method, by transforming the physisorption isotherm into the "BET plot", and by application of the BET equation to it (Eq. 8.1).

$$\frac{p/p_0}{V_{ads}(1-p/p_0)} = \frac{1}{V_{mono}C} + \frac{C-1}{V_{mono}C}(p/p_0) \qquad (8.1)$$

V_{ads} represents the total adsorbed volume, V_{mono} the monolayer volume, and C the adsorption constant. Deriving the V_{mono} is simple if the relation is linear, which is usually

restricted to a part of the isotherm within the p p_0^{-1} range of ~ 0.05–0.3. Determination of specific BET surface area (SSA_{BET}) in units $m^2\ g^{-1}$ is further calculated through Equation 8.2.

$$SSA_{BET} = V_{mono}\sigma_{N_2}N_A/m \quad (8.2)$$

σ represents the cross-section of N_2 molecule (equals to 0.162 nm^2), N_A is the Avogadro constant, and m the mass of adsorbent.

Mesopore size analysis (i.e., Barrett-Joyner-Halenda (BJH) method) is based on the Kelvin equation (Eq. 8.3), which correlates the relative pressure at which the pore condensation occurs in a cylindrical pore and the radius r of the meniscus of the condensed liquid in the pore.

$$ln(p/p_0) = -2\gamma V_m cos\varphi/rRT \quad (8.3)$$

γ represents the surface tension of the bulk fluid of the V_m ideal gas volume. φ is the wetting angle, R the ideal gas constant, and T the temperature. However, this method is limited to pores of cylindrical shapes above the diameter of 2.5 nm, which results in an underestimated pore size for narrow mesopores. These limitations can be overcome by applying the methods both micro- and mesopores, based on density functional theory (DFT).[220]

Before all of the physisorption measurements, the samples were outgassed under vacuum at 150 °C for 20 h. N_2 physisorption experiments were performed at −196 °C on a Quadrasorb apparatus (Quantachrome Instruments, USA). SSAs of the materials are calculated by using the multipoint BET model in the relative pressure range 0.05−0.2. The total pore volumes (V_t) were determined at p p_0^{-1} = 0.99. The pore size distributions are calculated by using the quenched solid DFT (QSDFT) method for nitrogen on carbon with slit/cylindrical/spherical pores at −196 °C, adsorption branch kernel, integrated into the QuadraWin 5.11 analysis software (Quantachrome). Micropore volumes (V_{micro}) were calculated by using the DFT method from the cumulative pore volumes at a diameter of 2 nm.

CO_2 Physisorption

The cryogenic temperatures of physisorption measurements with N_2 or Ar as test gases have the disadvantage of kinetic restrictions and diffusion issues. CO_2 physisorption at 0 °C is a useful alternative for the analysis of narrow micropores due to its high saturation pressure of 26141 torr. On the other side, it has to be considered that the CO_2 molecule has a quadrupole moment and interacts with polar functionalities in adsorbents, thus the pore size analysis with this test gas on such materials can be misleading depending on the applied model.

CO_2 physisorption experiments were carried out at 0 °C on the Quadrasorb apparatus to investigate the pores with a diameter smaller than 1.5 nm. Corresponding PSDs were calculated by the non-local DFT (NLDFT) method for CO_2 adsorbed on carbon at 0 °C.

Vapor Adsorption

The water molecule has a small kinetic diameter of 0.265 nm (in comparison to 0.364 nm for N_2, and 0.330 nm for CO_2) which enables its diffusion into small pores, but at the same time, it expresses specific interactions of higher enthalpy with polar surfaces due to its high dipole moment. It can, therefore, provide information about surface properties and hydrophilicity of the adsorbent, and in combination with N_2 or Ar adsorption about pore structure of the materials. Characterization of porous chiral carbons for chiral recognition was performed by physisorption measurements using (S)-(+)-2-Butanol or (R)-(–)-2-Butanol at 25 °C. At this temperature, the saturation pressure of 2-Butanol is 18.3 torr.[225-226]

Water and 2-Butanol physisorption measurements were performed at 25 °C (sample weight ~ 50 mg) on a Quantachrome Autosorb IQ apparatus.

Electron Microscopy

Electron microscopy methods are based on interactions between an electron beam and a sample in a vacuum. Electrons that are generated in the electron gun are further accelerated by an electromagnetic field and focused onto the sample through a series of electromagnetic lenses. Electrons accelerated onto the sample result in different types of interactions with the atoms (**Figure 8.2**).

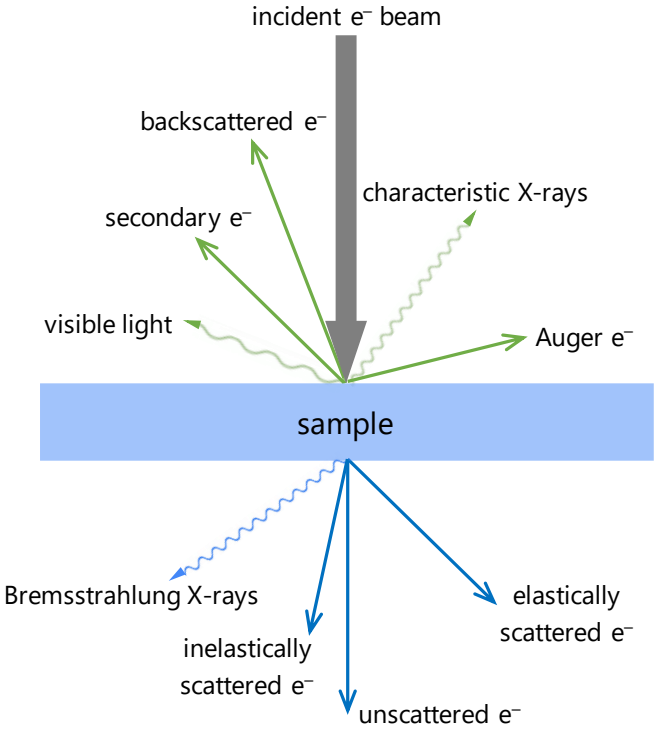

Figure 8.2. *Types of interactions between the electron beam and a sample.*

Scanning Electron Microscopy with Energy Dispersive X-ray Spectroscopy

SEM uses secondary and primary backscattered electrons for imaging of the specimen surface. Secondary electrons are important for analysis of the morphology and topography of the samples because they are low in energy and can be emitted only if they are generated close to the surface. Backscattered electrons are emitted from deeper regions due to their higher energy, in quantities that depend on the atomic number of the element. They are creating contrast in the composition of the sample that makes heavier atoms to appear brighter in the resulting image.

When an electron from an inner shell is ejected upon interaction with the incident beam, the vacancy is replaced by an electron from a higher shell. This process induces the generation of element-specific X-rays, that are utilized for qualitative and quantitative analysis with Energy Dispersive X-ray (EDX) Spectroscopy.[270]

SEM was carried out on a LEO 1550-Gemini microscope operating at 3.00 kV. The samples were coated with a few nm thin platinum layer via sputtering to increase the surface conductivity. EDX investigations were conducted using a Link ISIS-300 system (Oxford Microanalysis Group) equipped with a Si(Li) detector and an energy resolution of 133 eV. The measurements were performed by Heike Runge and Rona Pitschke (MPIKG).

(High-resolution) Transmission Electron Microscopy

Image formation in TEM is based on electrons that are transmitted through a very thin sample. The resolution is adjusted by the acceleration voltage, where higher voltage generally results in higher resolution, but the achievable resolution is limited by the electromagnetic lenses. Several modes of measurement use different types of electrons that are passed through the sample. Bright-field imaging is mainly formed by unscattered electrons that are sensitive to sample density, creating images in which lighter regions correspond to lighter elements and/or thinner samples, and elements with a higher atomic number and/or thicker samples appear darker. On the other hand, an inversed bright-field image is formed by using elastically scattered electrons, in a dark-field mode. Elastically scattered electrons can also be used for creating diffraction patterns for the characterization of the crystalline samples. Further information that can be derived from TEM is electron-energy loss spectroscopy and energy-filtered TEM, both using inelastically scattered electrons, as well as EDX spectroscopy.[271]

HRTEM in Chapter 5.1 was performed by using a JEOL ARM 200F microscope operated at 200 kV. TEM in the remaining Chapters was performed on a Zeiss912 Omega operated at 120 kV. Prior to analysis, the samples were dispersed in ethanol and sonicated for 5 min. Several droplets of dispersions were cast onto TEM copper grids with a holey carbon film and dried at room temperature. The HRTEM measurements were carried out by Dr.

Nadezda V. Tarakina and Bolortuya Badamdorj, and TEM by Rona Pitschke and Heike Runge (MPIKG).

Powder X-ray Diffraction

PXRD is a structural characterization method for the analysis of powders. X-rays are produced in an X-ray tube, upon bombardment of a solid target (commonly Cu or Mo) with a focused electron beam. These monochromatic X-rays are further directed to the sample, where elastic and inelastic interactions take place. If the wavelength (λ) of incident radiation is in the range of the distances in the lattice of the material, diffraction occurs. Atomic distances within crystal lattice are similar to the wavelength of X-rays, thus crystalline materials represent a diffraction lattice in XRD measurement. For parallel planes of atoms, with a distance between the planes d_{hkl}, constructive interference only occurs when Bragg's law (Eq. 8.4) is satisfied.

$$n\lambda = 2d_{hkl}sin\theta \tag{8.4}$$

Where n is a positive integer. Bragg's law provides a simplistic model for conditions required for diffraction, relating wavelength λ of incident X-ray with diffraction angle θ and the distance between the planes d_{hkl}. Since the orientation in the powdered sample is randomly arranged, it is necessary to measure diffraction through a wide range of 2θ to cover various possible lattice directions.[272]

PXRD patterns were recorded on a Bruker D8 Advance diffractometer that uses the Bragg-Brentano geometry, in which the diffraction vector (the vector that bisects the angle between the incident and diffracted beam) is normal to the surface of the sample. The instrument is equipped with a scintillation counter detector using Cu Kα radiation (λ = 0.1518 nm) in the 2θ range 3°–90° with a step size of 0.02° and counting time of 1 s per step.

Raman Spectroscopy

Raman spectroscopy is a vibrational spectroscopy technique that can be used for the characterization of crystalline, nanocrystalline, and amorphous carbons. When a sample is

irradiated with a laser beam of energy E_L and a frequency ν_L ($E_L = h\nu_L$, where h is the Planck constant), the light is scattered (**Figure 8.3a**). If the reflection beam has the same frequency, it is elastically scattered, and this process is known as Rayleigh scattering ($\nu_L = \nu_R$). When the light is inelastically scattered, the Raman effect occurs. The frequency shift ($\nu_{0\to1}$) is related to a vibration mode of the substance, and from it, the Raman shift (cm^{-1}) is derived ($\nu_{0\to1}/c$, where c is the speed of light). The scattered light with $\nu_L - \nu_{0\to1}$ is called Stokes scattering and that with $\nu_L + \nu_{0\to1}$ is called Anti-Stokes scattering. The Stokes scattering is usually used for Raman measurements of the carbon materials.[273-274]

Raman spectra in the present thesis were recorded by using a Witec Raman microscope operating with an objective (Nikon, 10×/0.25, ∞/-WD 6.1) and an excitation wavelength of 532 nm with an intensity of 3.5 mW and accumulations of 100 scans with 10 s per scan. Deconvolution of the spectra was performed by assuming mixed Gaussian/Lorentzian peaks to describe both the main D- and G-bands and the two bands with lower intensity, A and D^2, positioned at 1500 and 1170 cm^{-1}, respectively. The fit was performed by using OriginPro 2019. The parameters retained were the full width at half-maximum (FWHM) of the D-band and the ratio of the peak heights (I_D/I_G). The measurements were performed by Dr. Ralf Walczak (Chapter 5.1) and M.Sc. Wuyong Zhang (Chapter 4.2) (MPIKG).

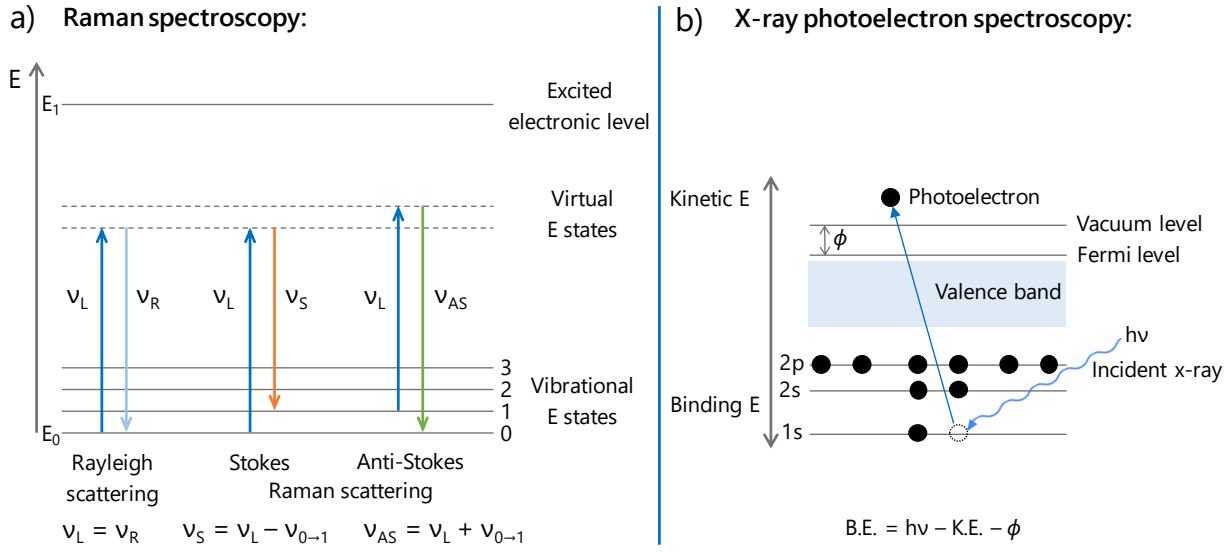

Figure 8.3. *a) Molecular energy level diagram with involved processes in Raman measurements: Rayleigh, Stokes Raman, and Anti-Stokes Raman scattering, and b) schematic energy level diagram for photoelectron emission process, which is the fundamental principle of XPS measurements.*

X-ray Photoelectron Spectroscopy

XPS is a surface characterization technique that provides information on elemental identification and chemical state of the elements, their relative composition, as well as the structure of the valence band. The sampling depth is typically between 3 and a maximum of 10 nm. When a sample is irradiated with x-rays of energy hν, and the electron from the core level is ejected with kinetic energy (K.E.), this phenomenon is known as a photoelectric effect (**Figure 8.3b**). This is described by the Einstein equation (Eq. 8.5).

$$K.E. = h\nu - B.E. - \phi \tag{8.5}$$

Where ϕ is a work function, and B.E. binding energy of the ejected electron. Binding energy is characteristic of each element, which enables qualitative and quantitative analysis. Moreover, the fine structure of the element signal depends also on its surroundings, which provides information about specific chemical binding motifs.[275]

XPS was performed on a Thermo Scientific K-Alpha spectrometer equipped with an Al Kα anode (hν = 1486.7 eV; 400 μm spot size). Elemental compositions were determined by using survey scans over a range of 1350−0 eV with a step size of 1.0 eV and a pass energy of 200 eV. Quantitative characterization of the presence of C, O, and Au was accomplished with high-resolution XPS region scans with a step size of 0.1 eV and a pass energy of 50 eV. Scanning ranges were 295−280, 545−525, and 99−79 eV, respectively. Shipping and handling were done in ambient conditions without further precautions. The samples were measured in a Cu metal powder sample holder without the use of conductive tape. Charge compensation was achieved by an electron flood gun. Binding energy calibration was performed by setting the C 1s binding energy of the graphitic sp^2 carbon to 284.5 eV. The measurements were performed by Prof. Dr. Jan Philipp Hofmann in the Eindhoven University of Technology, The Netherlands.

Thermogravimetric Analysis (Coupled with Mass Spectrometry)

Thermogravimetric analysis (TGA) is a technique for monitoring the mass of a substance as a function of temperature or time. A sample is subjected to a specified temperature program in a controlled atmosphere. The analysis of the gases released upon heating can

be accomplished by coupling with a mass spectrometer (TGA-MS), which offers further information about the sample composition.

TGA measurements were performed using a thermo-microbalance TG 209 F1 Libra (Netzsch, Selb, Germany). A platinum crucible was used for the measurement of 10 ± 1 mg of samples in a N_2 flow of 20 mL min^{-1} and a purge flow of 10 mL min^{-1} and an additional 5 mL min^{-1} O_2 flow for the measurements in synthetic air. The samples were heated to 1000 °C with a heating rate of 10 °C min^{-1}. For TGA-MS measurements the same instrument was used, coupled with a Thermostar Mass spectrometer (Pfeiffer Vacuum; Asslar/Germany) with ionization energy of 75 eV. The samples were heated to 1000 °C with a heating rate of 2.5 °C min^{-1} in a helium flow of 10 mL min^{-1} and a purge flow of 10 mL min^{-1}. The data was recorded and analyzed by the Proteus (6.1.0) and Quadstar (7.03) software package. The measurements were carried out by Antje Völkel from MPIKG.

Elemental Analysis

Elemental microanalysis (EA) is an analytical method based on the complete and instantaneous combustion of the sample, which converts all the organic and inorganic components of the sample into combustion products. This enables the quantification of the C, H, N, and S in the sample. The sample is combusted in O_2 atmosphere at ≈ 1000 °C, either alone or with the addition of a metal oxide catalyst. After the mixture of combustion gases passes over a catalyst layer, individual components (N_2, CO_2, H_2, and SO_2) are separated and detected with a thermal conductivity detector.

C/H/N/S EA in the present thesis was accomplished using a Vario Micro device, and the measurements were performed by Antje Völkel from MPIKG.

Inductively Coupled Plasma – Optical Emission Spectrometry

ICP-OES or inductively coupled plasma atomic emission spectroscopy (ICP-AES) is an analytical method for quantification of almost all elements. It uses inductively coupled plasma as an excitation source, through which argon is passed continuously. The electrically conducting ionized gas reaches temperatures of ≈ 10000 K. A sample, usually in the form of an aqueous solution, is partly converted into fine droplets by a nebulizer,

and an aerosol is subsequently injected in an argon flow. At the temperature of ≈ 7500 K, the sample is atomized and the atoms become excited and ionized. The intensity of emitted element-specific radiation is then measured. The quantification of the elements is accomplished through the comparison of previously measured calibration intensities.[276]

ICP-OES in Chapter 5.1 was conducted by using a Horiba Ultra 2 instrument equipped with photomultiplier tube detection. The content of the gold in the catalysts was determined by analyzing the solution after deposition on the carbon support. A metal leaching test was conducted by analyzing the catalytic reaction solution after the reaction. The measurements were performed by Ines Below-Lutz from MPIKG.

Isothermal Titration Calorimetry

Isothermal titration calorimetry is a technique that directly measures the heat change associated with interactions of two components mixing in the solution at a constant temperature. It is most often used for studying the binding of small molecules to macromolecules, such as protein binding. Characterization of the thermodynamics of a binding reaction requires determining the Gibbs free energy change (ΔG) and change in enthalpy and entropy (ΔH and ΔS) at a given temperature. They are dependent variables obtained by the following Equation 8.6.

$$\Delta G° = -RT \ln K = \Delta H° - T\Delta S° \tag{8.6}$$

Where K is the binding constant. A typical ITC experiment is performed at a constant temperature by titrating one binding partner (the titrant) into a solution of other binding partner (the titrand) in the sample cell (**Figure 8.4**). The titration is automated and occurs from a precision syringe, which is also stirring the contents of the sample cell to ensure the rapid mixing of the binding partners. The heat released or absorbed upon the addition of a small aliquot of titrant is measured against the reference cell filled with buffer. The signal is expressed as the electrical power (J s^{-1}) necessary to maintain a constant temperature difference between the sample cell and the reference cell, which are placed in an adiabatic jacket. Raw signal can be integrated to yield total calorimetric heat change per mol of titrant, plotted against the total ligand concentration, or number of titrations.

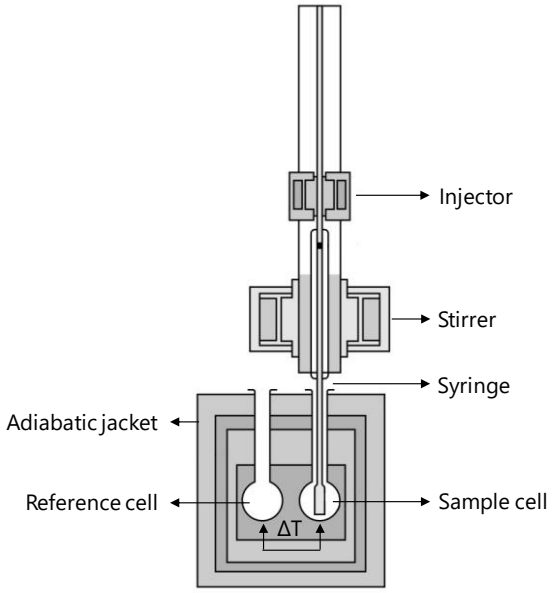

Figure 8.4. *Cross-section of the isothermal titration calorimeter.*

This technique also enables to probe chiral molecular interactions,[228, 277] by measuring the differences between interactions with different enantiomers of the same compound, as shown in the thesis on hand. The ITC data contains the following information: free energy changes, enthalpy changes, calorimetric and van't Hoff enthalpy changes, change in the heat capacity (if a sufficient number of measurements at different temperatures is performed), as well as entropy changes. However, most of these parameters are possible to calculate only for certain well-defined systems and are therefore not expressed in present studies due to difficulties imposed by titrating a dispersion instead of a solution, and thus numerous contributions to the signal.[278-280]

ITC measurements reported in Chapter 4 were performed using a VP-ITC microcalorimeter from MicroCal (Northampton, USA). The working cell of a volume of 1.442 mL was filled with an aqueous dispersion of the sample, and the reference cell of the same volume was filled with water. The titrant (L-Phenylalanine or D-Phenylalanine, c = 20 mM in Chapter 4.1, c = 60 mM in Chapter 4.2) was injected stepwise into the working cell with a syringe of the total volume of 288 µL. The sample cell was constantly stirred at a stirring rate of 307 rpm. The measurements were performed at a constant temperature of 25 °C. Small aliquots of titrant (5 µL) were injected into the solution of the working cell. The first injection was set to a volume of 2 µL, because of the possible dilution during the equilibration time

preceding the measurement, and therefore the first injection was ignored in the analysis of the data. Spacing between the injections was set to 300 s. Data analysis was performed using the Origin software provided by MicroCal.

Catalytic Tests

In Chapter 5.1 the catalytic oxidation of D-glucose was monitored via a potentiometric titrator (TitroLine 6000/7000) device with the functionality of a TITRONIC piston burette. The reaction was performed with 50 mL of 0.1 M D-glucose and 50 mg of 1 wt % Au on a C catalyst at 45 °C, pH = 9, under an oxygen flow of ≈ 250 mL min^{-1} and stirring at 800 rpm. The pH of the solution was kept constant at pH = 9 by automatic titration with 1 M aqueous NaOH solution. The catalytic activity was evaluated from the slope of the titration curve, in the range between 1 and 3 mL of added NaOH, which corresponds to the conversion between 20% and 60% of D-glucose.

Control catalytic experiments without the oxygen flow were performed by using selected mesoporous catalysts: Au-CMK-3, Au-STC-8, and Au-STC-2. The dispersion of a catalyst in water (50 mg in 10 mL) was saturated with oxygen under a flow of ≈ 250 mL min^{-1} for 7 min. Then the oxygen flow was stopped, and D-glucose solution (0.125 M) was added to the mixture to obtain a final concentration of 0.1 M. Finally, monitoring the reaction with the titrator described above was started. The atmosphere above the reaction mixture was purged with nitrogen.

In the Chapter 5.2 the same setup was used and the reaction was performed with 50 mL of 0.2 M D-glucose and 10 mg of 1 wt % Au on C catalyst at 30 °C, pH = 9, under an oxygen flow of ≈ 50 mL min^{-1} and stirring at 800 rpm. The pH of the solution was kept constant at pH = 9 by automatic titration with 1 M aqueous NaOH solution.

Nuclear Magnetic Resonance Spectroscopy

NMR spectroscopy offers a complete analysis of the structure, content, and purity of chemical compounds. This non-destructive technique relies on the characteristic spin of the nuclei of many elemental isotopes, most commonly ^{1}H, ^{13}C, ^{19}F, ^{31}P, and others. The sample is placed in an external magnetic field, inducing the energy levels to split up. The

energy gap equals a frequency of radiation, which depends on the strength of the external magnetic field, as well as the magnetic properties of the isotopes. Since the magnetic field is affected by electron shielding of a nucleus, different chemical environment delivers different resonant frequencies, which is a valuable source of information in structural analysis. A one-dimensional NMR experiment is usually sufficient for the interpretation of small organic molecules, but complex structures or overlapping resonances may be further analyzed by introducing a second dimension to the spectrum. In 2D NMR methods, two major groups can be distinguished, depending on whether the magnetization transfer occurs between nuclei of the same type, called homonuclear through-bond correlation methods, or between nuclei of two different types, called heteronuclear through-bond correlation methods.[281]

The products of the D-glucose oxidation reaction were analyzed by NMR on a Bruker Ascend 400 (400 MHz) spectrometer. Chemical shifts δ are reported in ppm and are adjusted to internal standards of the residual proton signal of the deuterated solvent (D_2O: 4.79 ppm for ^1H). The spectra were measured at room temperature. Having symmetrical signals, the center of this signal is given and for multiplets the area. Thereby the following characterization was used: s = singlet, sbr = singlet broad, d = doublet, t = triplet, q = quartet, m = multiplet or combinations like dd = doublet of doublet, or dt = doublet of triplet. Coupling constants (J) are given in Hz. Data were evaluated by using MestReNova v.12.0.4-22023 software. For ^1H NMR spectra, the correlation of the signals was done by the multiplicities. 2D spectra were recorded by heteronuclear single-quantum correlation (HSQC) as well as heteronuclear multiple-bond correlation (HMBC) spectroscopy.[282] HSQC was applied for the detection of correlations between ^{13}C and ^1H nuclei that are separated by one bond. HMBC was applied for the detection of correlations between ^{13}C and ^1H nuclei over longer ranges of 2–4 bonds.

8.3. Experimental Section

8.3.1. List of Used Chemicals

Substance	Chemical formula	Purity grade	Supplier
(R)-(−)-2-Butanol	$CH_3CH(OH)CH_2CH_3$	99%	Aldrich
(S)-(+)-2-Butanol	$CH_3CH(OH)CH_2CH_3$	99%	Aldrich
activated carbon	C	–	Carl Roth
Deuterium oxide	D_2O	99.9 atom % D	Aldrich
dimethylformamide	C_3H_7NO	99.8%	Aldrich
D-Glucose	$C_6H_{12}O_6$	99.5%	Carl Roth
D-Phenylalanine	$C_9H_{11}NO_2$	≥98.5%	Carl Roth
D-Tyrosine	$C_9H_{11}NO_3$	≥98%	Carl Roth
ethanol	CH_3CH_2OH	≥99.8%	Aldrich
FC-72 (tetradecafluorohexane)	C_6F_{14}	98%	abcr
hexaazatriphenylene-hexacarbonitrile	$C_{18}N_{12}$	95%	Aldrich
hydrochloric acid	HCl	37%	Aldrich
L-Phenylalanine	$C_9H_{11}NO_2$	≥99%	Carl Roth
L-Tyrosine	$C_9H_{11}NO_3$	≥99%	Carl Roth
Pluronic P123 (PEG-PPG-PEG)	$HO(CH_2CH_2O)_{20}(CH_2CH(CH_3)O)_{70}(CH_2CH_2O)_{20}H$	≥99%	Aldrich
sodium borohydride	$NaBH_4$	≥98%	Aldrich
sodium citrate	$Na_3C_6H_5O_7$	≥99%	Aldrich
sodium gluconate	$C_6H_{11}NaO_7$	≥99%	Sigma-Aldrich
sodium hydroxide	NaOH	≥98%	Aldrich
sucrose	$C_{12}H_{22}O_{11}$	>99.5%	Aldrich
sulfuric acid	H_2SO_4	98%	Merck
tetrachloroauric acid	$HAuCl_4 \cdot 3H_2O$	99%	Aldrich
tetraethyl orthosilicate	$SiC_8H_{20}O_4$	≥99%	Aldrich
trimesic acid	$C_9H_6O_6$	95%	Sigma-Aldrich
zinc chloride	$ZnCl_2$	>98%	Alfa Aesar

8.3.2. Materials Synthesis

Synthesis of SBA-15

The hexagonal ordered silica template SBA-15 was synthesized by dissolving 33.4 g of the triblock copolymer Pluronic P123 in 606 g of deionized water and 19.3 g of concentrated aqueous hydrochloric acid solution overnight at 35 °C in a 1000 mL polypropylene bottle under intense stirring. Then, 71.8 g of tetraethyl orthosilicate was added to the solution, and the mixture was stirred at 35 °C for another 24 h. The white suspension was then transferred to a Teflon-lined autoclave and hydrothermally treated at 130 °C for 24 h followed by filtration and washing with ~1000 mL of deionized water/ethanol (1:1 by volume). For the complete removal of the structure-directing agent, the SBA-15 was calcined at 550 °C for 5 h in a muffle furnace under an air atmosphere (heating rate: 60 °C h^{-1}).[67]

Synthesis of L-m-carbon and D-m-carbon

Ordered mesoporous chiral carbon was synthesized by impregnating 0.5 g of SBA-15 with a solution of 0.625 g chiral ionic liquid and 0.21 g trimesic acid in 3.5 mL water and 1.5 mL ethanol. Chiral ionic liquids, N,N,N-trimethyl-L-Tyrosine methyl ester tetrafluoroborate, and its D-enantiomer were synthesized by a previously reported procedure.[124, 223] The mixture was transferred to the Petri dish, dried at 100 °C for 6 h, subsequently heated to 160 °C, and kept for 6 h. Complete infiltration of template pores was achieved by repeating the procedure with a solution of 0.4 g chiral ionic liquid and 0.13 g trimesic acid in 3.5 mL water and 1.5 mL ethanol, followed by heating to 100 °C and 160 °C. Carbonization was carried out under a flowing N_2 atmosphere in a horizontal tubular furnace. The material was heated to 500 °C (heating rate: 150 °C h^{-1}) and dwelled for 2 h. Silica removal was achieved by refluxing the carbonized composite material in sodium-hydroxide solution (100 mL, 5 mol L^{-1}) overnight. After filtration and washing with large amounts of ethanol, the chiral carbon was dried at 60 °C.

Synthesis of CMK-3

Ordered mesoporous carbon CMK-3 was synthesized by impregnating 4 g of SBA-15 with 20 mL aqueous solution of 5 g sucrose to which was added 0.56 g 96% sulfuric acid. Polymerization of the carbohydrate was achieved by heating the mixture to 100 °C for 6 h, followed by heating to 160 °C for another 6 h. Reimpregnation of the silica pores was accomplished similarly, with a 20 mL aqueous solution of 3.2 g of sucrose to which was added 0.36 g of 96% sulfuric acid, followed by heating to 100 °C and 160 °C. Carbonization was carried out under a flowing N_2 atmosphere in a horizontal tubular furnace. The material was heated to 900 °C (heating rate: 150 °C h^{-1}) and dwelled for 2 h. Silica removal was achieved by refluxing the carbonized composite material in sodium-hydroxide solution (400 mL, 5 mol L^{-1}) overnight. After filtration and washing with large amounts of ethanol, the CMK-3 material was dried at 60 °C.[72]

Synthesis of C_2N/C composite

The C_2N-type coating on C carbon was synthesized by wet impregnation of 200 mg of C with the solution of 267 mg of hexaazatriphenylene-hexacarbonitrile (HAT-CN)[229] in 0.4 mL of dimethylformamide. After drying overnight at 70 °C under vacuum, the material was heated to 550 °C (heating rate: 240 °C h^{-1}) and dwelled for 2 h.

Synthesis of L-composite and D-composite

The chiral coating on C_2N/C composite was synthesized by wet impregnation of 179 mg of C_2N/C composite with a solution of 230 µL of N,N-dimethyl-L-Proline methyl ester bis(trifluoromethylsulfonyl)imide (L-Pro-TFSI) chiral ionic liquid in 0.46 mL of dimethylformamid. The same procedure was followed for the D-enantiomer. Chiral ionic liquids were synthesized by a previously reported procedure.[124] After drying overnight at 70 °C under vacuum, the material was heated to 500 °C (heating rate: 240 °C h^{-1}) and dwelled for 2 h.

Synthesis of the Colloidal AuNP Dispersion

The colloidal gold dispersion was synthesized by a modified Turkevich method.[260] 29 mL of 0.2 wt % $HAuCl_4 \cdot 3H_2O$ (49 wt % Au) was added to 500 mL of deionized water while

stirring. Then 1 wt % sodium citrate aqueous solution (11.6 mL) was added. After 30 s, 5.80 mL of freshly prepared sodium borohydride solution (17 mg of $NaBH_4$ in 10 mL of ice-cooled 1 wt % aqueous sodium citrate solution) was added to the mixture.

Synthesis of the Au-STC-x and Au-CMK-3 catalysts

The 1 wt % gold-on-carbon catalysts were synthesized by depositing gold nanoparticles on carbon supports by immersing 500 mg of the carbon into 91.1 mL of colloidal gold dispersion, followed by sonication for 2 h. The catalyst was separated by centrifugation at 4000 rpm for 20 min, washed three times with deionized water, and dried overnight in a vacuum oven at 60 °C.

Fabrication of Au-C-PFC and Au-C-HC emulsions

Most stable Au-C-PFC emulsions were obtained for 0.02 wt % Pickering emulsifier in a 95/5 % (v/v) mixture of water and perfluorocarbon (FC-72). First, 0.2 mg mL^{-1} Au-C catalyst was dispersed in water and the mixture was sonicated for a few minutes. Subsequently, the required amount of PFC was added in different volumes and vortex mixed for 10 seconds. The same procedure was followed for the synthesis of the hydrocarbon emulsions (Au-C-HC).

8.4. Supporting Figures and Tables

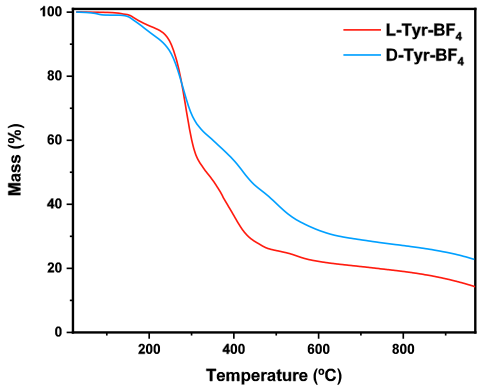

Figure S 1. *Thermal analysis of chiral ionic liquids L-Tyr BF_4 and D-Tyr BF_4 measured under nitrogen flow with a heating rate of 10 °C min^{-1}.*

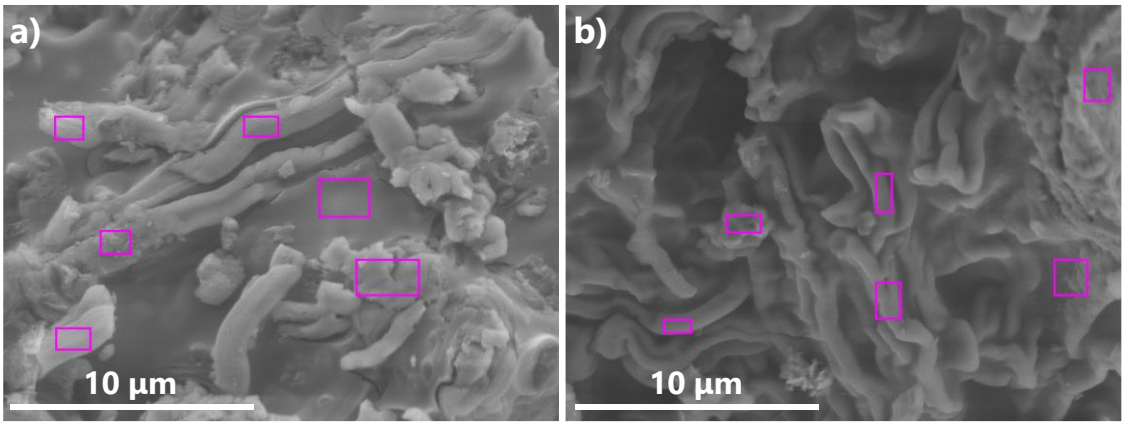

Figure S 2. *SEM images of a) L-m-carbon, and b) D-m-carbon, with marked areas on which the EDX analysis was performed.*

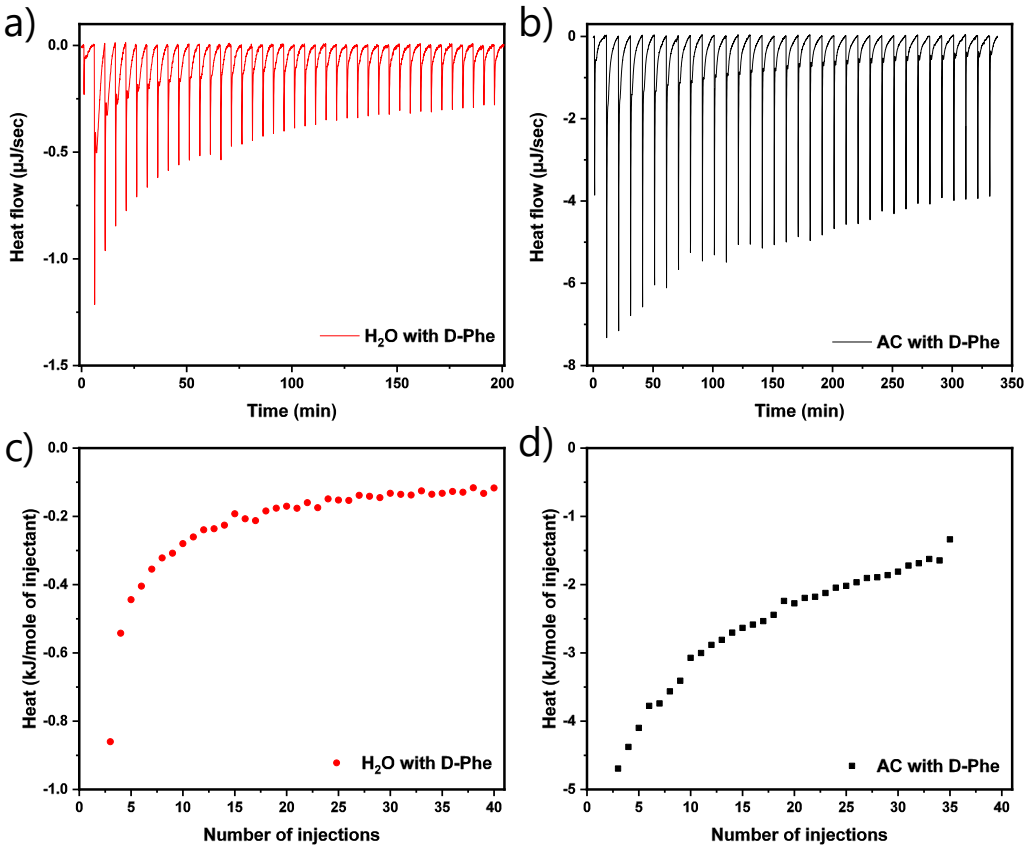

Figure S 3. *Raw ITC data from injecting D-Phenylalanine into a) water, and b) dispersion of activated carbon. Heat per mole of injected D-Phenylalanine into c) water, and d) dispersion of activated carbon.*

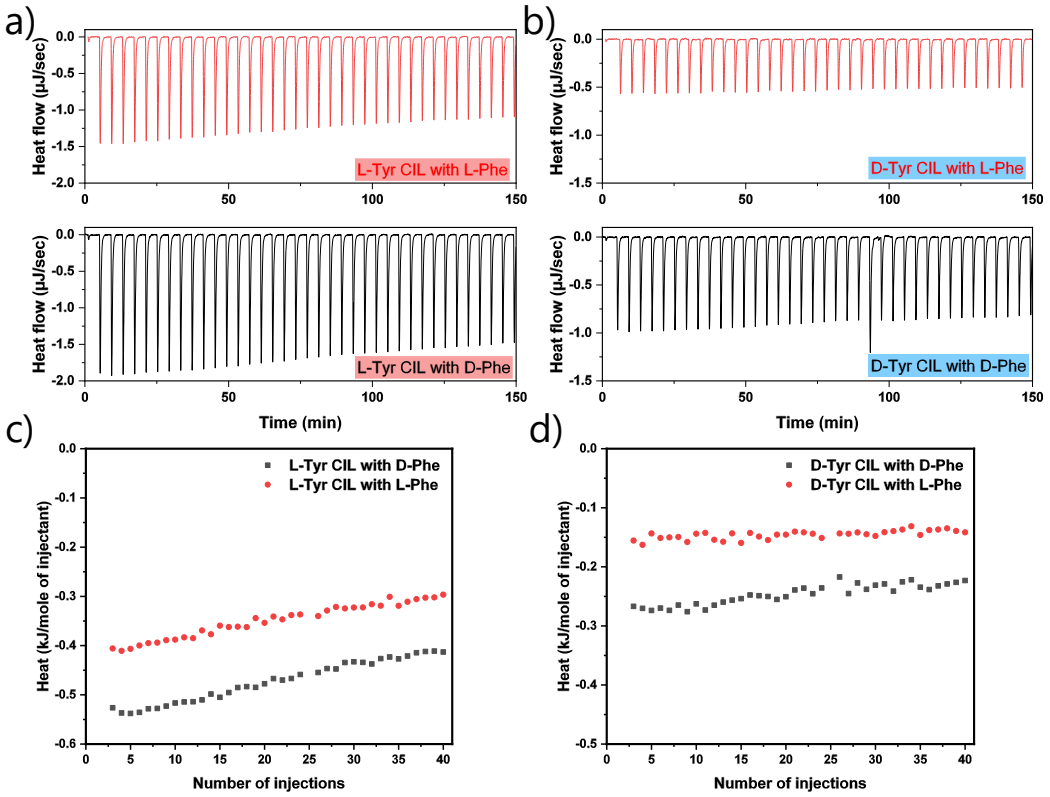

Figure S 4. *a) and b) Raw ITC data from injecting L-Phenylalanine (upper panel), and D-Phenylalanine (lower panel), into a) L-Tyr BF_4, and b) D-Tyr BF_4. Heat per mole of injected D-Phenylalanine (black points), and L-Phenylalanine (red points), into c) L-Tyr BF_4, and b) D-Tyr BF_4.*

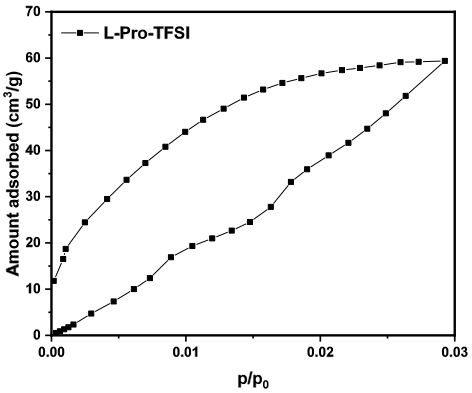

Figure S 5. *CO_2 physisorption isotherm (at 0 °C) of L-Pro-TFSI chiral ionic liquid carbonized at 400 °C. Measurement performed on a sample m<10 mg.*

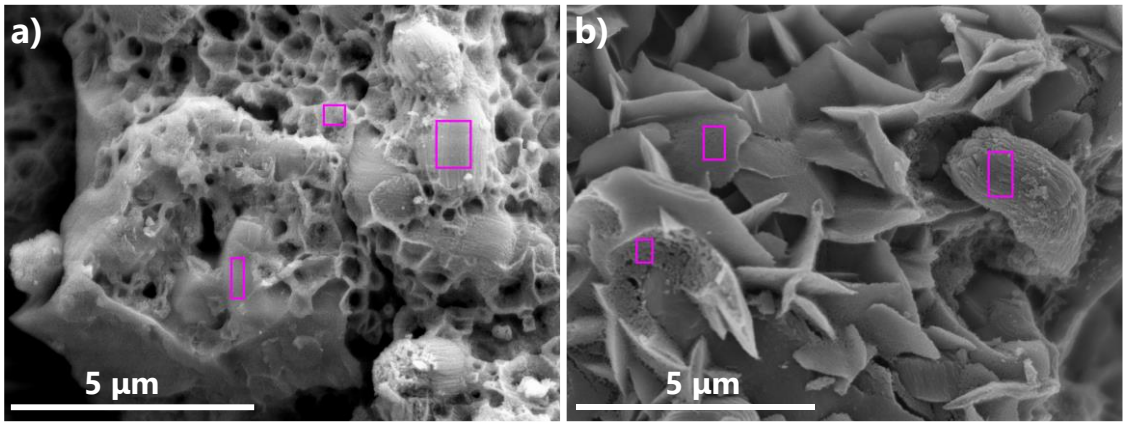

Figure S 6. *SEM images of a) L-composite, and b) D-composite, with marked areas on which the EDX analysis was performed.*

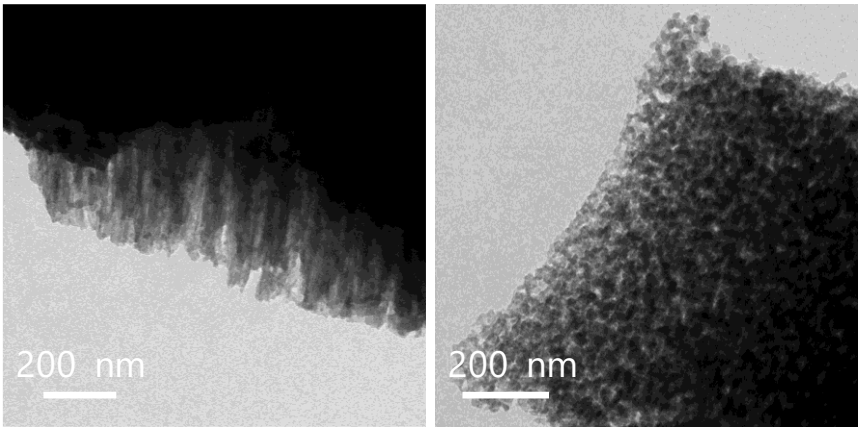

Figure S 7. *TEM images of C_2N/C composite.*

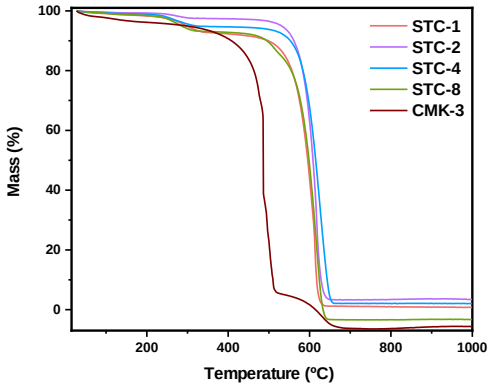

Figure S 8. *Thermogravimetric analysis (TGA) results of STCs and CMK-3 measured under synthetic air with a heating rate of 10 °C min^{-1}.*

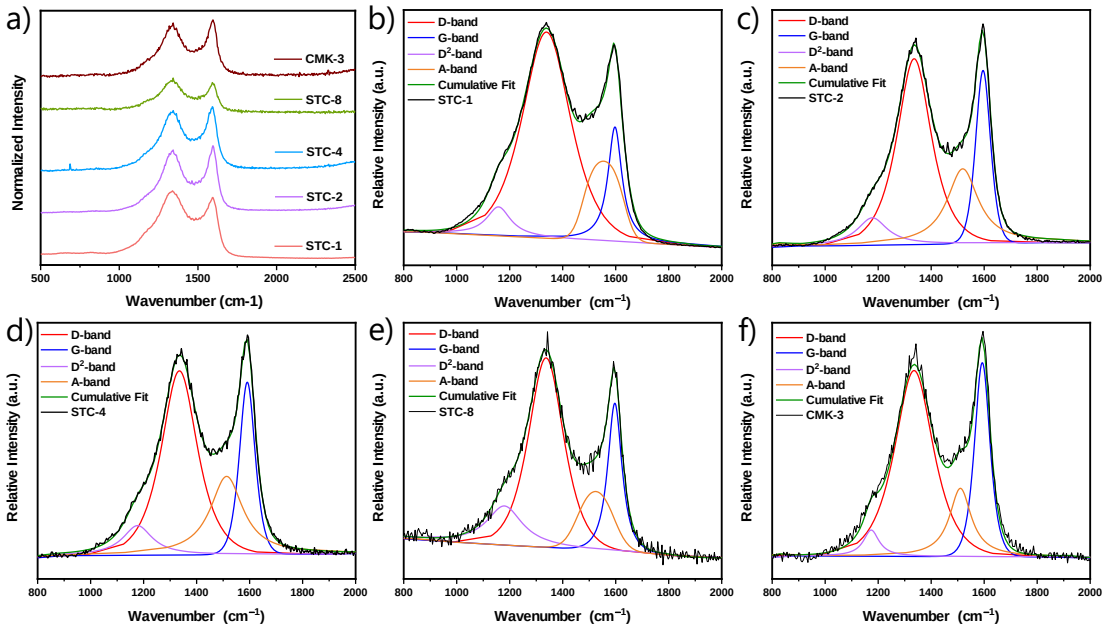

Figure S 9. *a) Raman spectra of STCs and CMK-3, and (b-f) corresponding fitted spectra of STC-1, STC-2, STC-4, STC-8, and CMK-3.*

Table S 1. *XPS fits including peak positions, full width at half maximum, and raw area.*

Sample	Peak	Position	FWHM	Raw Area
Au-STC-1	Au $4f_{7/2}$	84.2	1.0	12406
	Au $4f_{5/2}$	87.8	1.0	9305
	Au $4f_{7/2}$	86.2	1.0	773
	Au $4f_{5/2}$	89.8	1.0	580
	Csp^3	285.3	2.0	4196
	COR	286.8	2.0	2648
	CO	288.3	2.0	1009
	COOR	289.3	2.0	2613
	Csp^2	284.5	1.5	45244
	C 1s	291.1	2.0	1985
	O 1s	531.5	2.3	5963
	O 1s	533.3	2.3	4442
Au-STC-2	Au $4f_{7/2}$	84.0	0.9	8771
	Au $4f_{5/2}$	87.7	0.9	6578
	Au $4f_{7/2}$	86.0	0.9	430
	Au $4f_{5/2}$	89.7	0.9	323
	Csp^3	285.3	2.0	6104
	COR	286.8	2.0	3227

	CO	288.3	2.0	1248
	COOR	289.3	2.0	3767
	Csp^2	284.5	1.4	67149
	C 1s	291.2	2.0	2971
	O 1s	531.3	2.2	2879
	O 1s	532.9	2.2	6472
Au-STC-4	Au $4f_{7/2}$	84.0	0.9	5193
	Au $4f_{5/2}$	87.7	0.9	3895
	Au $4f_{7/2}$	86.0	0.9	280
	Au $4f_{5/2}$	89.7	0.9	210
	Csp3	285.3	2.0	5525
	COR	286.8	2.0	3020
	CO	288.3	2.0	1605
	COOR	289.3	2.0	3413
	Csp2	284.5	1.4	65852
	C 1s	291.0	2.0	3254
	O 1s	531.3	2.1	2688
	O 1s	533.0	2.1	4303
Au-STC-8	Au $4f_{7/2}$	84.1	1.0	22223
	Au $4f_{5/2}$	87.8	1.0	16668
	Au $4f_{7/2}$	86.1	1.0	1264
	Au $4f_{5/2}$	89.8	1.0	948
	Csp^3	285.3	2.0	8415
	COR	286.8	2.0	3603
	CO	288.3	2.0	1269
	COOR	289.3	2.0	4394
	Csp^2	284.5	1.4	68195
	C 1s	291.2	2.0	3668
	O 1s	531.0	2.2	2411
	O 1s	532.8	2.2	5461
Au-CMK-3	Au $4f_{7/2}$	84.1	1.0	12920
	Au $4f_{5/2}$	87.8	1.0	9690
	Au $4f_{7/2}$	86.1	1.0	675
	Au $4f_{5/2}$	89.8	1.0	506
	Csp^3	285.3	2.0	3633
	COR	286.8	2.0	4195
	CO	288.3	2.0	1437
	COOR	289.3	2.0	5156
	Csp^2	284.5	1.4	91797
	C 1s	291.2	2.0	4217
	O 1s	531.3	2.3	2752
	O 1s	532.8	2.3	5321

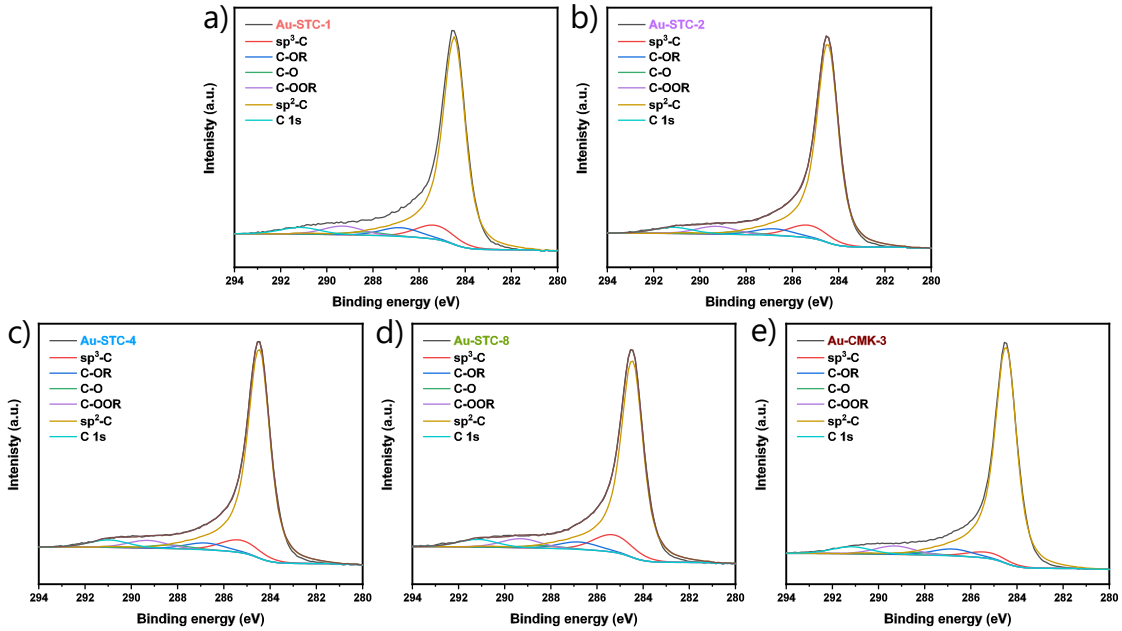

Figure S 10. *C 1s XPS spectra with fitted components of catalysts: a) Au-STC-1, b) Au-STC-2, c) Au-STC-4, d) Au-STC-8, and e) Au-CMK-3.*

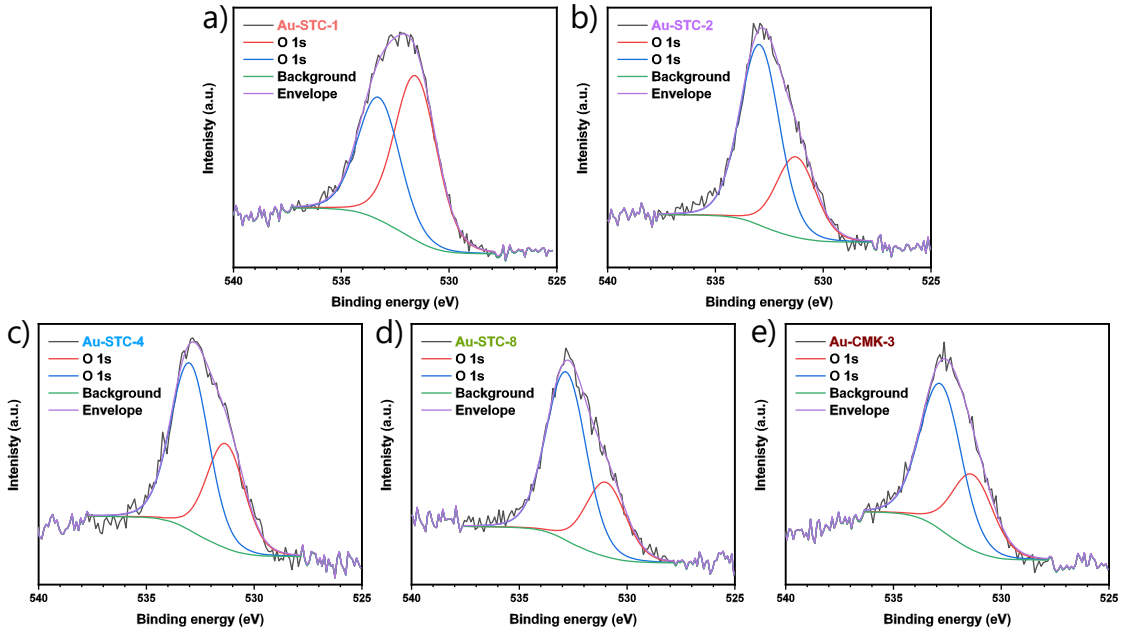

Figure S 11. *O 1s XPS spectra with fitted components of catalysts: a) Au-STC-1, b) Au-STC-2, c) Au-STC-4, d) Au-STC-8, and e) Au-CMK-3.*

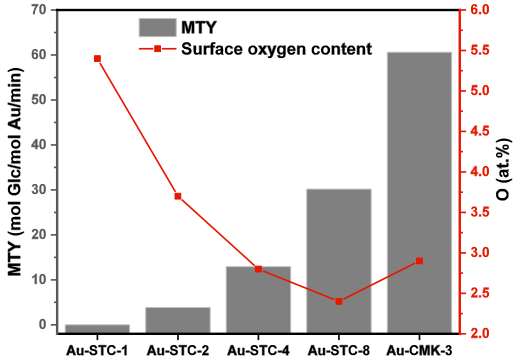

Figure S 12. *Correlation between catalytic activities (metal time yield) of the catalysts and their surface oxygen content.*

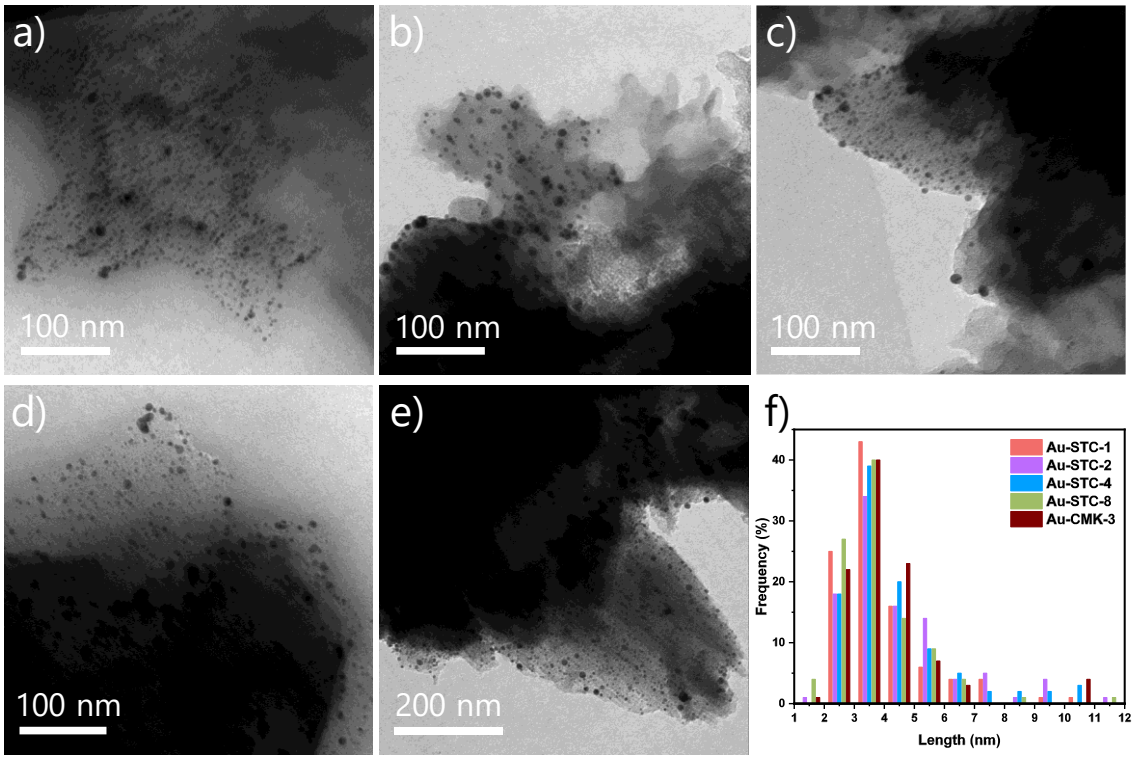

Figure S 13. *TEM images of catalysts after glucose oxidation reaction: a) Au-STC-1, b) Au-STC-2, c) Au-STC-4, d) Au-STC-8, e) Au-CMK-3, and f) corresponding AuNP size distributions.*

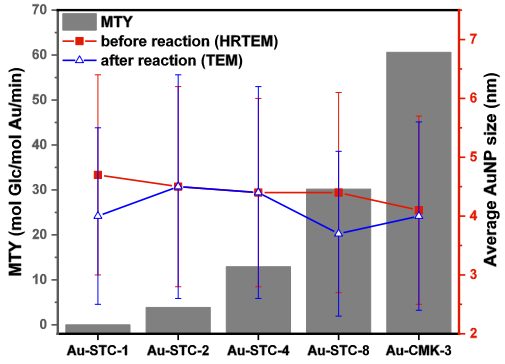

Figure S 14. *Correlation between catalytic activities (metal time yield) of the catalysts and their average AuNP size before and after the catalytic reaction.*

Table S 2. *Results of metal leaching test, determined by ICP-OES, reported with relative standard deviation, and in comparison to starting concentration of Au (10 mg L^{-1}). (All Au contents determined are below the applied calibration limit of the ICP-OES, which is 0.1 mg L^{-1}).*

Sample	Au [mg L^{-1}]	RSD [%]	Au [% from starting concentration]
Au-STC-1	0.059	5.4	0.59
Au-STC-2	0.037	2.3	0.37
Au-STC-4	0.033	2.3	0.33
Au-STC-8	0.072	7.3	0.72
Au-CMK-3	0.031	1.3	0.31

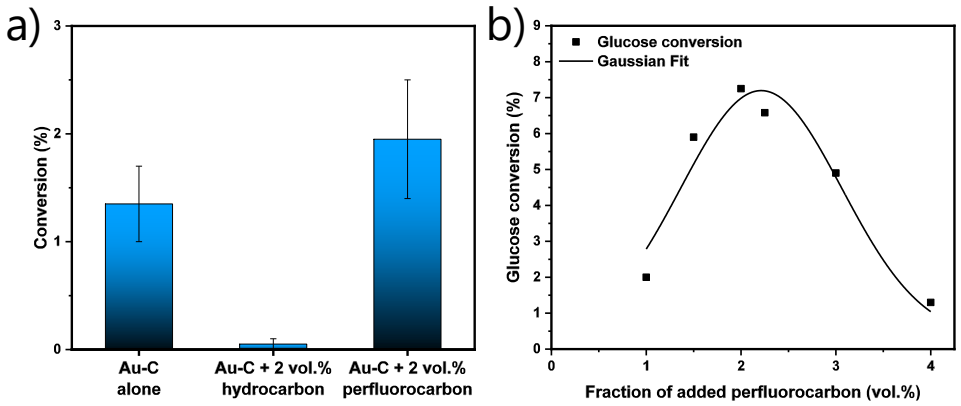

Figure S 15. *a) Diagram comparing three tested catalytic systems after 60 minutes, and b) dependence of D-glucose conversion on the volume fraction of added PFC after 170 minutes.*

Characterization of D-glucose and Na-gluconate.

D-glucose: ^{1}H NMR (400 MHz, D_2O) δ 5.17 (d, *J* = 3.7 Hz, 1H), 4.59 (d, *J* = 7.9 Hz, 1H), 3.91 – 3.75 (m, 3H), 3.74 – 3.57 (m, 3H), 3.52 – 3.27 (m, 5H), 3.19 (dd, *J* = 9.2, 7.9 Hz, 1H). ^{13}C NMR (101 MHz, D_2O) δ 95.79, 91.98, 75.83, 75.63, 74.00, 72.64, 71.35, 71.31, 69.51, 69.46, 60.62, 60.45.

Na-gluconate: ^{1}H NMR (400 MHz, D_2O) δ 4.07 (d, *J* = 3.8 Hz, 1H), 3.97 (dd, 1H), 3.78 – 3.75 (m, 1H), 3.73 – 3.68 (m, 2H), 3.64 – 3.58 (m, 1H). ^{13}C NMR (101 MHz, D_2O) δ 178.54, 73.98, 72.45, 71.02, 70.82, 62.48.

^{1}H, ^{13}C NMR, HSQC, and HMBC spectra of D-glucose and Na-gluconate.

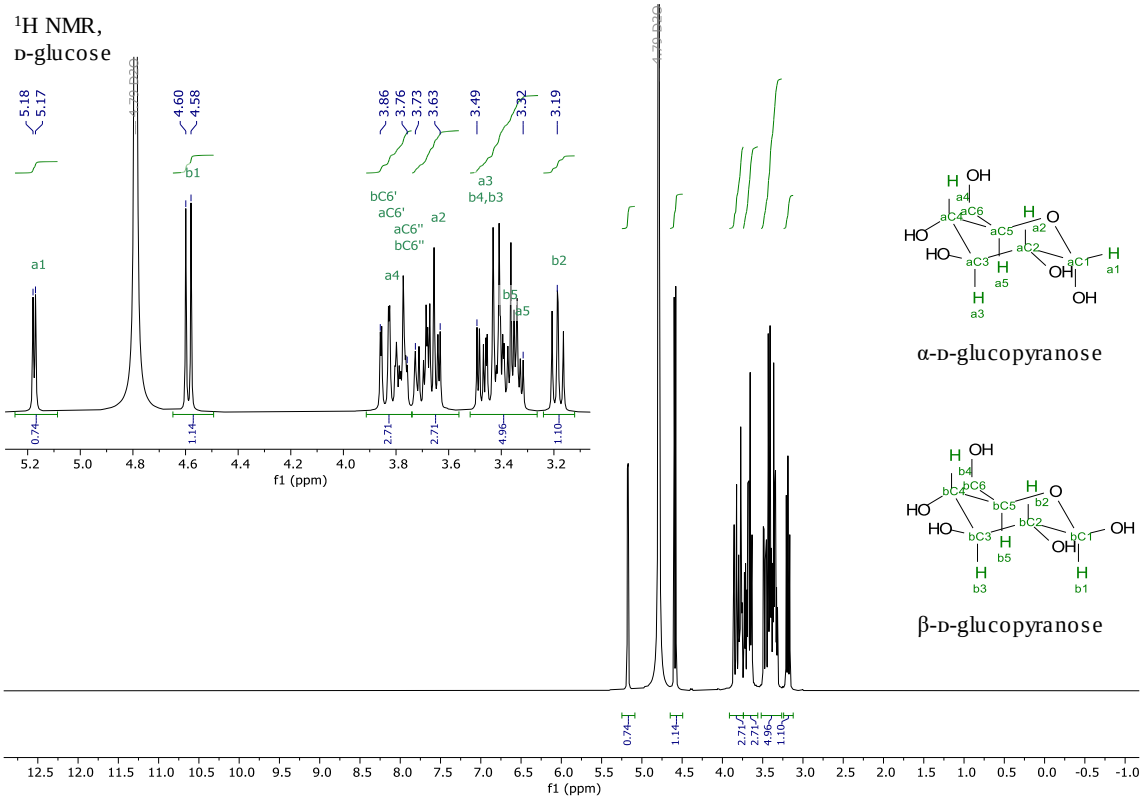

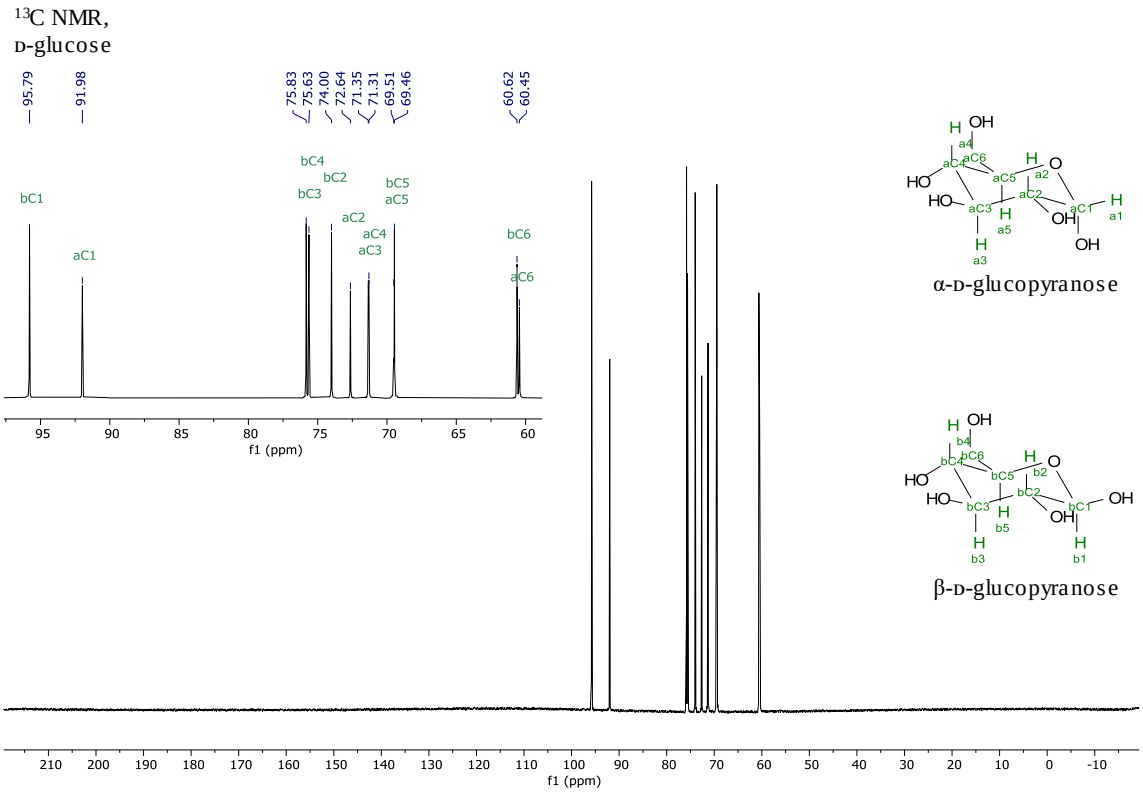

HSQC,
D-glucose

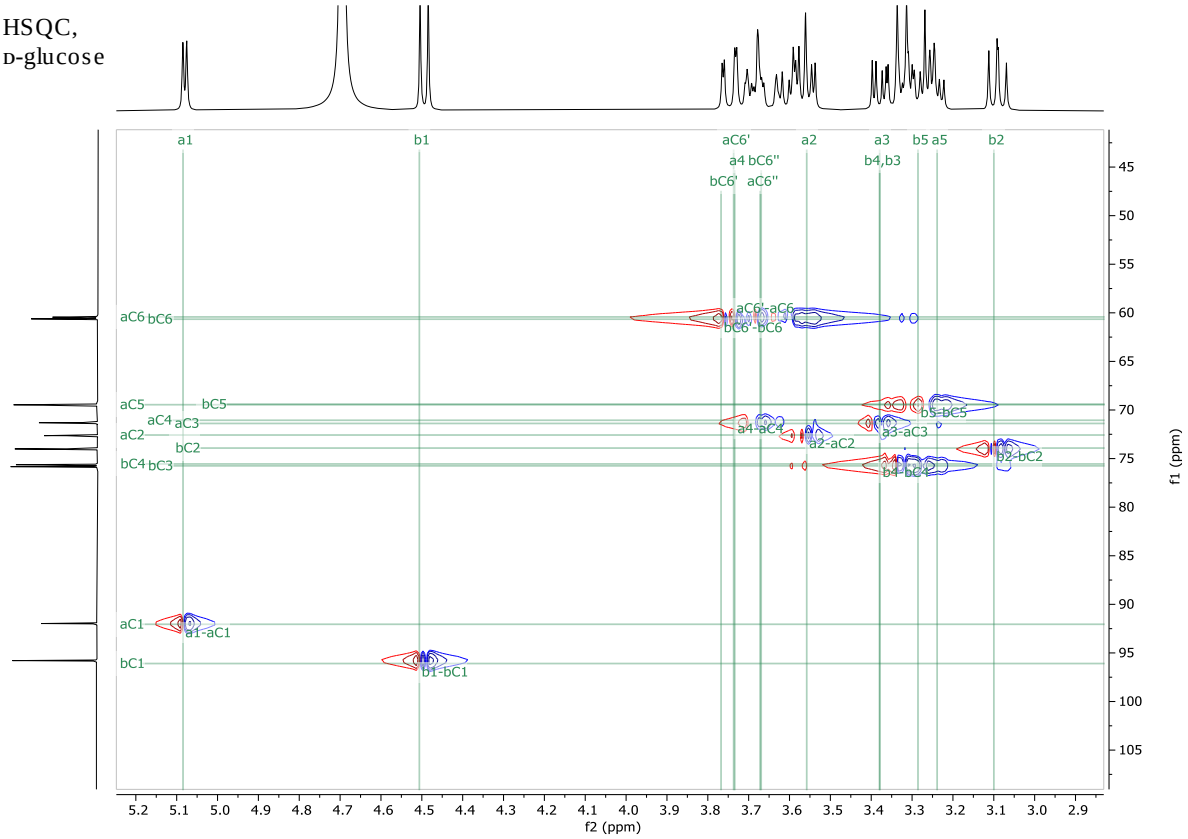

HMBC,
D-glucose

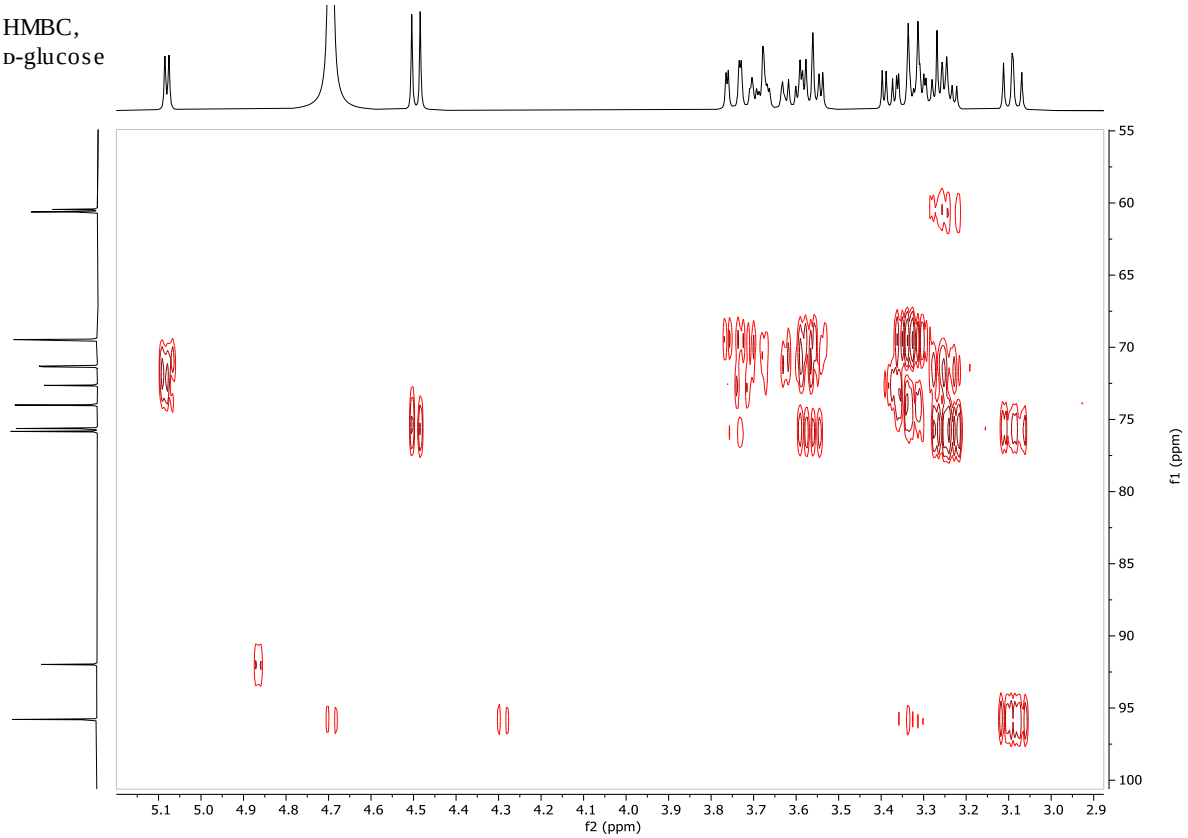

^{1}H NMR,
Gluconic acid

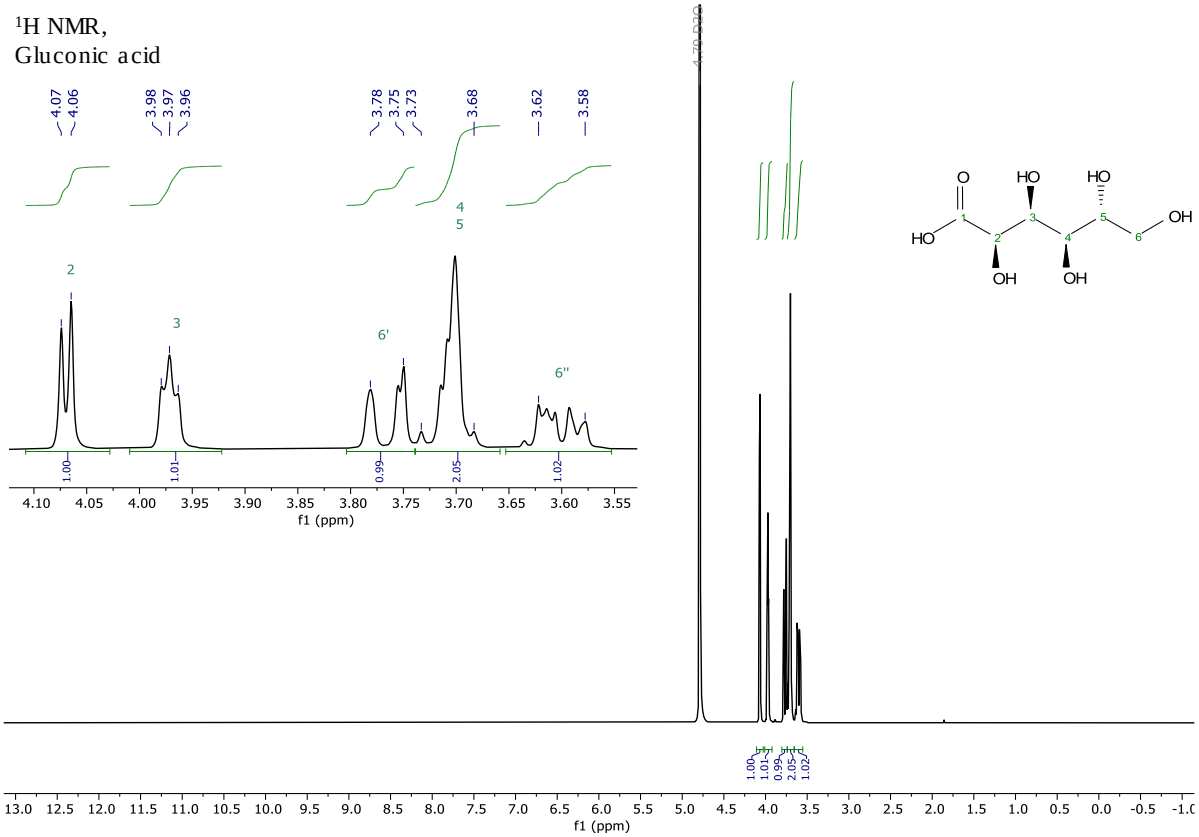

^{13}C NMR,
Gluconic acid

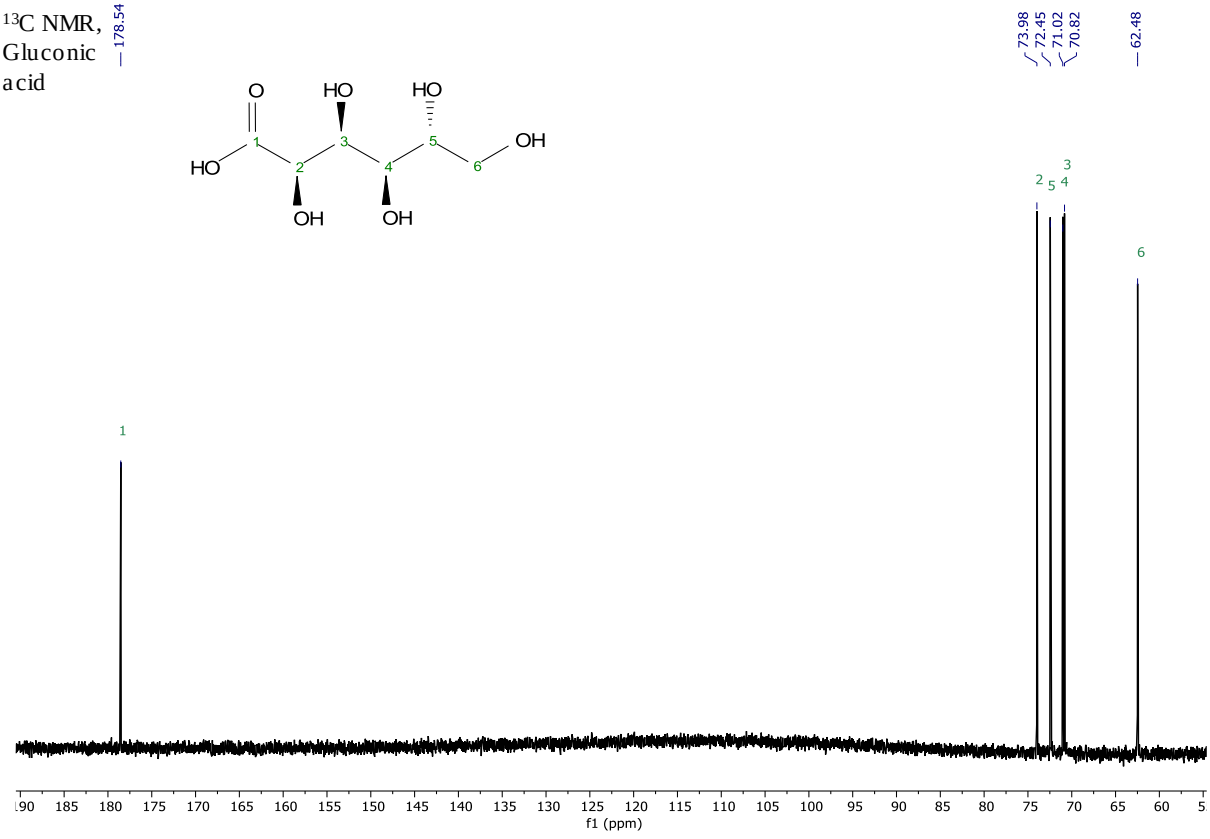

HSQC,
Gluconic acid

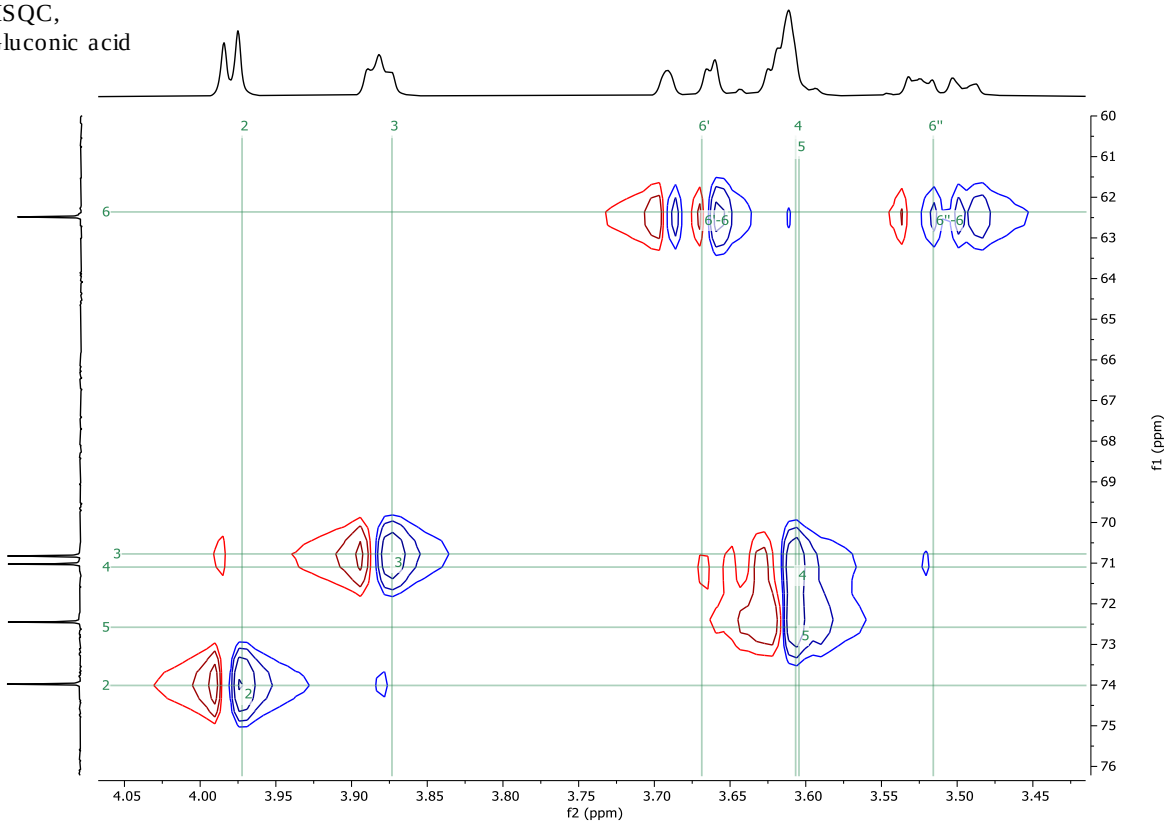

HMBC,
Gluconic acid

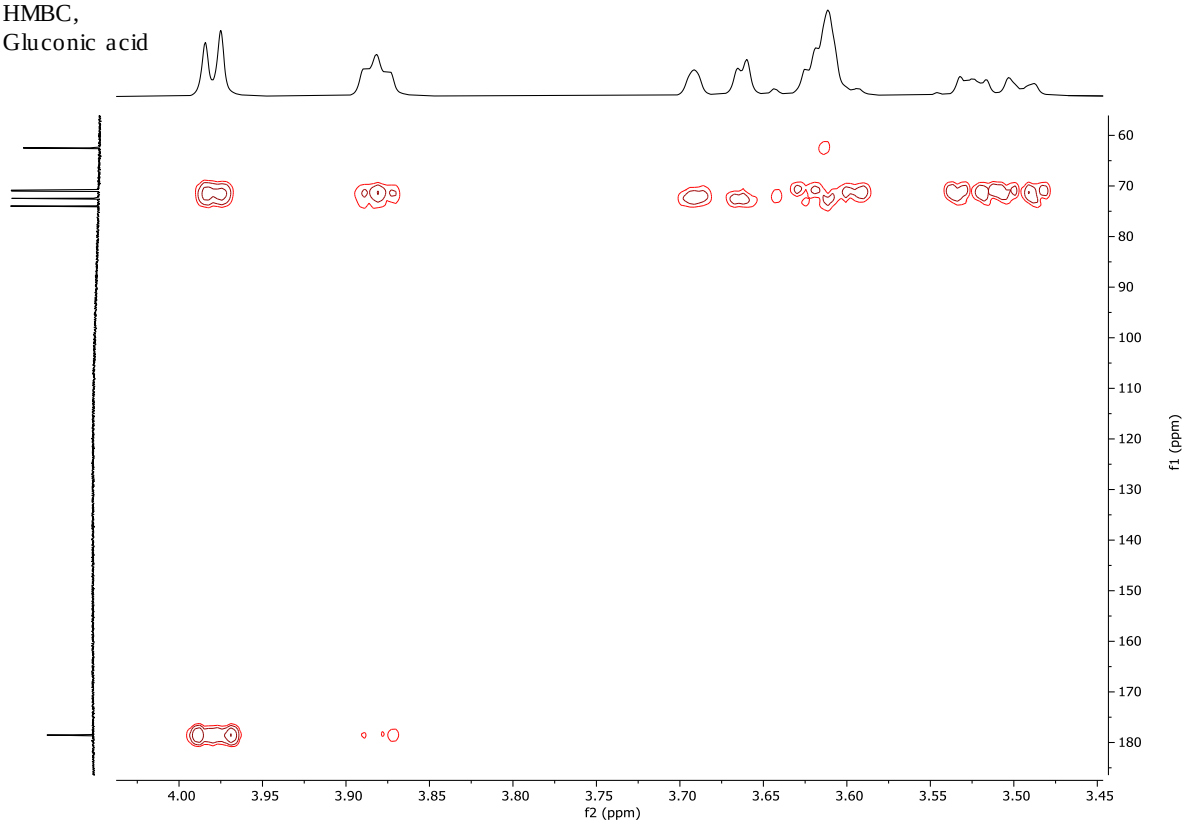

^{1}H and ^{13}C NMR spectra of the reaction mixtures after 5 h of the catalytic reaction with different catalysts.

^{1}H NMR,
Reaction mixture after catalysis with AuMK-3

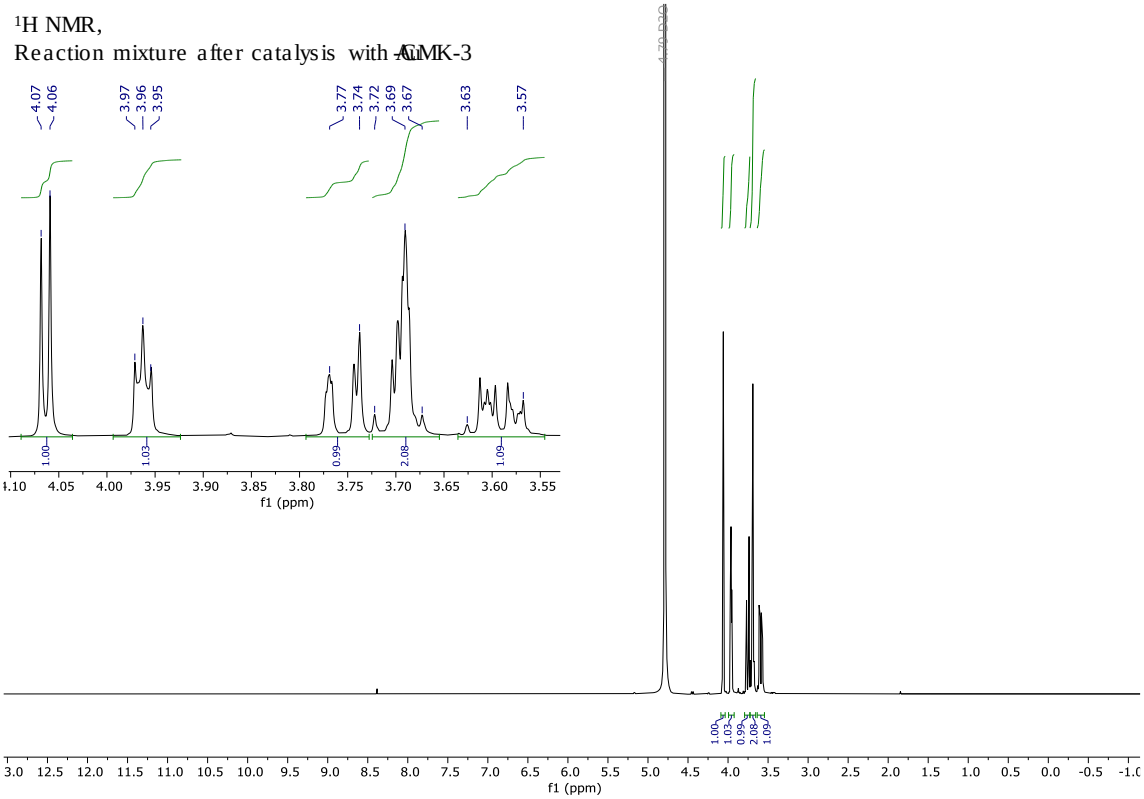

^{13}C NMR,
Reaction mixture after catalysis with AuMK-3

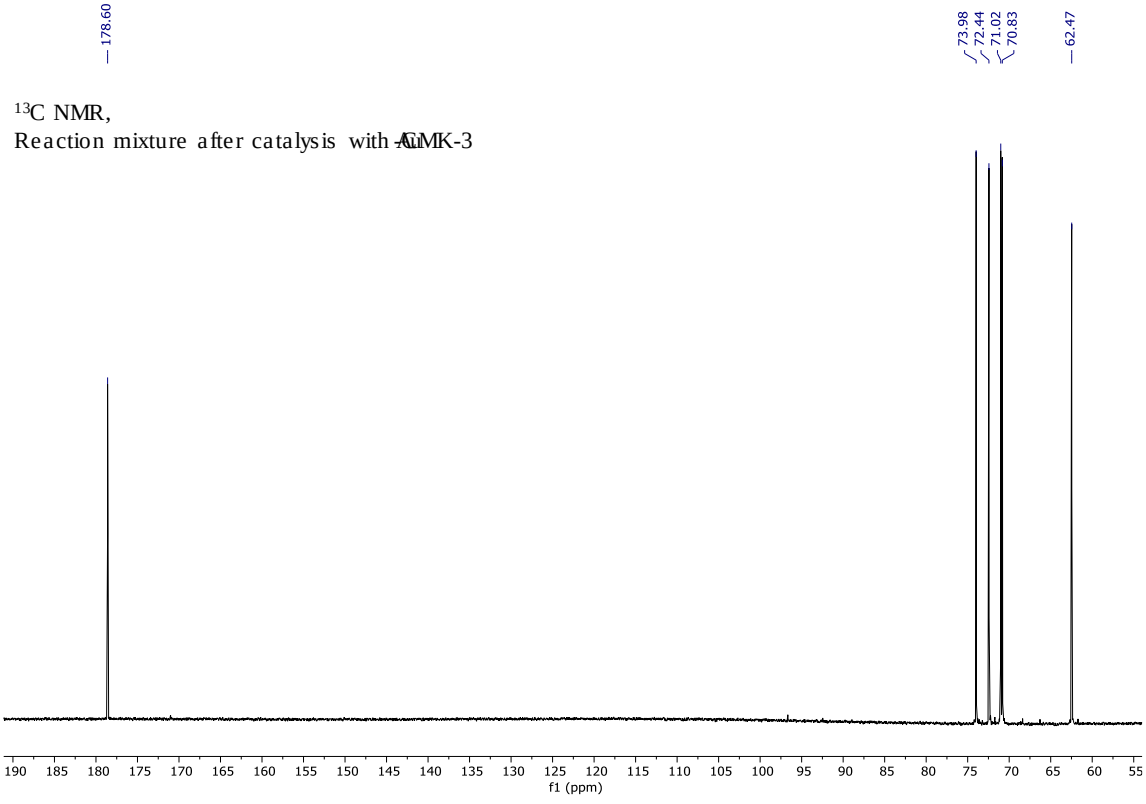

^{1}H NMR,
Reaction mixture after catalysis with AuTC-8

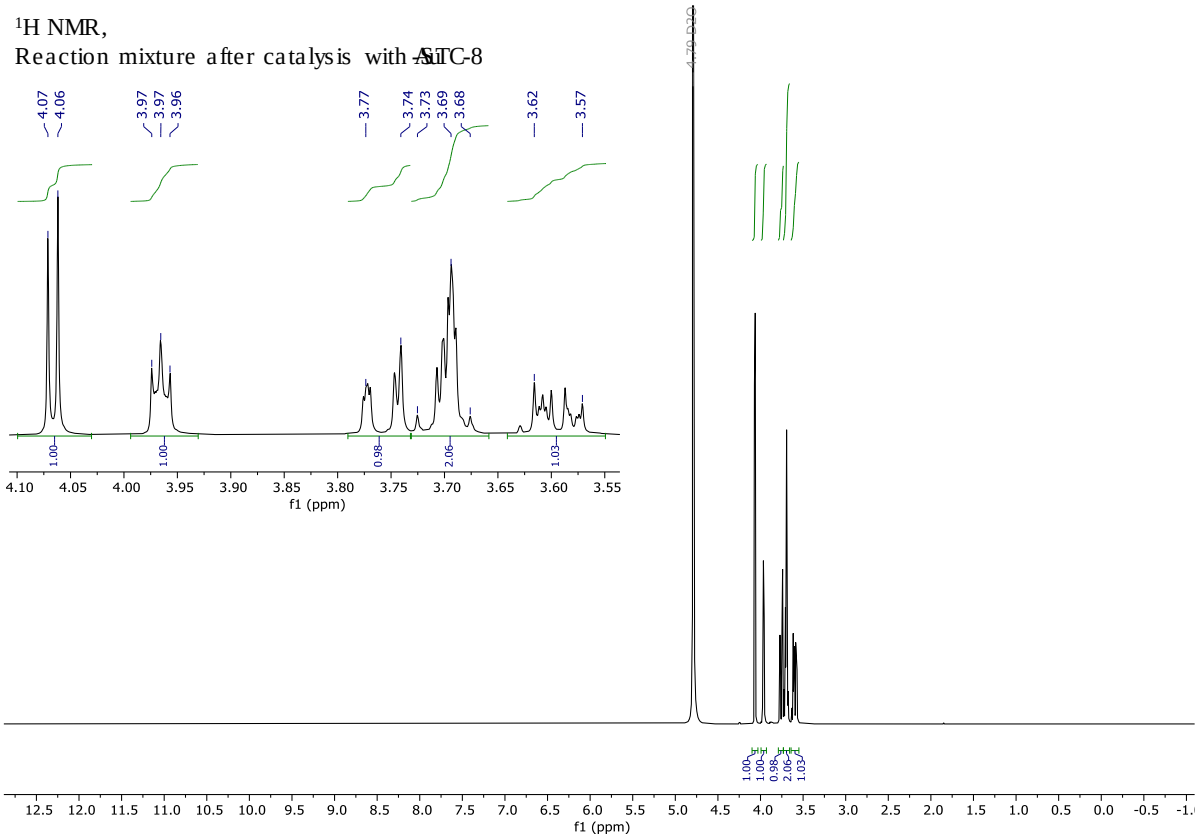

^{13}C NMR,
Reaction mixture after catalysis with AuTC-8

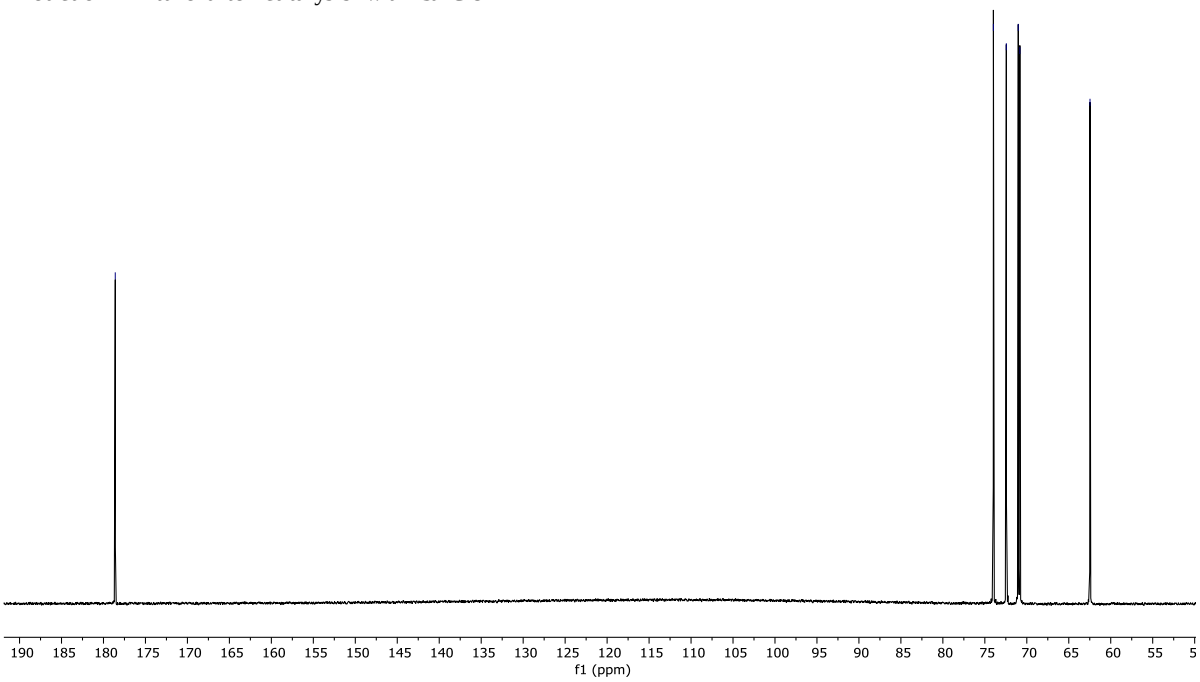

■ : D-glucose
▲ : gluconic acid

^{1}H NMR,
Reaction mixture after catalysis with AuTC-4

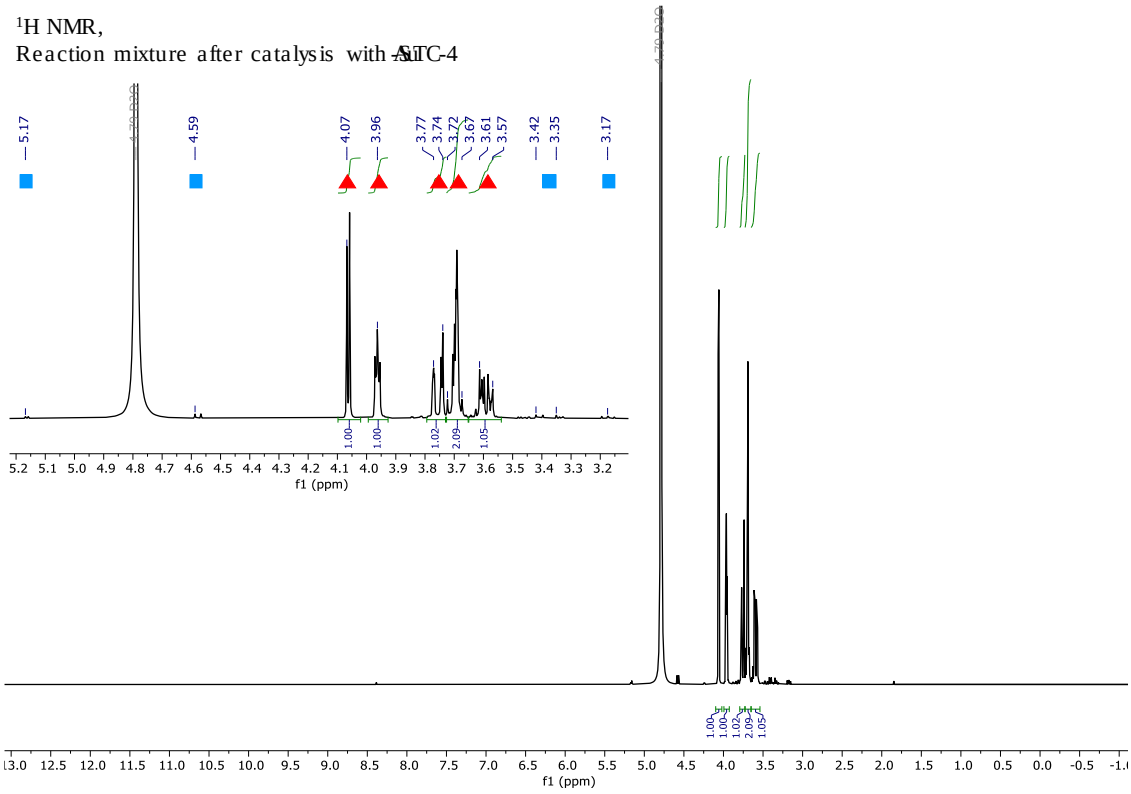

^{13}C NMR,
Reaction mixture after catalysis with AuTC-4

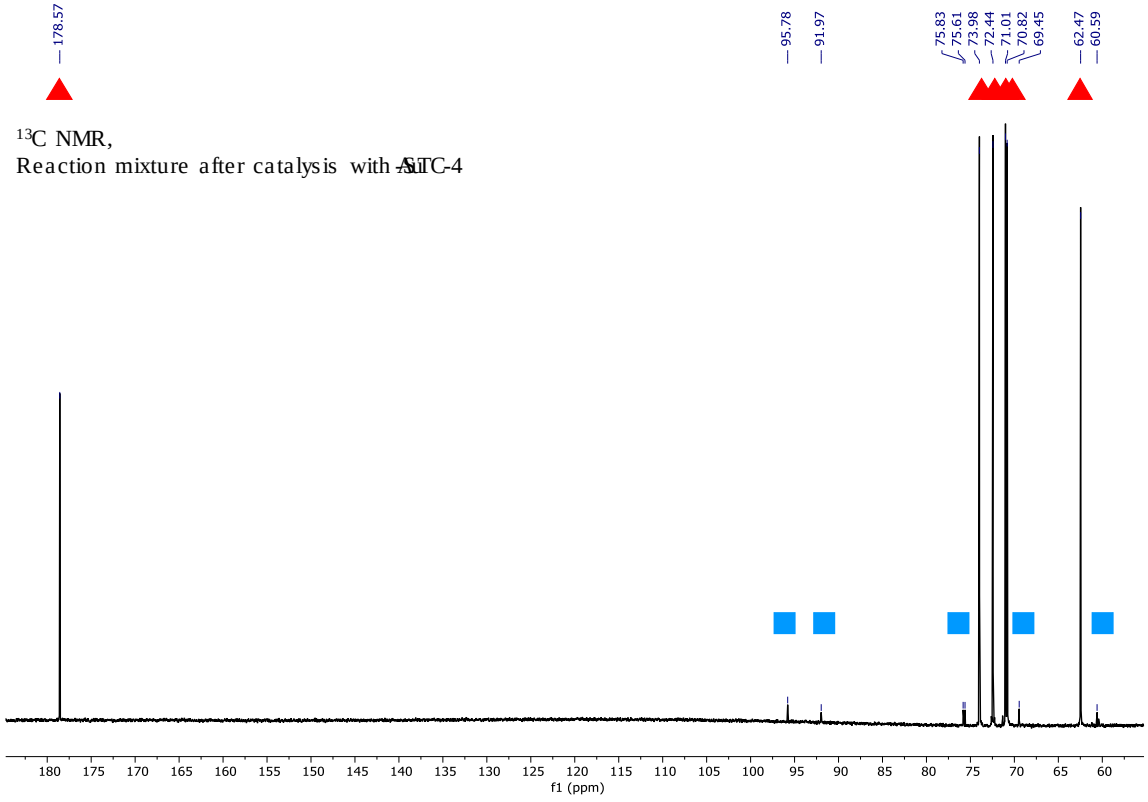

^{1}H NMR,
Reaction mixture after catalysis with AuTC-2

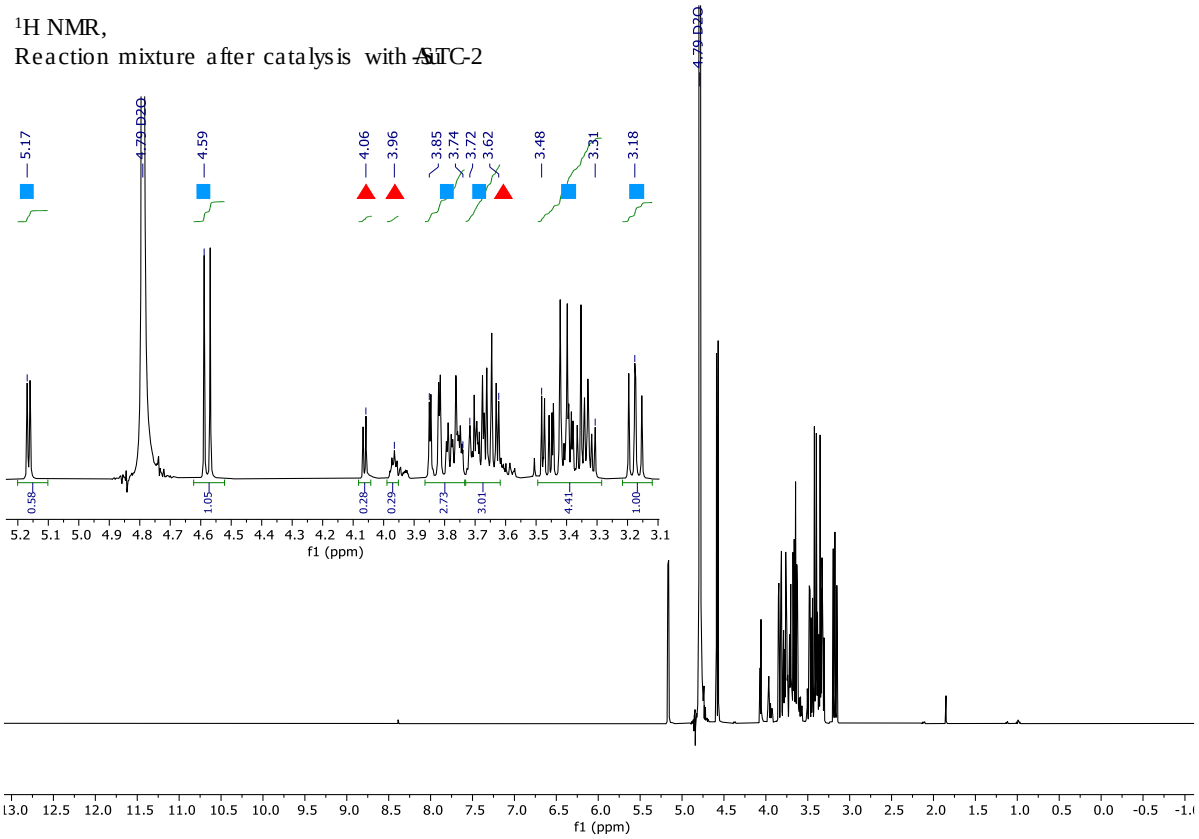

^{13}C NMR,
Reaction mixture after catalysis with AuTC-2

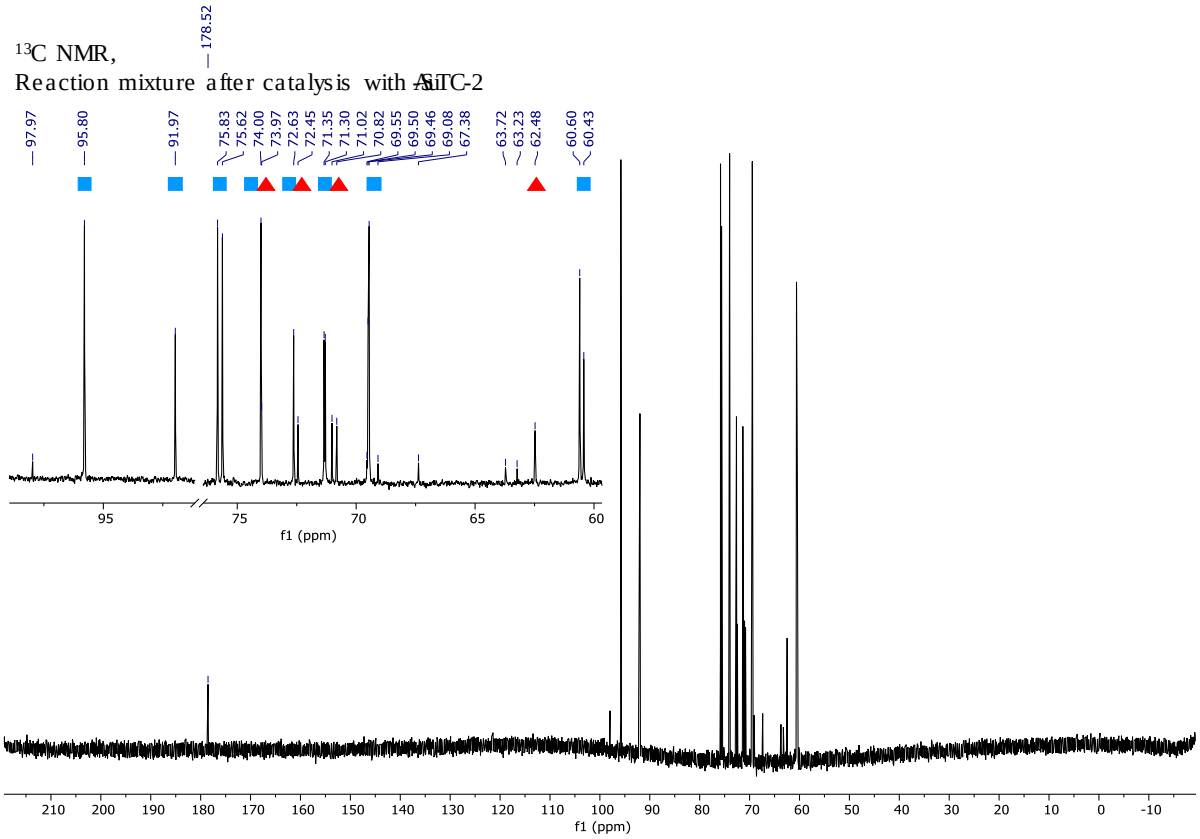

^{1}H NMR,
Reaction mixture after catalysis with Au-STC-1

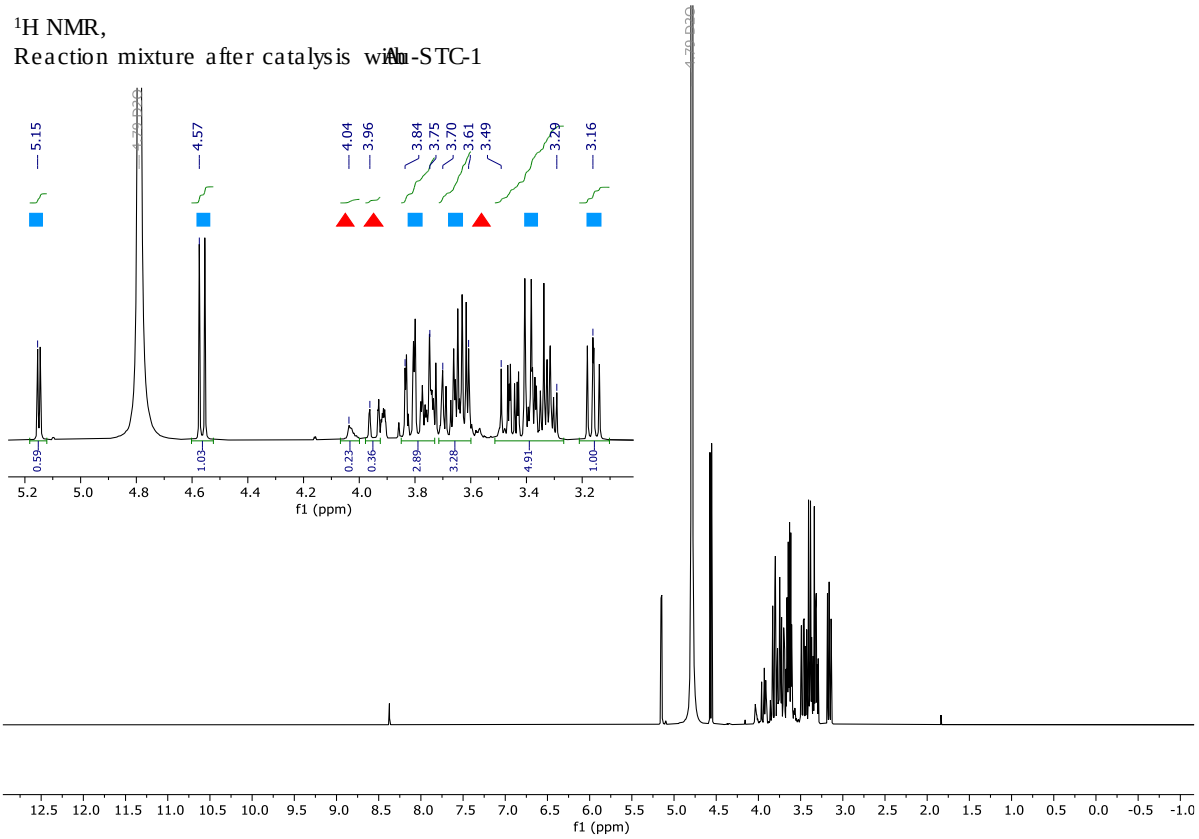

^{13}C NMR,
Reaction mixture after catalysis with Au-STC-1

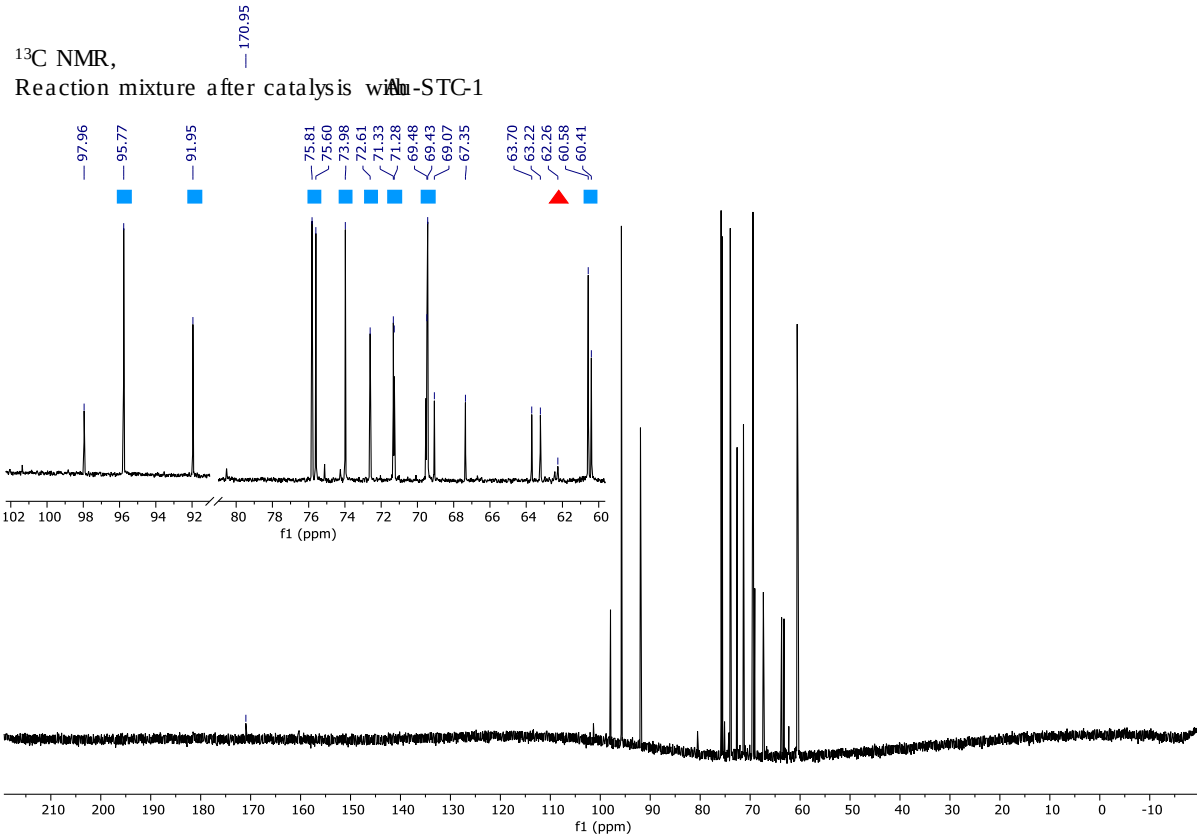

8.4.1. List of Figures

8.4.2. List of Tables

List of Publications

1. Aloni, S. S., **Perovic, M.**, Weitman, M., Cohen, R., Oschatz, M., and Mastai, Y.: Amino acid-based ionic liquids as precursors for the synthesis of chiral nanoporous carbons. *Nanoscale Advances* **2019**, *1*, 12, 4981 – 4988.
2. Ilic, I., **Perovic, M.,** and Liedel, C.: Interplay of porosity, wettability, and redox activity as determining factors for lithium-organic electrochemical energy storage using biomolecules. *ChemSusChem* **2020**, *13*, 7, 1856 – 1863.
3. **Perovic, M.**, Qin, Q., and Oschatz, M.: From Molecular Precursors to Nanoparticles—Tailoring the Adsorption Properties of Porous Carbon Materials by Controlled Chemical Functionalization. *Advanced Functional Materials* **2020**, *30*, 41, 1908371.
4. **Perovic, M.**, Tarakina, N.V., Hofmann, J.P., and Oschatz, M.: Influence of Local Environments in Pores of Different Size on the Catalytic Liquid-Phase Oxidation of d-Glucose by Au Nanoparticles Supported on Nanoporous Carbon. *ACS Applied Nano Materials* **2020**, *3*, 8, 7695 – 7703.
5. **Perovic, M.**, Aloni, S. S., Mastai, Y., and Oschatz, M.: Mesoporous Carbon Materials With Enantioselective Surface Obtained by Nanocasting for Selective Adsorption of Chiral Molecules From Solution and the Gas Phase. *CARBON* **2020**, *170*, 550 – 557.
6. **Perovic, M.**, Zeininger, L., and Oschatz, M.: Immobilization of Gold-on-Carbon Catalysts onto Perfluorocarbon Emulsion Droplets to Promote Oxygen Delivery in Aqueous Phase d-Glucose Oxidation. *ChemCatChem* **2020**, DOI: 10.1002/cctc.202001590.
7. Ilic, I. K., Tsouka, A., **Perovic, M.**, Hwang, J., Heil, T., Loeffler, F.F., Oschatz, M., Antonietti, M., Liedel, C.: Sustainable Cathodes for Lithium-Ion Energy Storage Devices Based on Tannic Acid – Towards Eco-Friendly Energy Storage. *Advanced Sustainable Systems* **2020**, 2000206.
8. **Perovic, M.**, Aloni, S. S., Zhang, W., Mastai, Y., Antonietti, M., and Oschatz, M.: Towards Efficient Synthesis of Porous All-Carbon-based Nanocomposites for Enantiospecific Separation. **2020**, *in preparation*.

Declaration

Die vorliegende Dissertation entstand in dem Zeitraum zwischen April 2018 und August 2020 am Max-Planck-Institut für Kolloid- und Grenzflächenforschung unter Betreuung von Prof. Dr. Dr. h.c. Markus Antonietti.

Hiermit erkläre ich, dass die vorliegende Arbeit selbstständig angefertigt wurde und keine anderen als die angegebenen Hilfsmittel und Quelle verwendet wurden.

Die Arbeit wurde bisher weder im Inland noch im Ausland in gleicher oder ähnlicher Form einer anderen Prüfungsbehörde vorgelegt. Es habe bisher keine früheren erfolglosen Promotionsverfahren stattgefunden.

The present work was carried during the period between April 2018 and August 2020 at the Max Planck Institute of Colloids and Interfaces under the supervision of Prof. Dr. Dr. h.c. Markus Antonietti.

I declare that I have written this work on my own and used no other than the named aids and references.

This thesis was not submitted to another examination board in this or other countries. There were no unsuccessful examination processes.

Milena Perovic

Potsdam, den 27.08.2020